

1N-02-CR
 REF
 0017
 5426
 P- 142

Old Dominion University Research Foundation

DEPARTMENT OF MECHANICAL ENGINEERING
 COLLEGE OF ENGINEERING & TECHNOLOGY
 OLD DOMINION UNIVERSITY
 NORFOLK, VIRGINIA 23529

**EXPERIMENTAL INVESTIGATION OF THE
 INLET DETECTOR CONFIGURATION VARIATION
 IN THE FLOW FIELD AT MACH 1.9**

By

Kyu C. Hwang, Graduate Research Assistant

Surrendra N. Tiwari, Principal Investigator

and

Stanley J. Miley, Research Associate

Final Report

For the period ended May 31, 1995

Prepared for
 National Aeronautics and Space Administration
 Langley Research Center
 Hampton, VA 23681-0001

N96-12563

Unclass

G3/02 0072059

Under

Research Grant NAG-1-1556

Mr. Michael C. Fisher, Technical Monitor
 FAD-Laminar Flow Control Office

(NASA-CR-199617) EXPERIMENTAL
 INVESTIGATION OF THE INLET DETECTOR
 CONFIGURATION VARIATION IN THE FLOW
 FIELD AT MACH 1.9 Final Report
 Report, period ended 31 May 1995
 (Old Dominion Univ.) 142 p

October 1995

DEPARTMENT OF MECHANICAL ENGINEERING
COLLEGE OF ENGINEERING & TECHNOLOGY
OLD DOMINION UNIVERSITY
NORFOLK, VIRGINIA 23529

**EXPERIMENTAL INVESTIGATION OF THE
INLET DETECTOR CONFIGURATION VARIATION
IN THE FLOW FIELD AT MACH 1.9**

By

Kyu C. Hwang, Graduate Research Assistant

Surrendra N. Tiwari, Principal Investigator

and

Stanley J. Miley, Research Associate

Final Report
For the period ended May 31, 1995

Prepared for
National Aeronautics and Space Administration
Langley Research Center
Hampton, VA 23681-0001

Under
Research Grant NAG-1-1556
Mr. Michael C. Fisher, Technical Monitor
FAD-Laminar Flow Control Office

Submitted by the
Old Dominion University Research Foundation
P.O. Box 6369
Norfolk, VA 23508



October 1995

EXPERIMENTAL INVESTIGATION OF THE INLET DEFLECTOR CONFIGURATION VARIATION IN THE FLOW FIELD AT MACH 1.9

Kyu C. Hwang¹, Surendra N. Tiwari², and Stanley J. Miley³

Department of Mechanical Engineering
Old Dominion University, Norfolk, VA 23529

ABSTRACT

In recent years, active research has been conducted to study the technological feasibility of supersonic laminar flow control on the wing of the High Speed Civil Transport (HSCT). For this study, the F-16XL has been chosen due to its highly swept crank wing planform that closely resembles the HSCT configurations. During flights, it is discovered that the shock wave generated from the aircraft inlet introduces disturbances on the wing where the data acquisition is conducted. The flow field about a supersonic inlet is characterized by a complex three-dimensional pattern of shock waves generated by the geometrical configuration of a deflector and a cowl lip. Hence, in this study, experimental method is employed to investigate the effects of the variation of deflector configuration on the flow field, and consequently, the possibility of diverting the incoming shock-disturbances away from the test section. In the present experiments, a model composed of a simple circular tube with a triangular deflector is designed to study the deflector length and the deflector base width variation in the flow field.

Experimental results indicate that the lowest external pressure ratio is observed at the junction where the deflector lip and the inlet cowl lip merge. Also, it is noted that the external pressure ratio, the internal pressure ratio, the coefficient of spillage drag, and the shock standoff

¹ Graduate Research Assistant

² Eminent Professor

³ Research Associate

distance decrease as the deflector length increases. In addition, the Redefined Total Pressure Recovery Ratio (RTPRR) increases with an increase in the deflector length. Results from the study of the effect of the deflector's base width variation on the flow field indicate that the lowest external pressure ratio is observed at the junction between the inlet cowl lip and the deflector lip. As the base width of the deflector increases, the external pressure ratio at 0° rotation increases, whereas the external pressure ratio at 180° rotation decreases. In addition, the internal pressure ratio and the coefficient of spillage drag decrease as the base width of the deflector increases. However, RTPRR and shock standoff distance increase as the base width increases. In conclusion, as deflector dimensions vary, distinctive patterns in the pressure variation around the inlet deflector are observed. With an increase in the deflector length and base width, the magnitude of shock-disturbances are weakened due to a decrease in the external pressure ratio. Also, as the deflector length and base width increase, a smaller bow shock angle is formed. Therefore, the inlet shock wave formation would be significantly altered, and consequently, shock disturbances on the wing test section can be avoided through appropriately designing the deflector.

ACKNOWLEDGMENTS

This is a final report on the research project, "Laminar Instability Measurement System for SLFC Flight Research Program," for the period ended May 31, 1995. Special attention during this period was directed to "Experimental Investigation of the Inlet Deflector Configuration Variation in the Flow Field at Mach 1.9."

The authors are indebted to Dr. Colin P. Britcher for his support and guidance in conducting experiments at Old Dominion University, and to Dr. Gregory V. Selby for his administrative support. Sincere thanks are extended to Mr. J. K. Ahuja for many helpful suggestions and support in CFD analysis, and to Mr. Jerry Robertson and his staff for cooperation in manufacturing parts and rebuilding the tunnel compressor.

This work in part, was supported by the NASA Langley Research Center (Laminar Flow Control Office of the Flight Application Division) through the grant NAG-1-1556. The grant was monitored by Mr. Michael C. Fisher. This, in part, was also supported by the Old Dominion University's ICAM Project through NASA Grant NAG-1-363. This grant was monitored by Mr. Roger A. Hathaway, University Affairs Officer, NASA Langley Research Center, Hampton, Virginia 23681-0001.

TABLE OF CONTENTS

	<u>PAGE</u>
ACKNOWLEDGEMENT	iv
LIST OF TABLES.	viii
LIST OF FIGURES.	x
LIST OF SYMBOLS	xii
 Chapter	
1. INTRODUCTION	1
2. EXPERIMENTAL SETUP	9
2-1. Wind Tunnel	9
2-2. Instrumentation	10
2-3. Experimental Conditions	12
3. PRELIMINARY DESIGN OF TEST MODEL	18
3-1. Maximum Load	19
3-2. Maximum Cross Sectional Area	20
3-3. Material Selection	21
3-4. Structural Analysis	22
4. TEST MODEL	27
4-1. Base Plate	27
4-2. Bracket	28

4-3. Support tube	29
4-4. Flow Regulator	30
4-5. Test Units	31
4-6. Pressure Taps	32
4-7. Final Overview	33
5. EXPERIMENTAL RESULTS	41
5-1. Unsteadiness and Non-Dimensional Data	41
5-2. Flow Conditions and Assumptions	43
5-3. Matching the Incoming Flow Conditions	45
5-4. Calibration of Pressure Transducer	47
5-5. Errors and Accuracy	47
5-6. Uncertainty in Measurements	49
5-7. Verification	50
5-8. Experimental Data	51
6. DISCUSSION OF RESULTS	78
6-1. The Effect of Deflector Length	78
6-2. The Effect of Deflector Base Width	82
7. CONCLUSIONS.	94
REFERENCES	97
APPENDIX A. SHADOWGRAPH PHOTOS	99
A-1. Test Configuration #1-1	100
A-2. Test Configuration #1-2	101

A-3. Test Configuration #1-3	102
A-4. Test Configuration #2-1	103
A-5. Test Configuration #2-2	104
A-6. Test Configuration #2-3	105
APPENDIX B. NUMERICAL ANALYSIS	106
B-1. Governing Equations	107
B-2. Physical Domain and Grid Transformations	110
B-3. Numerical Method	111
B-4. Remarks	114
APPENDIX C. UNCERTAINTY CALCULATIONS	116
C-1. Uncertainty in Direct Measurement	117
C-2. Propagation of Uncertainty.	117
APPENDIX D. COMPUTER PROGRAMS	119
D-1. Basic Program for Data Acquisition	120
D-2. Basic Program for Printing Data	124
D-3. Fortran Program for Correcting Data	126

LIST OF TABLES

<u>TABLE</u>	<u>PAGE</u>
5-1. Experimental results for test configuration #1-1	60
5-2. Experimental results for test configuration #1-2	61
5-3. Experimental results for test configuration #1-3	62
5-4. Experimental results for test configuration #2-1	63
5-5. Experimental results for test configuration #2-2	64
5-6. Experimental results for test configuration #2-3	65
5-7. Non-dimensional results for test configuration #1-1	66
5-8. Non-dimensional results for test configuration #1-2	66
5-9. Non-dimensional results for test configuration #1-3	67
5-10. Non-dimensional results for test configuration #2-1	67
5-11. Non-dimensional results for test configuration #2-2	68
5-12. Non-dimensional results for test configuration #2-3	68
5-13. Corrected non-dimensional results for test configuration #1-1 .	69
5-14. Corrected non-dimensional results for test configuration #1-2 .	69
5-15. Corrected non-dimensional results for test configuration #1-3 .	70
5-16. Corrected non-dimensional results for test configuration #2-1 .	70
5-17. Corrected non-dimensional results for test configuration #2-2 .	71
5-18. Corrected non-dimensional results for test configuration #2-3 .	71

5-19. Corrected average non-dimensional results for test configuration #1-1	72
5-20. Corrected average non-dimensional results for test configuration #1-2	72
5-21. Corrected average non-dimensional results for test configuration #1-3	73
5-22. Corrected average non-dimensional results for test configuration #2-1	73
5-23. Corrected average non-dimensional results for test configuration #2-2	74
5-24. Corrected average non-dimensional results for test configuration #2-3	74
5-25. Redefined Total Pressure Recovery Ratio and coefficient of spillage drag for test configuration #1-1	75
5-26. Redefined Total Pressure Recovery Ratio and coefficient of spillage drag for test configuration #1-2	75
5-27. Redefined Total Pressure Recovery Ratio and coefficient of spillage drag for test configuration #1-3	76
5-28. Redefined Total Pressure Recovery Ratio and coefficient of spillage drag for test configuration #2-1	76
5-29. Redefined Total Pressure Recovery Ratio and coefficient of spillage drag for test configuration #2-2	77
5-30. Redefined Total Pressure Recovery Ratio and coefficient of spillage drag for test configuration #2-3	77

LIST OF FIGURES

<u>FIGURE</u>	<u>PAGE</u>
1-1. Schematic of the F-16XL test section and shock disturbances	8
2-1. Schematic of the supersonic tunnel test section	14
2-2. Schematic of the blowdown type supersonic tunnel.	15
2-3. Schematic of the shadowgraph operation.	16
2-4. F-16 inlet	17
3-1. Theoretical design flow condition for structural analysis.	24
3-2. Theoretical maximum cross sectional area	25
3-3. Theoretical model for the structural analysis	26
4-1. Schematic of the support mechanism	34
4-2. Schematic of the support mechanism base plate.	35
4-3. Schematic of the bracket and the support tube.	36
4-4. Schematic of the flow regulator	37
4-5. Schematic of the test unit	38
4-6. Photographic view of the support mechanism and the test units	39
4-7. Photographic view of the support mechanism in tunnel	40
5-1. Typical stagnation pressure measurements during the tunnel operation	53

5-2. Typical non-dimensional external pressure measurements during the tunnel operation	54
5-3. Typical non-dimensional internal pressure measurements during the tunnel operation	55
5-4. Shadowgraph photo of two external probes in supersonic flow .	56
5-5. Stagnation pressure measurements with PSI-DPT and MKS-PDT	57
5-6. A) Shadowgraph photo for a flat circular cylinder at $M=1.9$.	58
5-6. B) Schlieren photo for a flat circular cylinder at $M=2.0$. . .	58
5-7. Theoretical and experimental comparison of the internal pressure ratio for a pitot type inlet.	59
6-1. External probe pressure ratio measurements for different deflector lengths	86
6-2. Internal probe pressure ratio measurements for different deflector lengths	87
6-3. Redefined Total Pressure Recovery Ratio (RTPRR) for different deflector lengths and a theoretical simple pitot tube.	88
6-4. Coefficient of spillage drag vs. total pressure recovery ratio for different deflector lengths	89
6-5. External probe pressure ratio measurements for different base widths	90
6-6. Internal probe pressure ratio measurements for different base widths	91
6-7. Redefined Total Pressure Recovery Ratio (RTPRR) for different base width lengths and a theoretical simple pitot tube	92
6-8. Coefficient of spillage drag vs. total pressure recovery ratio for different base widths	93

LIST OF SYMBOLS

A	Area
C_d	Drag Coefficient
E	For Fluid Analysis: Total Energy For Structural Analysis: Young's Modulus
F	Force
G	Shear Modulus
I	Moment of Inertia
I_p	Polar Moment of Inertia
J	Jacobian
k	Thermal Conductivity
L	Material Length
M	For Fluid Analysis: Mach Number For Structural Analysis: Momentum
P	Pressure
P_o	Stagnation Pressure
P^*	Non-Dimensional Pressure

q	Heat Flux
r	Radius of Gyration
R	Universal Gas Constant
Re	Reynolds Number
T	Temperature
T_o	Stagnation Temperature
u	X-Component Velocity
v	Y-Component Velocity

Greek Symbols

δ	Deflection
δ_{comp}	Compressional deflection
μ	Viscosity
ρ	Density
σ	Normal Stress
$\sigma_{buckling}$	Critical Stress for Buckling
τ	Shear Stress
ϕ	Torsional Deflection (Radian)

Chapter 1

INTRODUCTION

For many years, the National Aeronautics and Space Administration (NASA) has been involved in the design and development of a commercial supersonic aircraft known as the High Speed Civil Transport (HSCT). In recent years, active research has been conducted to study the technological feasibility of Supersonic Laminar Flow Control (SLFC) on the HSCT's wing. Successful application of laminar flow control to HSCT is desired, because it offers significant benefits in reductions of take-off structural load, fuel consumption, and noise [1].*

To experimentally study the feasibility of SLFC, the F-16XL has been chosen due to its highly swept cranked delta wing planform that closely resembles the HSCT configurations. The F-16XL has an inboard section of the wing which is swept 70° , and the outboard section which is swept 50° . Currently, NASA has two F-16XL's in service in which the single seat aircraft is assigned to NASA Langley Research Center, VA, for the feasibility study, and the two seat aircraft is assigned to NASA Dryden Flight Research Center,

* The numbers in brackets indicate references.

CA, for laminar flow research. For the feasibility study, hot-film sensor arrays are deployed along the F-16's wing to investigate the flow development.

It was discovered during flights at Langley Research Center that large disturbances were detected on the wing. These disturbances appeared due to the presence of a shock wave generated from the engine inlet [2]. The F-16XL has an axisymmetric pitot inlet with a "deflector plate" attached at a upper lip of the cowl. This inlet configuration is designed to generate a series of the shock waves to increase the inlet pressure recovery. During flights, the shock wave swept across the wing section where the data acquisition was conducted (Fig. 1-1). Since shock-disturbances introduce the instability in the flow field measurements, to improve the feasibility study, two methods were suggested to eliminate the disturbances along the wing. The first method was to install a vertical plate underneath the wing to deflect the shock wave away from the wing. The other was to appropriately modify the inlet, especially the configuration of the inlet deflector, to divert the shock wave away from the wing.

Of the two methods suggested, active consideration was given to installing a vertical plate underneath the wing for the following factors. First, the data required to design the plate was readily available. Second, the plate configuration was simpler for analysis. Finally, if the optimal design of the plate is obtained, the incoming shock wave would be deflected away from the wing, and the acquisition of undisturbed data would be possible. To obtain the

optimal design, numerical analysis was employed due to its inexpensiveness. However, during the wind tunnel test, Laser Doppler Velocimeter (LDV) measurements indicated that the plate could not completely deflect the shock wave away from the wing section. The results revealed that much of the shock wave bypassed the plate and consequently disturbed the wing. Although the magnitude of disturbances along the wing had been significantly weakened, disturbances to the data were still considerable. Complete elimination of disturbances by the plate was not achieved, because numerical analysis could not accurately predict the dynamic variation in flight conditions.

Alternatively, to eliminate disturbances, the modification of the inlet deflector configuration was considered. The method was attractive due to the following factors. First, the method provided a permanent solution to the problem. The source of the shock wave would be modified and redirected away from the wing. Last, with the method, any introduction of an unwanted object to the aircraft body would not be needed. Although this would provide solutions to many problems, immediate implementation of the method was not considered, because insufficient information, especially the effects of the pressure distribution around an inlet at various deflector configurations, was available. Since the modification of the inlet-deflector would require extensive knowledge of the fluid motion around the inlet at different deflector configurations, a need to investigate the flow field around the inlet for different deflector configurations inevitably rose.

For the investigation, a literature survey was conducted to retrieve related research previously done by other investigators. The lecture notes written by Seddon, Goldsmith, et al. [3] provided the basic functions and objectives of an inlet design. In the notes, Seddon, et al. stated that the flow field about a supersonic inlet is characterized by a complex three-dimensional pattern of oblique shock waves generated by the geometry of the deflector and the cowl lip. Also, the notes described that the inlet efficiency and the spillage drag are determined by the formation of shock waves. The notes illustrated a detailed description of the flow field for various inlet configurations, but the external pressure variation around an axisymmetric inlet at various deflector configurations was not discussed.

The experimental study conducted by Ferri and Nucci [4] reported the overall performance of a circular inlet with a single step conical central body at Mach 2.45, 2.75, and 3.30 with the corresponding Reynolds numbers ranging from 3.0×10^6 to 3.5×10^6 . The study presented the effects of the mass flow rate and the angle of the central body on the pressure variations around the inlet. The shadowgraph photos showed that the angle of the spillage shock increased as the internal mass flow rate decreased. The shock is a discontinuity in the flow field, and the spillage shock is a curved shock that is induced by the air spillage at the aircraft inlet. In addition, as the angle of the central body increased, the angle of the spillage shock decreased. In this study, a successful investigation of the external shock wave formations for different

internal mass flow rates and conical body configurations was conducted. However, the investigation of a circular inlet with a deflector on a upper lip of the cowl at Mach 1.9 was not included.

The numerical study conducted by Flores, Chaderjian, and Sorenson [5] reported the pressure distribution around the F-16A inlet at Mach 0.9, attack angle of 4.12° , and the Reynolds number of 4.5×10^6 . The results were based on the zonal approach of the thin-layer Navier Stokes equations. In zonal approach, the flow field is partitioned into distinct zones where each zone is solved independently. In the study, the pressure distribution around the inlet was investigated as an integrated part of the fuselage. Hence, a full description of the pressure variations around the inlet at supersonic flow conditions was not achieved.

The study conducted by Huband, Rizzetta, and Shang [6] reported the pressure distribution around the F-16A inlet at Mach 1.2, attack angle of 6° , and the Reynolds number 12.75×10^6 . The results were based on the three dimensional Navier Stokes equations with the MacCormack explicit algorithm. Although the results provided the pressure distribution around the inlet as an integrated part of the fuselage at supersonic flow conditions, the study omitted the deflector from the inlet configuration for simplicity in numerical analysis, therefore, the full description of the pressure variations around the inlet was not included.

Based on the literature survey, although many of the studies were conducted for axisymmetric inlets, the full description of the external pressure distributions around the inlet deflector at different deflector's lengths and widths was not included. Hence, the research objective of this study is to experimentally investigate the external pressure and Mach number variation around a pitot inlet with various deflector configurations. In addition, the shock angle, the shock standoff distance, the spillage drag, and the total pressure recovery ratio are investigated. The other objective is to study the possibility of diverting shock-disturbances away from the wing. At this point it would be important to state that the objective of this study is not to determine an optimal inlet design, but rather, provide overall information for the optimal design.

The general layout of this thesis is as follows. In Chap. 2, the detailed descriptions of instruments along with their limits in measurements are described. In Chap. 3, the preliminary design goals and criteria for the support mechanism and the test units are elaborated. In Chap. 4, the full description of the support mechanism and the test units are included. In Chap. 5, the nondimensionalization of the results are discussed. Also, a detailed description of the assumptions that applied for data analysis are included. Consequently, along with its accuracy and limits, the tabulated form of the results are presented. In Chap. 6, the effects of each geometrical

variation in the flow field are discussed. Finally, conclusions drawn from this study are presented in Chap. 7.

Initially, to validate the results, numerical analysis was introduced. However, after extensive trial and error, it was concluded that the axisymmetric SPARK code could not successfully model the inlet configurations. An extensive modification of the code was needed which task was beyond of scope the this investigation. However, the theoretical formulation for CFD was done, and this is included in Appendix B. for future investigation.

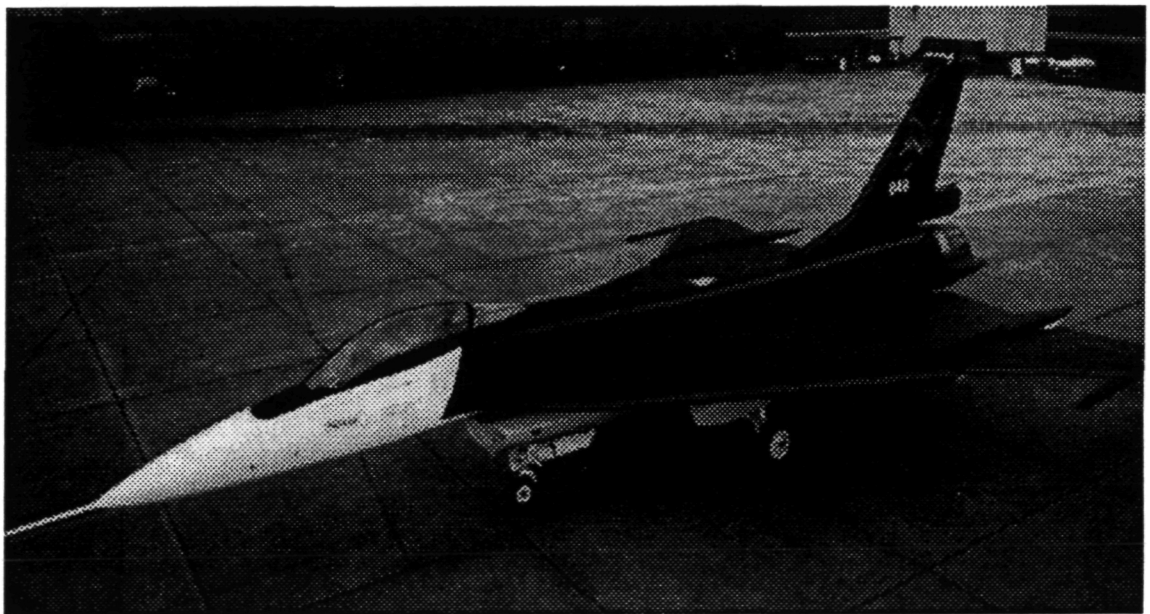
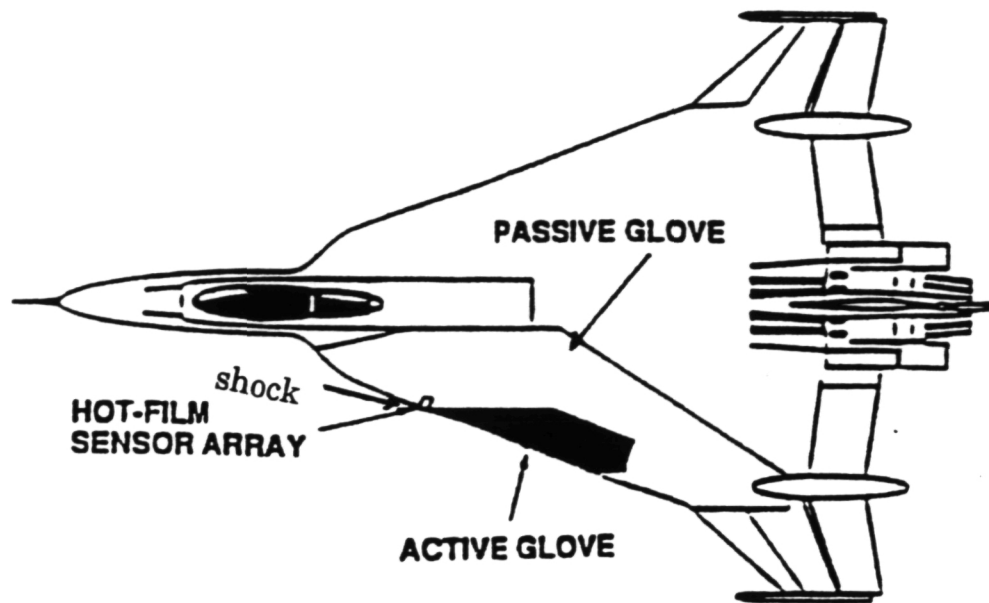


Figure 1-1. Schematic of the F-16XL test section and shock disturbances.

Chapter 2

EXPERIMENTAL SETUP

In the experiments, data acquisition depends on the instruments for the measurements. Since the accuracy in the measurements depends on the instruments, a detailed description of the experimental instruments would be necessary in understanding their functions and limits. Accordingly, in this chapter, the instruments and the experimental conditions are described.

2-1. Wind Tunnel

The supersonic wind tunnel facility at Old Dominion University is an Aerolab 4 inch by 4 inch sliding block type blowdown tunnel that was designed to operate in the speed range of Mach 1.5 to Mach 3.5. The sliding block type setting provides a smooth variation of Mach number. The Mach number in the test section is set carefully by controlling the throat area through manually moving a lower part of the nozzle block (Fig. 2-1).

The general description of the tunnel operation is that the compressed air from two 1942 cubic feet tanks flows into the tunnel's "settling chamber" through a pneumatically operated valve (Spencer valve). The flow leaves the

settling chamber through perforated steel screens which remove large scale disturbances from the flow. Then, the flow enters a convergent-divergent nozzle and into the test section (Fig. 2-2). To obtain the specific Reynolds number operation, stagnation pressure is preset through the control panel. With the preset stagnation pressure, the Spencer valve begins to regulate the settling chamber pressure and thus stabilizes the stagnation pressure through a solenoid switch. The maximum operating time of the tunnel is 30 seconds, and each tank can hold air at a maximum pressure of 100 Psig.

2-2. Instrumentation

The facility has a PSI DPT-6400 pressure transmitter for the pressure measurements. DPT-6400 was designed to support eight transducers, and each transducer could support eight different pressure ports. Currently, the facility has two transducers active and supports a maximum of 16 pressure ports for the experiments. During the tunnel operation, each pressure port is opened for the input pressure readings, then transmits these data back to a transducer as a voltage. Transmitting the data to the transducer would not be initiated until all the pressure ports read the input pressures. Once the data are transmitted as a voltage, the transmitter converts the incoming signals to the actual pressure as follows.

$$P = A + B*V$$

where

P = Gage Pressure
A = Zero Coefficient
B = Span Coefficient
V = Voltage Input

Both Zero and Span coefficients for each port were calibrated previously and are stored in the transmitter's memory. The calculated pressure is then sent to an output port for display. Since DPT-6400 does not support the data storage, an AT&T personal computer is supplemented. To link the transmitter to the computer, the interface program which was written in BASIC is introduced. Through the program, the pressure outputs at each sampling are transmitted from DPT-6400 to the computer for the display and storage. However, due to limited capability of the transmitter, the sampling rate is set for 2 seconds.

The facility has a platinum resistance thermometer which is mounted in the settling chamber of the tunnel for measuring the stagnation temperature. The thermometer is a voltage sensitive device, and is connected to the multifunction board for the temperature readings. The multifunction expansion board (DASCON-1) which was manufactured by the MetraByte Corporation, has a four channel, 12 bit analog-digital converter, and a maximum 30 conversions per second capability. In the experiments, due to the small test section area, technical difficulty in measurements, and financial constraint, direct temperature measurements in the test section are not conducted.

The facility also has a Shadowgraph system for the non-intrusive measurements. The general description of the system is that a light generated from the 100 W Mercury Vapor Arc lamp is reflected by a 6 inch diameter concave mirror through the test section and then on to a screen (Fig. 2-3). The shadowgraph system depends on variation of the index of refraction in a transparent medium (air) and the resulting effects on a light beam passing through the test region. In a shadowgraph system, the linear displacement of the perturbed light is measured, and the variation of the second derivative of the index of refraction (second derivative of density) with respect height appears on a screen behind of the test section.

2-3. Experimental Conditions

The experiments are conducted at the supersonic facility at Old Dominion University. For the investigations, instead of duplicating the complicated F-16 inlet, a simple circular tube with a triangular deflector attached at a upper lip of the cowl is chosen for simplicity and ease in duplication. Although there is a difference in geometrical configurations between the F-16 inlet (Fig. 2-4) and the test model, in general, both inlet configurations display similar flow characteristics, therefore, the simple circular tube is adequate for this study. In the study, two basic patterns of the deflector configurations are investigated. The first set of experiments is conducted with the inlet at different deflector lengths. The second set of

experiments is conducted with the inlet at different base lengths. In each test, to accurately investigate the effects of these two variables, the other geometrical properties - diffuser length, diffuser area distribution, and cowl lip profile - are maintained constant. The test is conducted at Mach 1.9 with the internal Reynolds numbers between 1.12×10^3 and 1.35×10^3 . The simulated inlet has a subcritical mode of operation and the internal mass flow rate of 83 percent of the incoming mass flow rate of air. The internal mass flow rate is calculated based on the inlet without a deflector at Mach 1.9. In the experiment, the data are obtained through the pressure probes and the method of shadowgraph.

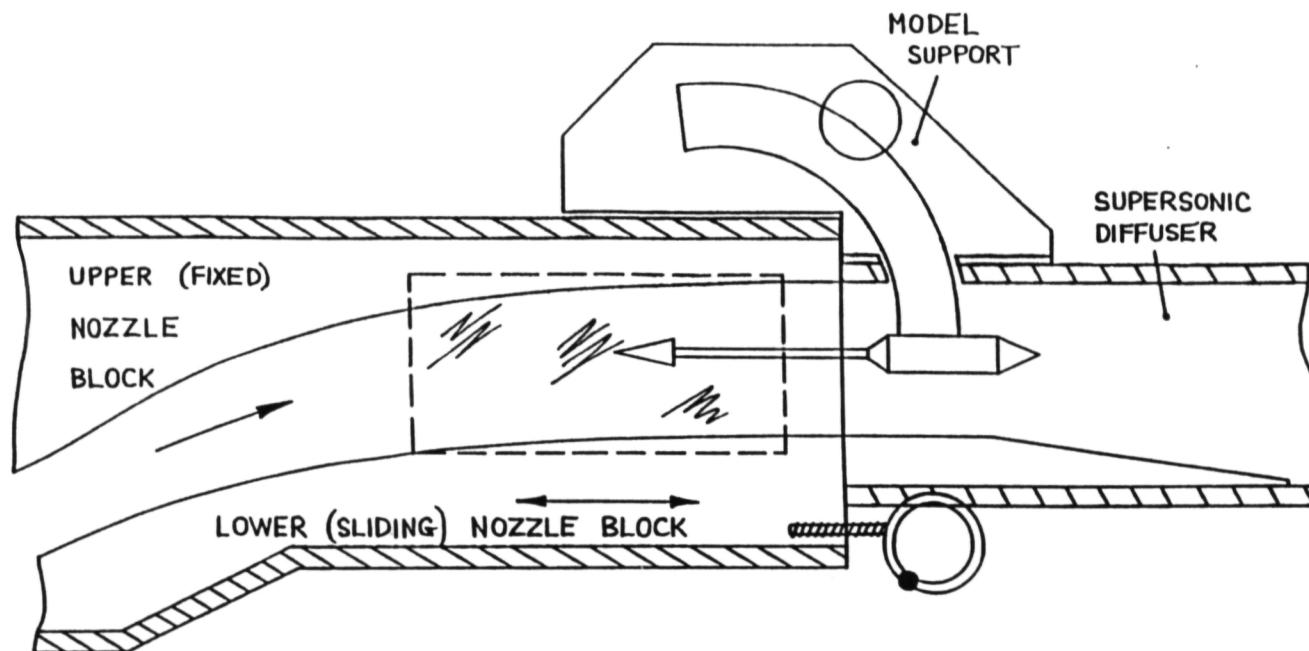


Figure 2-1. Schematic of the supersonic tunnel test section.

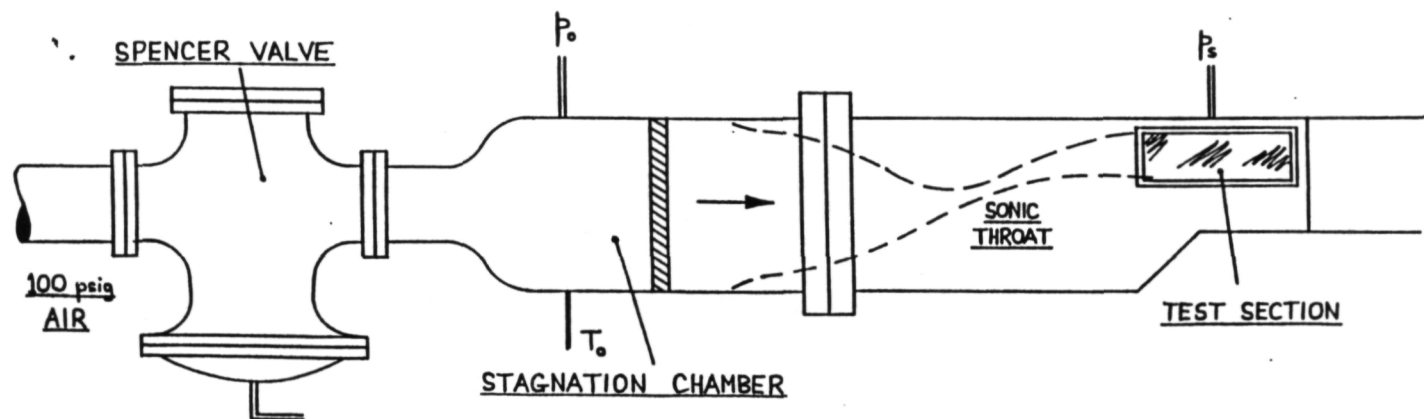


Figure 2-2. Schematic of blowdown type supersonic tunnel.

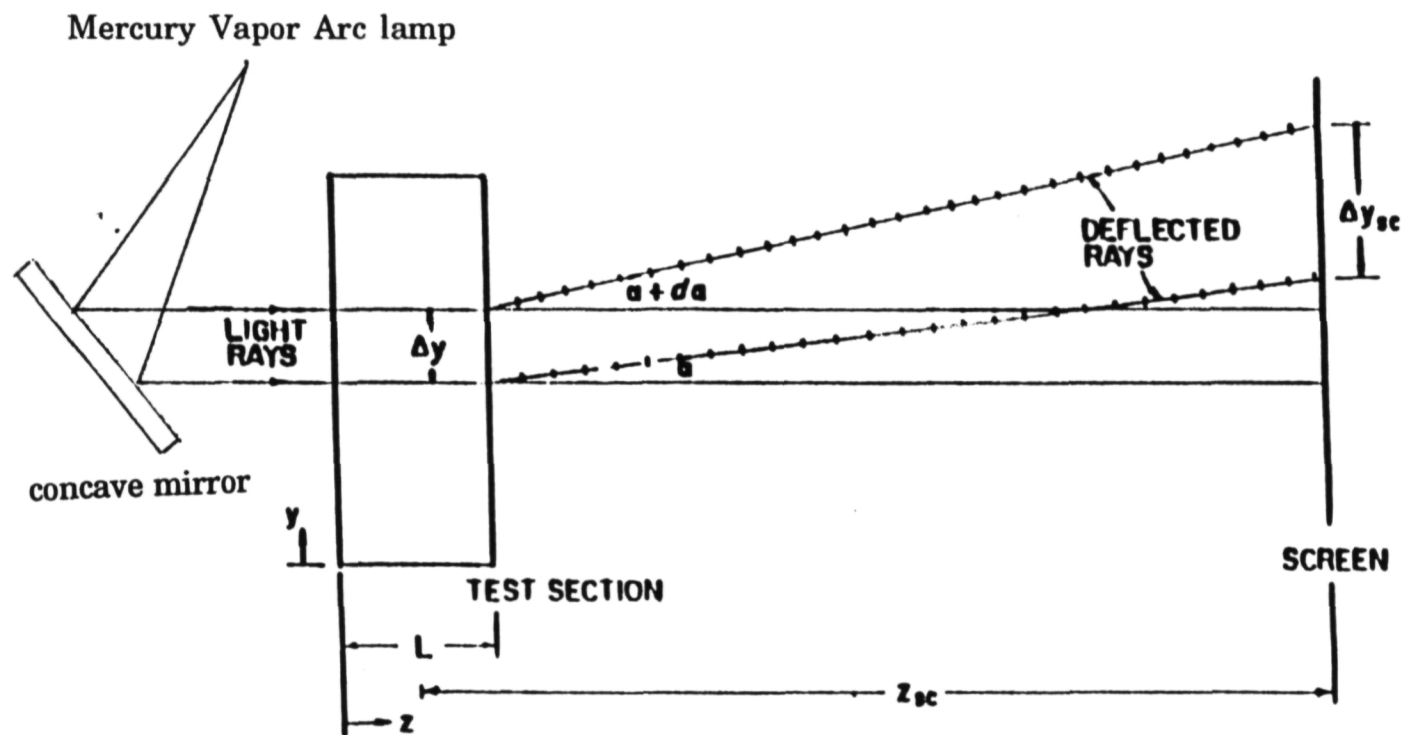


Figure 2-3. Schematic of the shadowgraph operation.

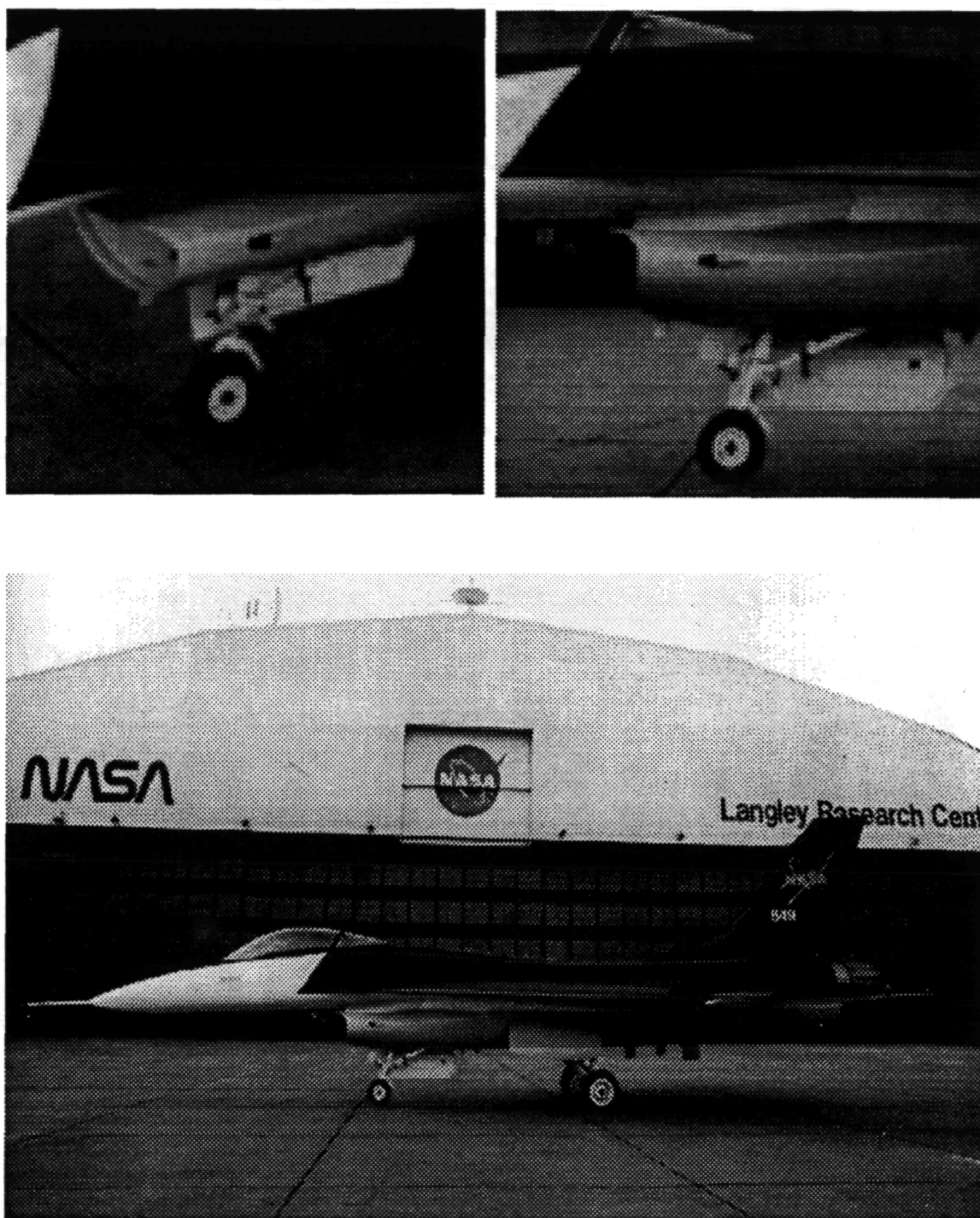


Figure 2-4. F-16 inlet.

Chapter 3

PRELIMINARY DESIGN OF TEST MODEL

In a wind tunnel, it is desired to subject a test object to the flow conditions that it undergoes in actual flight. To create a test object of an appreciable size to test and maintain uniform supersonic flow for a sufficient time to extract meaningful results requires effort. Generally, for a blowdown tunnel, designing an appreciable size of a test object and maintaining an adequate supersonic flow require many compromises. Hence, it is essential to understand their relationships in the flow field.

Unlike in subsonic flow where the pressure distribution is rather continuous, in supersonic flow, the pressure distribution along a test object is discontinuous due to the presence of shock waves. Therefore, a model suffers various type of stresses and forces during the tunnel operation. These stresses and forces induce various structural problems (vibration, deflection, torsion, and deformation etc.) on a model, and consequently, could result in catastrophic structural failures detrimental to the tunnel environment. In a supersonic experiment, blockage of the tunnel or the presence of loose objects in the tunnel during operation could be fatal to the tunnel operation as well

as to the operator(s). Accordingly, it is important to understand the condition of the tunnel operation to design a model within the safety limits to avoid any fatal consequences.

In this study, to insure a safe and adequate test model, four preliminary design stages are considered. First, the maximum hypothetical pressure load on the test object is considered. Then, with the load and the test Mach number, the maximum cross sectional area of the test object is examined. Third, the selection of material is considered. Finally, the structural analysis is conducted. In the next sections, each design stage is discussed with appropriate mathematical models and theory.

3-1. Maximum Load

To insure the safe modelling, the maximum hypothetical pressure difference on a model during the operation is considered. The mathematical equation for this calculation is as follow.

$$\frac{P_o}{P} = \left[1 + \frac{\gamma-1}{2} M^2 \right]^{\frac{\gamma}{\gamma-1}} \quad (3-1)$$

For the analysis, the following assumptions are made. First, as shown in Fig. 3-1, it is assumed that the tunnel is operated at Mach 1.9 and the maximum stagnation pressure of 60 Psig. Second, the conditions of isentropic and inviscid flow before and after the shock are assumed. Finally, it is

assumed that the one side of the model is exposed to the supersonic flow while the other is exposed to the subsonic flow. One side of the model captures the normal shock wave due to small local outlet area. With the above assumptions, 26.5 Psig of the test model pressure difference is calculated.

3-2. Maximum Cross Sectional Area

In the second design stage, the maximum cross sectional area of the model is calculated. From a practical point of view, a larger model is preferred since the model captures more detail of the flow field variation and provides a structurally safer model.

However, for the blowdown tunnel, the maximum cross sectional area of the test object is restricted and dependent on the test Mach number because of the limited amounts of the supply pressure [9]. At the initial stage of the tunnel operation, the normal shock is generated from the primary throat area and exits through the test section. Accordingly, if a larger test object is introduced to the test section, the test object blocks the passage of the normal shock from the test section; therefore, the normal shock would be captured and would remain in the upstream of the test object throughout the experiments. If the above situation arose, the condition of supersonic flow in the test section would not be met. For the closed loop type tunnel, if the above situation arose, increasing the supply pressure would eliminate the normal shock in the test section and thus secure supersonic flow in the test section.

Figure 3-2 shows the maximum ratio of the cross sectional area (the maximum cross sectional area of the test object to the total cross sectional area of the test section) as a function of the test Mach number. The figure illustrated that when the Mach number is increased, the upper limit of the maximum percentage ratio is increased. This indicated that a larger cross sectional area of the test object is permitted as the Mach number increases. At Mach 1.9, the recommended maximum theoretical cross sectional area of the test object is 15 percent of the cross sectional area of the test section. However, since there would be pressure loss due to friction in the test section in actual flow, the maximum cross sectional area of the test object was selected to 10 percent or 1.6 square inches of the cross sectional area of the test section.

3-3. Material Selection

With the maximum theoretical pressure load of 26.5 Psig and the cross sectional area of the test object of 1.6 square inches, steel is selected for the experiments due to following reasons. First, steel provides high strength to the test object to withstand the load. Last, the cost of steel is within the limit of the budget and the material is already available for use.

3-4. Structural Analysis

With known maximum pressure load, maximum cross sectional area of the test object, and the material type, the final step in the preliminary design is to select the length of the test object. To determine the length, two criteria are considered. First, the deflection of the test object is within the limit of tolerance. In the experiments, the limit is set for 0.1 percent variation in length of each component. Last, it is considered that the length of the test object should be long enough to mount on the outer tunnel wall and to locate in the test section. For the analysis, the following mathematical equations are used.

$$\phi = \frac{ML}{GI_P} \quad (3-2)$$

$$\delta_{\text{comp}} = \frac{FL}{EA} \quad (3-3)$$

$$\sigma_{\text{buckling}} = \frac{\pi^2 E}{\left(\frac{L}{r}\right)^2} \quad (3-4)$$

$$\delta_{\text{max}} = \frac{ML^2}{2EI} + \frac{FL^3}{3EI} + \frac{F_{\text{pressure load}} L^4}{8EI} \quad (3-5)$$

As indicated in Fig. 3-3, the theoretical test section is simulated for the calculations. A simple two dimensional beam and a circular cylinder are utilized separately to simulate the model configurations. These configurations are selected, because the shapes provide simpler structural analysis and are easy to manufacture. These configurations are utilized to form the basis for the test model. Although the flow conditions in Fig. 3-3 do not simulate the precise tunnel environment, these provide the simple and effective analysis in predicting possible outcomes. In the analysis, the structural effects due to the lateral loads are less significant than the effects due to the longitudinal loads, hence, the effects due to the lateral loads along the model are neglected.

Finally, it is noted that, in each design stage, Factor Of Safety (FOS) is applied to carry out the next calculation. FOS compensates for the difference between the theoretical and the actual values. In the analysis, FOS of 2 is used to ensure a safe model.

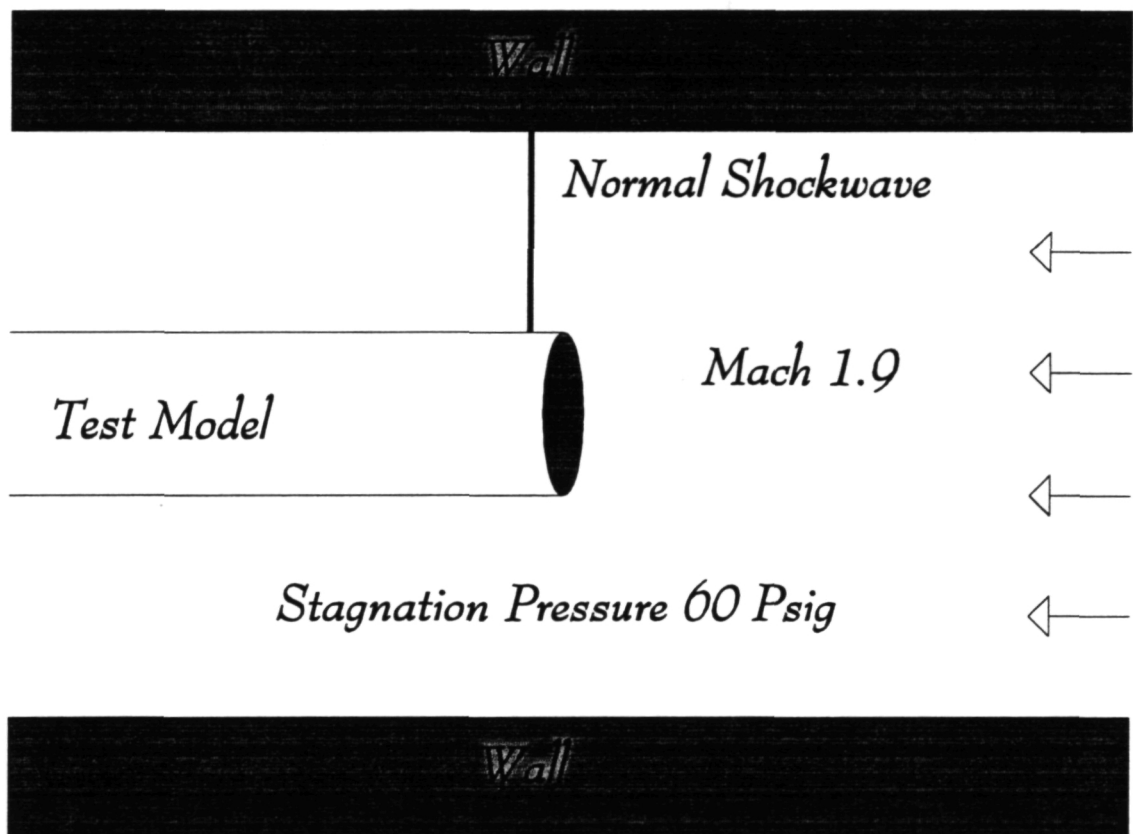


Figure 3-1. Theoretical design flow condition for structural analysis.

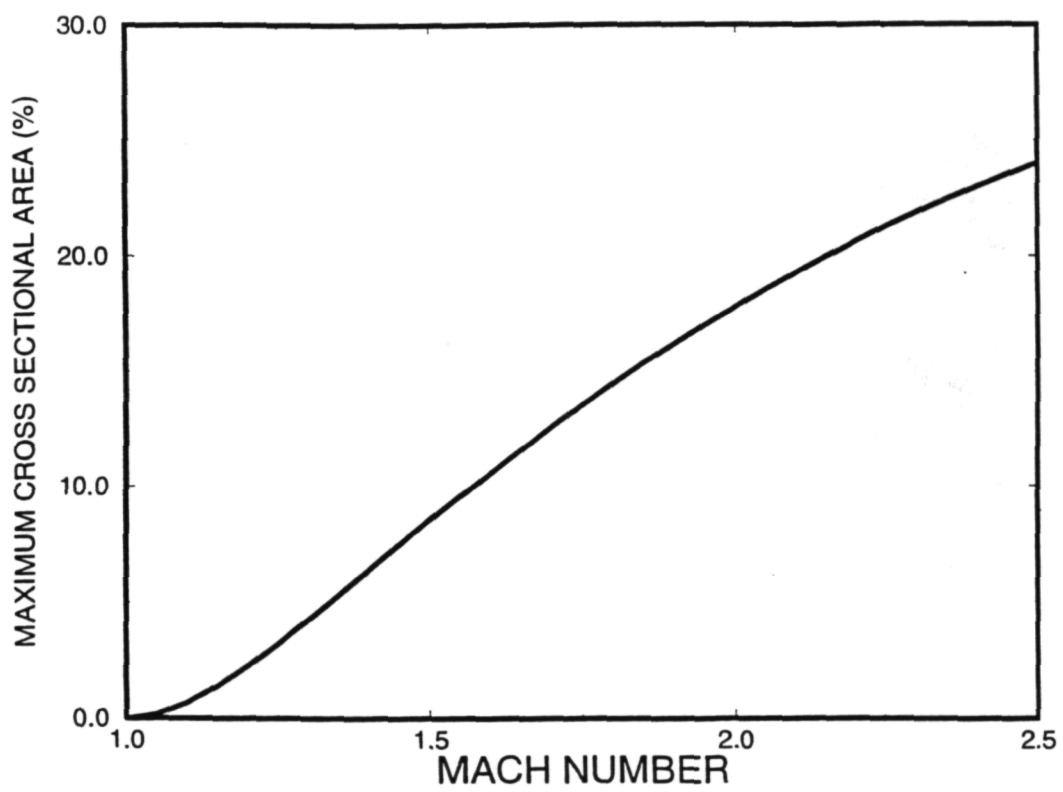


Figure 3-2. Theoretical maximum cross sectional area.

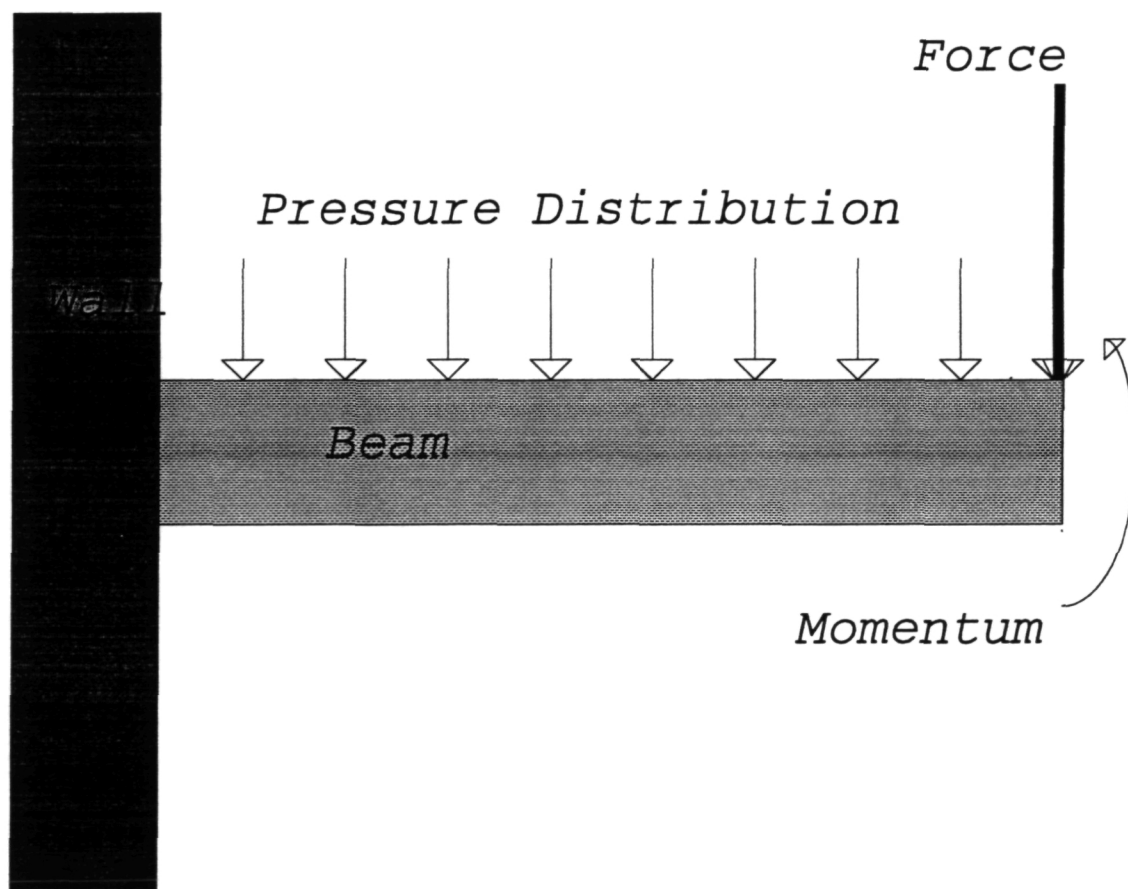


Figure 3-3. Theoretical model for the structural analysis

Chapter 4

TEST MODEL

In this chapter, the final details of the test model are discussed. To integrate into the tunnel environment, a few modifications on the test model are incorporated. However, the basic features of the test model are kept within the design limits that are specified in Chap. 4. The test model consists of two parts, the support mechanism and the test unit. The support mechanism (Fig. 4-1) consists of four components: the base plate, the bracket, the support tube, and the flow regulator. The main objective of the support mechanism is to provide a firm support for the test unit in the test section. The detailed description of each component of the support mechanism as well as the test units are described in this chapter.

4-1. Base Plate

As illustrated in Fig.4-2, the base plate has a dimension of 10.5"x4"x0.75". Both upper halves of the edges (0.5"x4.5"x0.75") are removed to fit to the outer wall of the tunnel. The block, 0.4"x4"x0.75" along the upper half center of the base plate is removed so the body could be fitted. There are

four 0.25 inch diameter holes at each corner of the lower half of the base plate for mounting. A two inch diameter of the block in the lower half of the base plate is removed to reduce an unnecessary weight to the model. The edges of the base plate are smoothly contoured to disperse any stress concentration. The thickness of 0.75" is selected to provide a greater contact area to the bracket for effective absorption of the loads/stresses generated from the test section.

4-2. Bracket

The bracket (Fig. 4-3) is designed to suspend three components together; the base plate, the support tube, and the flow regulator. In the experiments, since the bracket is submerged into the supersonic flow (but not necessarily in the test section), two main features are incorporated in design.

First, the inclined configuration of the bracket is implemented. This configuration is adapted because of the limit in the maximum cross sectional area for the test object, the considerable distance between the base plate and the test section, and the drag and stress considerations. In the supersonic flow, the flow velocity in the vicinity of the bracket could be divided/analyzed into two components, the tangential velocity and the normal velocity. Since only the normal velocity along the bracket would directly affect the formation of the shock wave, if an optimal bracket angle is selected, the shock would not be formed in the vicinity of the bracket (normal velocity is less than Mach 1);

consequently, low drag (pressure load) and stress along the bracket would result. Although the inclined bracket configuration contributes many solutions to the problems, the angle of the bracket is limited to 24° due to the minimum deflection requirement.

Last, the sharp edge configuration is incorporated along the outer boundary of the bracket to eliminate the formation of vorticities. The formation of vorticities in the flow introduces fluctuations in external pressure measurements and increases structural stress. With the sharp edge configuration, the bracket would suffer lower structural stress. Finally, the bracket has a thickness of 0.5 inches in compromise between the weight and the minimum deflection requirement.

4-3. Support Tube

The support tube, as shown in Fig. 4-3, is designed to suspend the test unit during the experiments. The tube has dimensions of 5 inches length and 1 inch outer diameter and is mounted to the body. The tube is designed such that the first three inches of the support tube has a $7/8$ inch internal diameter, whereas the last two inches of the tube has a $3/4$ inch internal diameter. Also, two distinctive internal diameters are incorporated in designing the support tube. In essence, with the Larger Internal Diameter (LID), the test unit would be inserted into the support tube, whereas the Smaller Internal Diameter (SID) prevents any further slide of the test unit into the support tube.

LID has a three inch length to increase the contact area between the test unit and the support tube. In consequence, the lateral and rotational movements by the test units during the tunnel operation are prevented. The internal edge where two internal diameters meet is smoothly contoured to fit to the end of the test unit. This is necessary, because the discontinuity in internal surface could trigger a flow separation which could introduce fluctuations in data.

4-4. Flow Regulator

The flow regulator (Figs. 4-3 and 4-4) consists of three components, a cone, a thread, and a circular block. The cone, which has a length of 1.4 inches with a half angle of 20° , is designed to regulate internal mass flow rate. The half angle of 20° is selected to smoothly contour the internal flow to the outlet. To regulate the internal flow rate, the thread is incorporated to provide the lateral movements of the cone. A 1/4-28 type thread is selected to prevent vibrational movements of the cone. Also, to control the location of the cone relative to the support tube, scale marks are added on one side of the thread where it was flattened. In addition, to maintain the rod and the cone steadily along the axial centerline of the support tube, a circular block is introduced. A circular block, which has dimensions of a 0.5 inch outer diameter, a 3.5 inch length, and a 1/4-28 type internal thread, is attached to the bracket to provide the firm support of the flow regulator.

4-5. Test Units

As illustrated in Fig. 4-5, the test unit has a circular configuration with the $7/8$ inches outer diameter and the $3/4$ inches inner diameter. These diameters are selected to fit smoothly into the fitting unit. Accordingly, the test unit has a 4 inch length. In essence, the first one inch of the test unit is designed to expose to the supersonic flow, whereas the last three inches of the unit is designed to insert into the fitting unit. Also, the test unit has the scale marks inscribed around an outer surface for the incremental rotations one inch away from the inlet entrance. For the tests, each deflector configuration is added to the test unit. In the experiments, two sets of the deflector configuration variation are investigated. Specific dimensions of each set are as follows.

1. A simple circular tube is selected with the deflector lengths of 10, 25, and 50 percents of the inner diameter length. The deflector has a zero frontal width and the 20.83 percent base width of the outer circumference (see Fig. 4-5 for terminology). These are labeled as the Test Configuration #1-1, #1-2, and #1-3 respectively.
2. A simple circular tube is selected with the deflector base widths of 37.5, 50.0, and 62.5 percents of the outer circumference. The deflector has a zero frontal width and a 73.4 percent deflector length of the inner diameter length (see Fig. 4-5 for terminology). These are labeled as the Test Configuration #2-1, #2-2, and #2-3 respectively.

In addition, a circular block tube and a simple circular tube without a deflector are experimented for validations. In the experiments, the data are collected at every 45° incremental rotation of the test unit.

4-6. Pressure Taps

In the experiments, four thin walled 0.1 inch internal diameter tubes are utilized for the pressure measurements. The tubes are made of alloy steel and are chosen for its durability. Relatively larger internal diameter tubes are selected to minimize the pressure settling time. Two of the four pressure tubes are attached on top of the support tube to measure the external stagnation and static pressures. The external pressure probes are located 0.4 inches above the support tube and are 0.4 inches apart from each other. The stagnation pressure probe is located 0.3 inches behind of the inlet cowl lip, whereas the static pressure probe is located 0.7 inches behind the inlet cowl lip. To reduce the effects of the probe misalignment, the two hole static pressure probe is implemented for the experiments. For the internal static pressure measurements, the tube is installed on the internal surface of the support tube four inches away from the entrance. Finally, for the internal stagnation pressure measurements, the tube is installed on the tip of the cone.

4-7. Final Over View

The final layout of the components for the experiment is illustrated in Fig. 4-6. In assembly process, due to heavy weights, larger pieces are bolted together for the rigidity, whereas the smaller components are welded together. Overall, the support mechanism and the test unit performed superbly during the experiments.

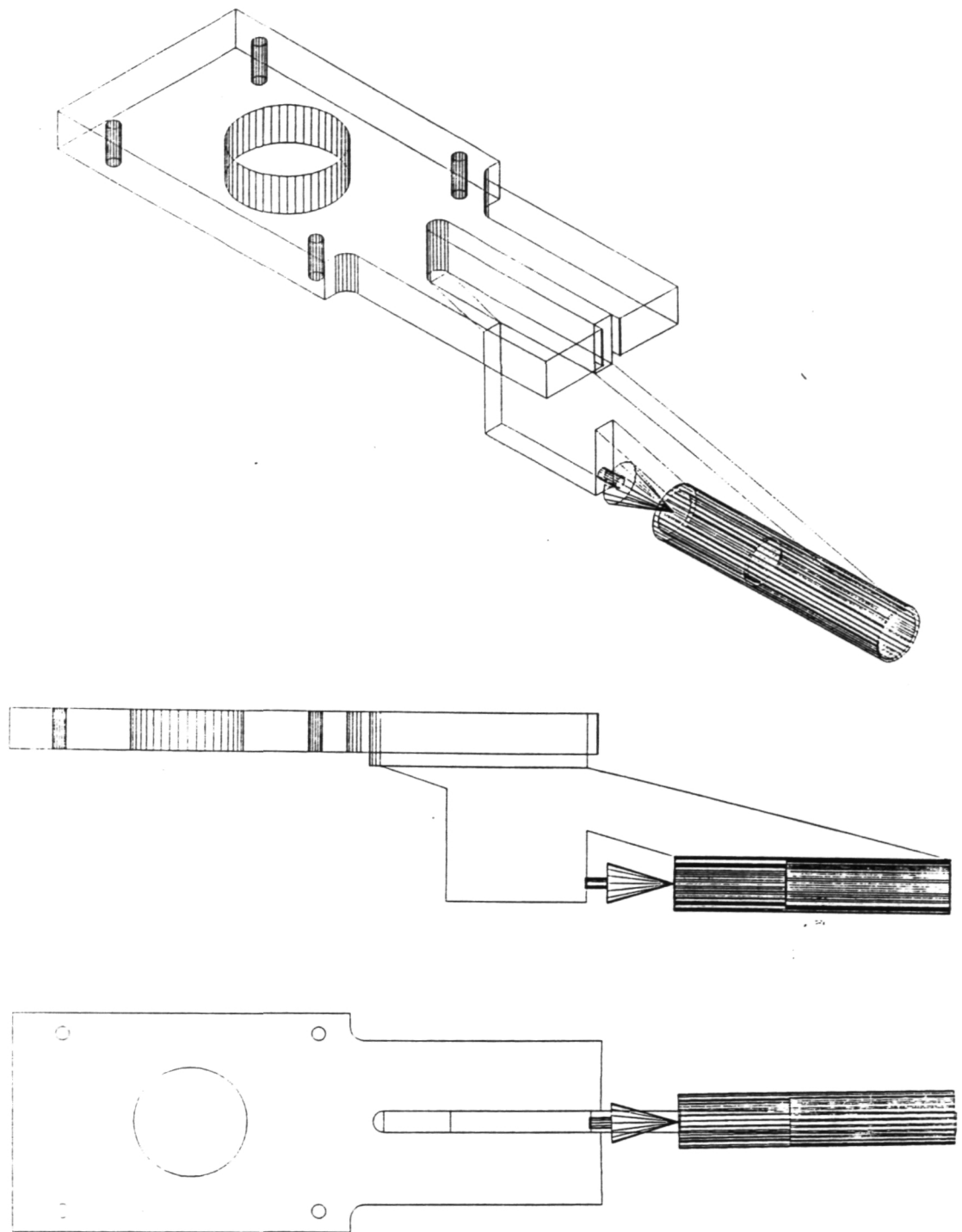


Figure 4-1. Schematic of the support mechanism.

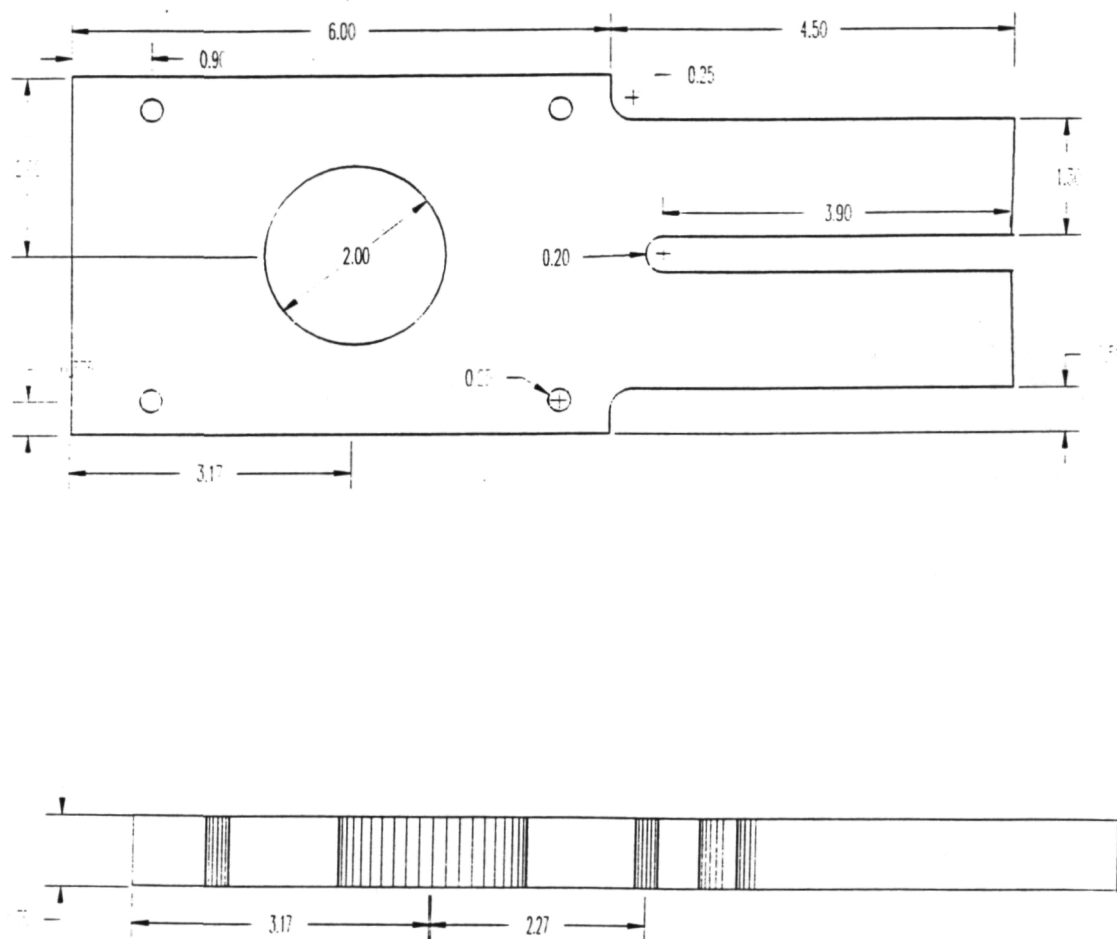


Figure 4-2. Schematic of the support mechanism base plate.

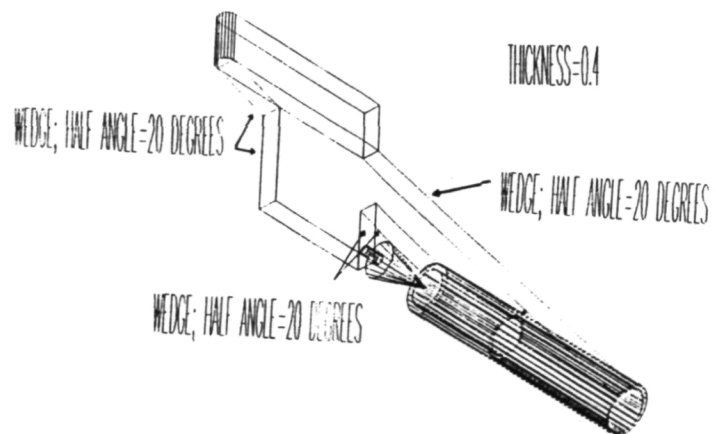
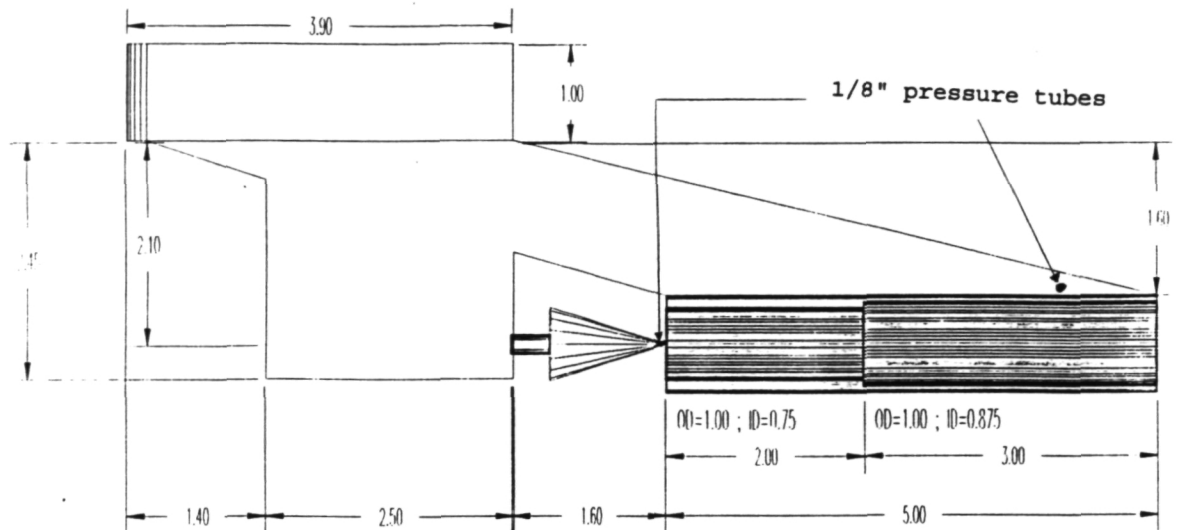


Figure 4-3. Schematic of the bracket and the support tube.

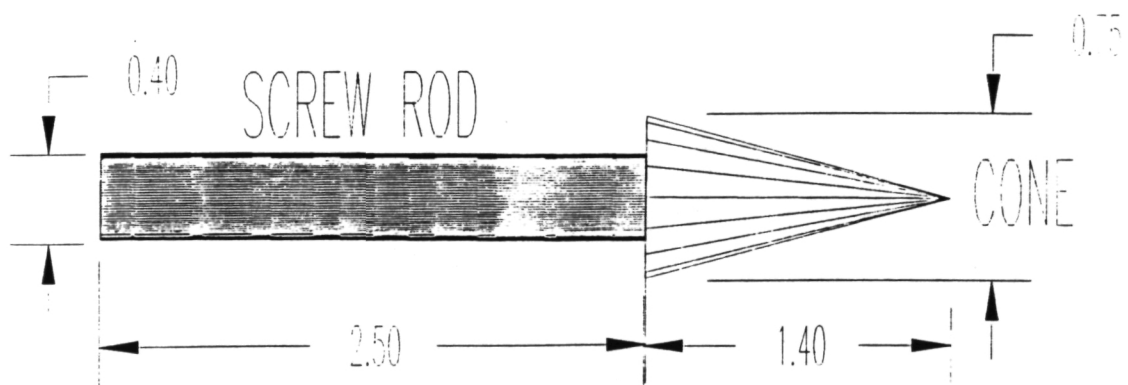


Figure 4-4. Schematic of the flow regulator.

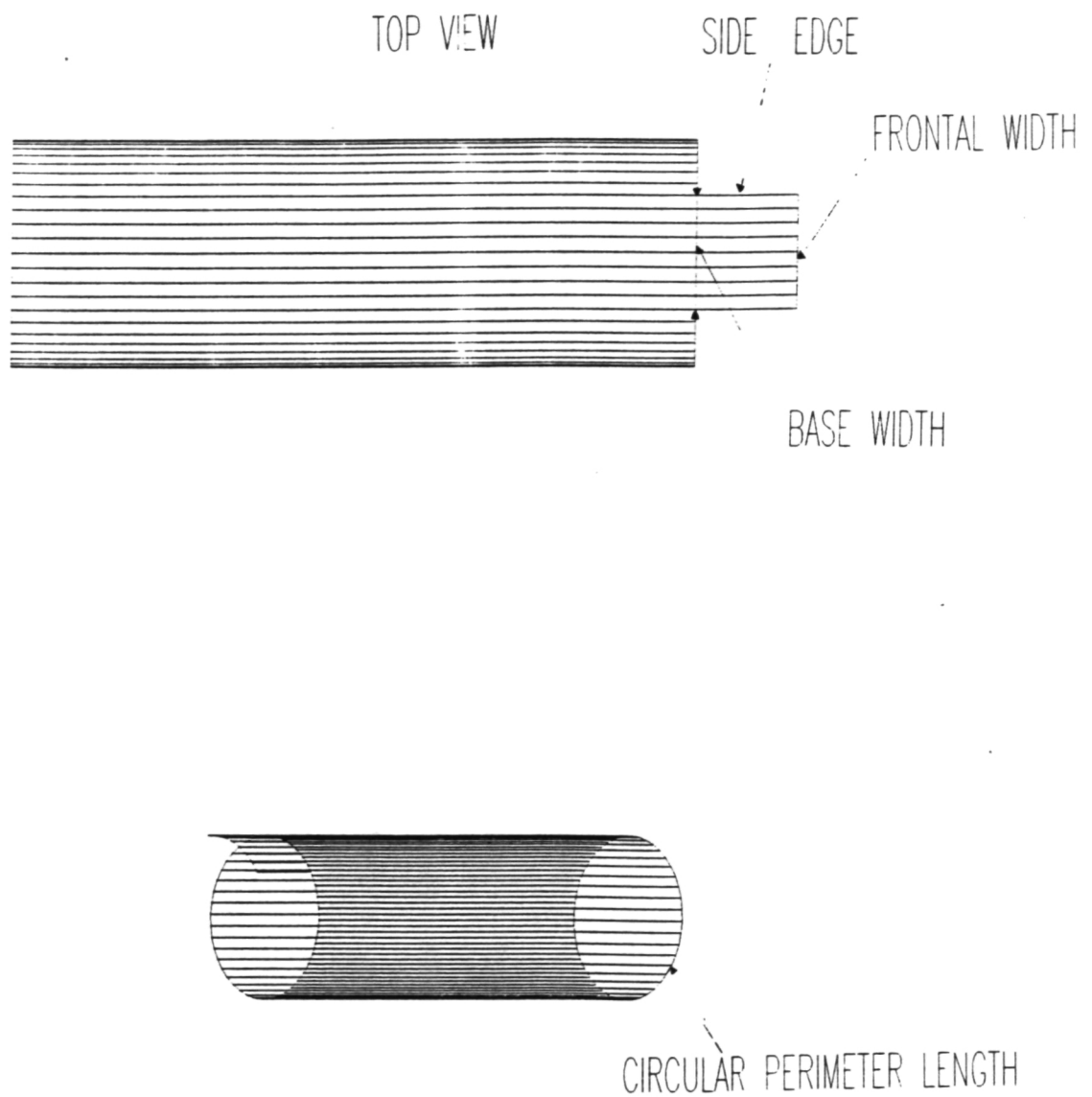
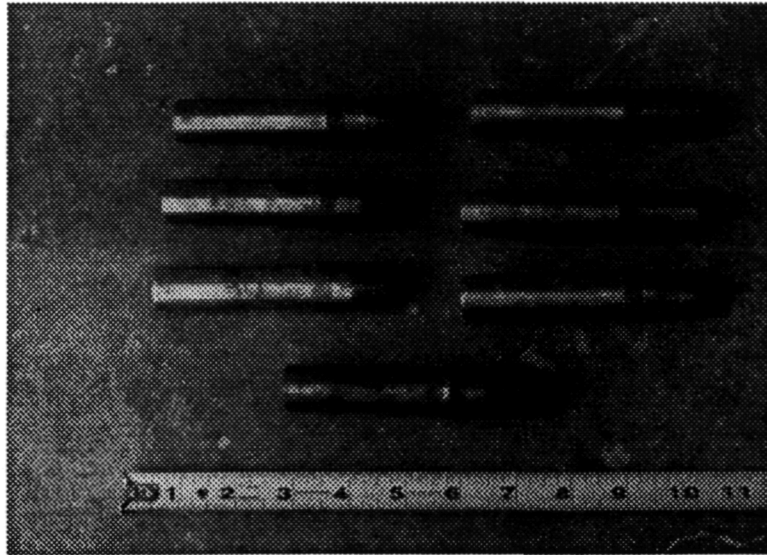
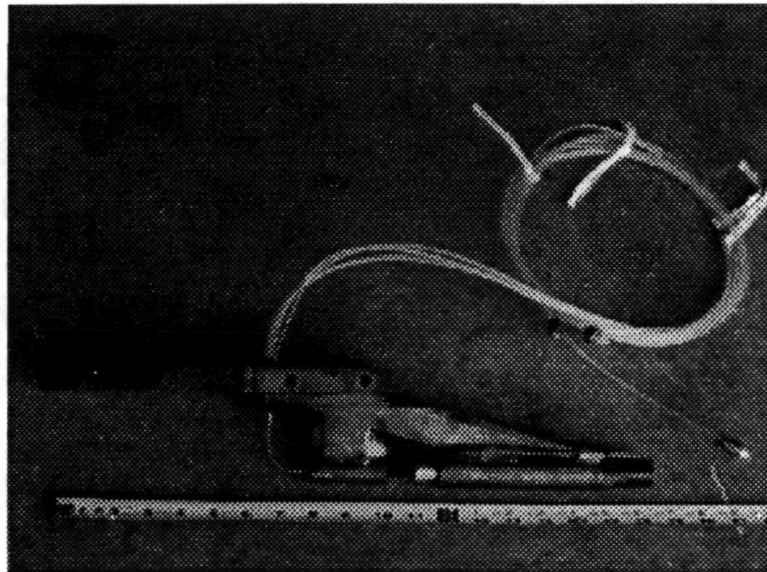


Figure 4-5. Schematic of the test unit.



A) Test Units



B) Support Mechanism

Figure 4-6. Photographic view of the support mechanism and the test units.

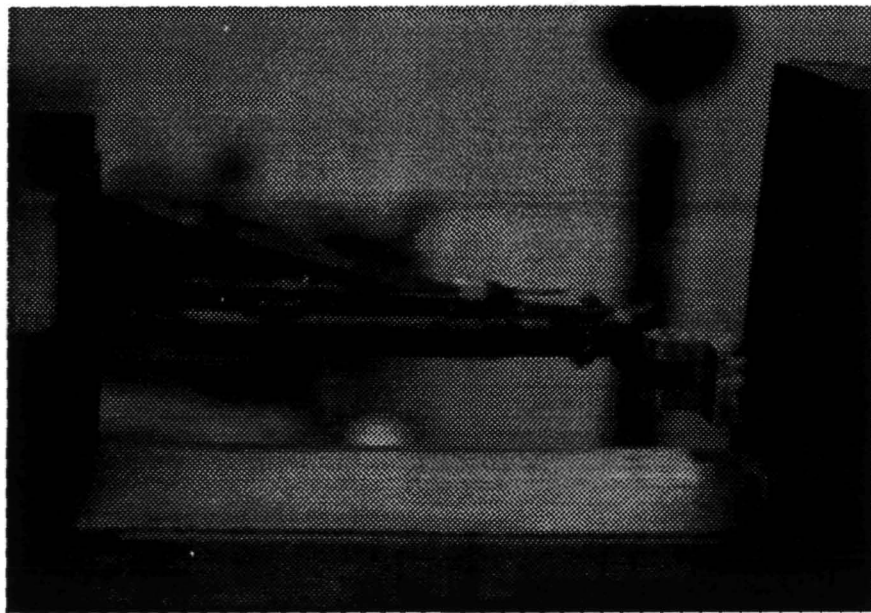


Figure 4-7. Photographic view of the support mechanism in tunnel.

Chapter 5

EXPERIMENTAL RESULTS

In this chapter, the experimental results are presented. First, the unsteadiness in stagnation pressure and the non-dimensional form of the pressure measurements are addressed. Then, the assumptions that applied for the flow analysis are introduced. Sequentially, to reduce the differences among the incoming flow conditions, the method of averaging data is discussed. Next, the evaluation of PSI-DPT is included along with a detailed description of errors and uncertainties in the measurements. Finally, the verification of the results and the tabulated form of the experimental data are presented.

5-1. Unsteadiness and Non-Dimensional Data

During the tunnel operations, the external stagnation pressure displays unsteadiness in the measurements. Figure 5-1 represents the typical external stagnation pressure measurements during the tunnel operation. When the flow is initiated, the stagnation pressure rises to its maximum, then, the pressure decreases steadily. In an ideal operation, the stagnation pressure remains steady after the peak point. The unsteadiness in the pressure

measurements result due to the improper function of the mechanical components in the tunnel. The pneumatic valve (Pilot valve) that is supposed to stabilize the preset stagnation pressure could not adequately respond to the storage pressure drop. Many diagnostic approaches are adopted to correct the problem; however, none are successful.

The unsteadiness in the stagnation pressure measurements creates significant problems in analyzing data. A steady decrease in the stagnation pressure results in unsteadiness in other pressure measurements as well. Since the pressure measurements vary with time, selecting the data that represents the actual flow conditions would be difficult. This poses a great difficulty in comparing with the experimental data. Hence, to make the data comparison compatible, the non-dimensionalization of the data is implemented as follows:

$$P^* = \frac{P_{\text{static (same flow)}}}{P_{\text{stagnation (same flow)}}} \quad (5-1)$$

Although the non-dimensional form of the data does not provide detailed variation in each pressure measurement, in these experiments, the sets of data serve two important objectives. First, the number of variables in data are reduced. Consequently, the reduction in the number of variables promote simpler analysis in the pressure measurements. Second, as indicated in Figs. 5-2 and 5-3, the region of steady measurements is obtained. In the figures,

the non-dimensional form of the pressure measurements are plotted against the sample time. The presence of the steady state region provides the cohesive and steady sets of the data, and thus, increases the compatibility in data comparison. The figures show that the sample time between four and six (after a peak) reveal the steady measurements of the non-dimensional pressure, hence, the experimental data for analysis are obtained from this time zone.

5-2. Flow Conditions and Assumptions

The raw data that is collected during the experiments represents the local flow conditions where the sensors encounter. Hence, to represent the actual flow conditions, the correction/adjustment on the raw data is required. Correcting the raw data is not an easy task: it requires detailed knowledge of the flow properties as well as their behaviors. Since the full disclosure of the flow field for correcting the data is not available and is difficult to obtain, the following assumptions are made for the correction without sacrificing the quality of the data.

First, since the perforated screens dampen much of disturbances, the conditions of compressible and uniform flow are applied. Second, the ideal gas law relation is implemented due to its low operating Mach number ($M=1.9$). Third, although the significant temperature gradient exists between the test section and the tunnel environment, the condition of adiabatic flow is

considered due to shortness of each tunnel operation time. Fourth, the conditions of inviscid and isentropic (before and after the shock waves) are applied. These are assumed, because the distance between the pressure probes are minimal where the pressure loss among the probes due to the friction is negligible. Also, it is assumed that the effects of the boundary layer growth along the surface of the part is negligible due to a short test configuration length (the actual test configuration segment length that is exposed to the flow). Finally, the pressure probe measurements in the supersonic flow is assumed to be undisturbed by the presence of the other probe. Further elaboration of the last assumption is as follows.

Figure 5-4 shows an oblique shock generates from the tip of the static probe and a bow shock generates from the stagnation probe. Two shock waves are seen to impinge onto each probe. Since the stagnation pressure probe (the actual position of the tap) is located in the outer range of an oblique shock disturbances, the primary concern is focused on the static pressure probe. It is noted that the oblique shock disturbances generated from the tip of the static probe are disregarded because of the minimal effects on the static pressure measurements [9]. However, the effects of the bow shock disturbances generate from the tip of stagnation probe on the static pressure measurements are different. The magnitude of disturbances is determined based on the distance between two external pressure probes. Since detailed information on the magnitude of disturbances on the static pressure

measurements by the bow shock is not available (due to equipment failure at the wind tunnel facility), and the distance between the probes is relatively apart, the magnitude of bow shock disturbances on the static probe is assumed small. However, further investigation on this assumption is recommended for future studies.

As previously mentioned, there are two external probes introduced in the flow for the external stagnation and static pressure measurements. When the probes are submerged into the supersonic flow, as shown in Fig. 5-4, a normal shock is formed in front of the stagnation probe. Since the subsonic flow region at the probe inlet is expected, the probe reads the subsonic stagnation pressure, instead of the supersonic stagnation pressure. Hence, to accurately present the actual pressure condition, the following equation is employed iteratively for the analysis.

$$\frac{P_{o2}}{P_1} = \left[1 + \frac{\gamma-1}{2} M_2^2 \right]^{\frac{\gamma}{\gamma-1}} \left[\frac{2\gamma M_1^2}{\gamma+1} - \frac{\gamma-1}{\gamma+1} \right] \quad (5-2)$$

5-3. Matching the Incoming Flow Conditions

In the experiments, the incoming flow conditions for every test are measured differently from each other. These differences result mainly from the uncontrollable surrounding tunnel environments, and consequently, contribute difficulties in the data comparison. In the experiments, the

nondimensional form of the incoming pressure (ratio between the external static pressure and the stagnation pressure) and the stagnation temperature are seen to fluctuate the most. Although both variables result in a significant influence on the measurements, greater emphasis is given on the external pressure than the temperature. This is because the fluctuation in nondimensional form of the external pressure contributes greater impact on the probe pressure measurements than the fluctuations in temperature.

To minimize the fluctuation in the incoming flow conditions and to make data comparisons compatible, two methods are suggested. First, the method of curve fitting is considered. The non-dimensional form of the experimental pressures are plotted against the incoming Mach numbers. However, the method is quickly abandoned due to the following reasons. First, there is not enough data for the plots. Second, the plotted data is concentrated in a confined area. Finally, when the plots are magnified, the data reveals a severe randomness in pattern, and consequently, a valid extrapolation of the data is impossible. The randomness in pattern is not the result of insufficient number of data points for the plot, instead, it is the result of flow characteristics.

The next in consideration is the method of averaging of the experimental data. Although the method is not very effective in matching the flow conditions, it reduces the range of difference in each data set. Hence, the method is implemented for the analysis. In this study, the experimental data

shows that the average differences among each set of data are less than three percent of the mean data.

5-4. Calibration of Pressure Transducer

To evaluate the accuracy in measurements, the PSI Digital Pressure Transmitter (PSI-DPT) is recalibrated. For the recalibration, PSI-DPT is compared with the MKS's Pressure Differential Transducer (Type 220 BH-2A7-A-10K). Figure 5-5 represents the experimental stagnation pressures measured by both transducers. The plot demonstrates that although there are significant differences on both ends of the graph, the measurements in the middle (by both transducers) display relatively small differences. Since the data for comparisons is retrieved from the region in the middle (between sample time 4 and 6), PSI-DPT displays relatively accurate pressure measurements for the experiments.

5-5. Error and Accuracy

In the experiment, the data inherits errors and consequently affects the accuracy of the measurements. Some of these errors are temporal and the others are more likely permanent. In the wind tunnel tests, the most visible temporal errors are displayed at the initial stage of the tunnel operation where greater fluctuations in pressure measurements are observed. These errors are presented due to unsteady movements in the mechanical components in the

tunnel. However, the effects of these errors disperse when the tunnel is run several times to "warm up" the tunnel components.

Concerning the permanent errors in the wind tunnel, four areas are focused upon. First, due to constant change in the tunnel environment, the transducer's pressure (voltage) reading at the static mode (the condition where the tunnel was operated) result in a small error. To minimize the error, the coefficients of each pressure port are required to recalibrate for each test. Since the recalibration of the coefficients for each experiment would require much effort and would not improve the accuracy significantly, the reevaluation of the coefficients for PSI-DPT at each test is not conducted. Second, because of the non-insulated storage tanks located outside of the facility, the density variation due to the temperature variation is observed. Third, due to misalignment on pressure probes, small errors in the pressure probe measurements are observed. Finally, due to its computer chip bit size, the data acquisition board displays an error in the measurements. At the static mode of operation, the output displays small non-zero readings in pressure even though the actual input pressure readings are zero.

Although these errors are visible, the effects of these errors are small compared to the effects of uncertainties in measurements. Consequently, these errors are neglected throughout the experiments. However, these errors

are persistently presented throughout the experiments and limit the accuracy on the measurements.

5-6. Uncertainty in Measurements

In every physical measurement, there are uncertainties in the measurements. The uncertainties in the measurements result due to the limited capacity, sensitivity, and range of the instruments, and consequently, confine the accuracy of results.

In the analysis, two types of uncertainties are considered; namely the uncertainty in direct measurement and the propagation of uncertainty [10]. Each has different characteristics and is derived differently. The uncertainty in direct measurement is presented due to the discrepancies in each experimental measurement. The uncertainty in direct is calculated based on the average deviation in each experimental measurement. The propagation of uncertainty in data is derived as a result of the uncertainty in each variable. For calculating the propagation of uncertainty, the fractional uncertainties of each variable are added. For further understanding on the uncertainty in direct measurement and the propagation of uncertainty, a sample calculation is included in Appendix C. In the experiments, unlike the errors mentioned in section 5-5, the effects of these uncertainties on final sets of data are considerable; therefore, these are presented in the final sets of data.

5-7. Verifications

For every experiment, the verification of the data is required to further strengthen the results. In this study, as previously mentioned, numerical analysis is originally introduced as a way to verify the results. However, due to inability to generate an appropriate grid, the verification of the experimental results with numerical solutions is not possible. Alternatively, the verification of results are conducted by comparing the pre-existing theoretical and experimental data. Since it is a difficult and time consuming task to verify every experimental result, two simple geometrical inlets are experimented for the comparisons. A flat circular block tube is introduced in the flow for visual comparison between the experimental shadowgraph and the pre-existing schlieren results. Also, a simple pitot tube is experimented to compare the experimental and theoretical results of the non-dimensional form of the internal pressure.

The verification of external results is demonstrated in Figs. 5-6a and 5-6b. The photo on the top represents the result that is obtained from the experimentation of a flat circular cylinder at Mach 1.9, whereas the photo on the bottom represents the result of a flat circular cylinder previously done by Van Dyke at Mach 2.0 [15]. Although there is a six percent difference in the test Mach number, in general, the characteristics of the shock wave formations in photos match with each other.

For verifying the internal pressure ratio, a pitot inlet is experimented. In Fig. 5-7, the experimented internal pressure ratio is plotted against the theoretical internal pressure ratio. Although there is a difference between the two results (less than 5 % difference), the results are within the range of uncertainties in the measurements. The small differences in these results are contributed mainly by the presence of the internal friction. Therefore, two results are assumed to be identical.

5-8. Experimental Data

In this section, the experimental data at Mach 1.9, and the internal Reynolds number between 1.12×10^3 and 1.35×10^3 are considered. For the pressure measurements, the dimensional and non-dimensional forms of the data at each angle of rotation are collectively tabulated. Also, the redefined total pressure recovery ratio (RTPRR) and the coefficient of the spillage drag [12] are included in tabulated form (see Tables). Redefinition of the total pressure recovery and the coefficient of the spillage drag are necessary due to non-dimensionalization of the pressure term. The mathematical equations for the new variables are defined as follows:

$$\text{RTPRR} = \frac{P_{o2} P_1}{P_{o1} P_2} \quad (5-3)$$

$$C_{\text{spillage drag}} = \frac{[P_i \gamma M_i^2 + (P_i - P_o)] A_i - P_o \gamma M_o^2 A_o}{q_o A_i} \quad (5-4)$$

where

$$q_o = \frac{1}{2} \gamma P_o M_o^2$$

The coefficient of the spillage drag could be rewritten as

$$C_{\text{spillage drag}} = \frac{2}{RTPRR} \frac{P_{o2}}{P_{o1}} \left[\frac{\gamma M_i^2 + 1}{\gamma M_o^2} - \frac{M_i}{M_o} \left(\frac{1 + \frac{\gamma - 1}{2} M_i^2}{1 + \frac{\gamma - 1}{2} M_o^2} \right)^{\frac{1}{2}} \right] - \frac{2}{\gamma M_o^2} \quad (5-5)$$

For the shock angle and the shock standoff distance of each test configuration, the shadowgraph photos are presented in Appendix A.

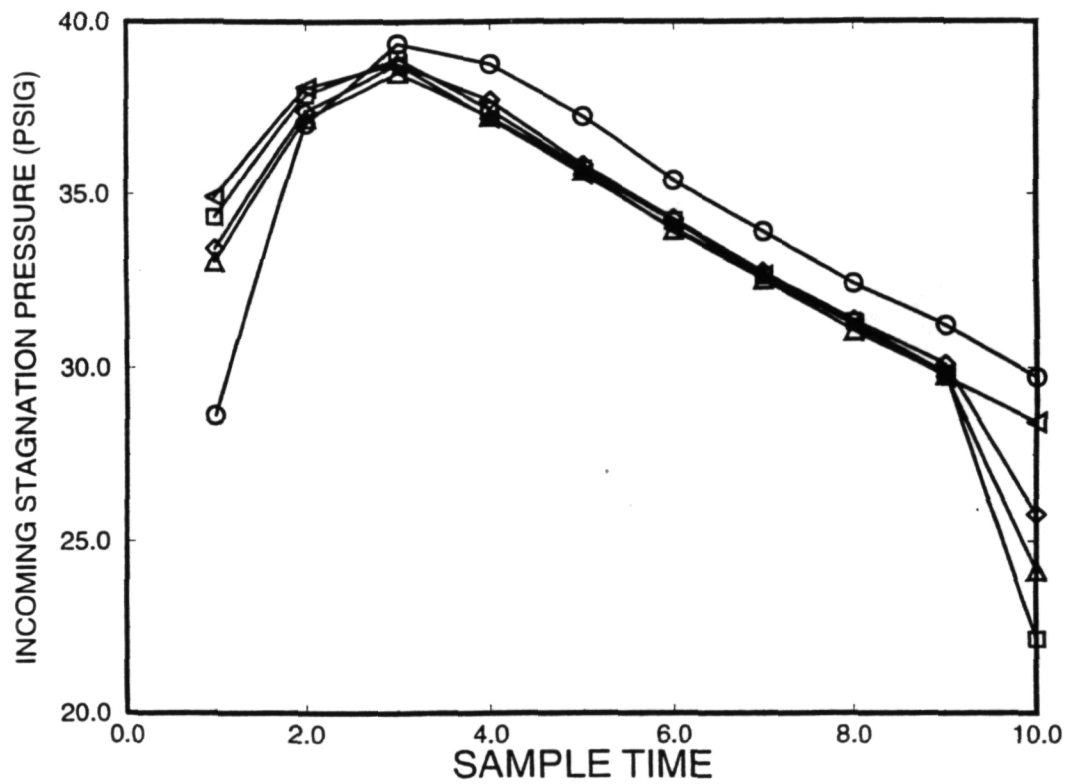


Figure 5-1. Typical stagnation pressure measurements during the tunnel operation.

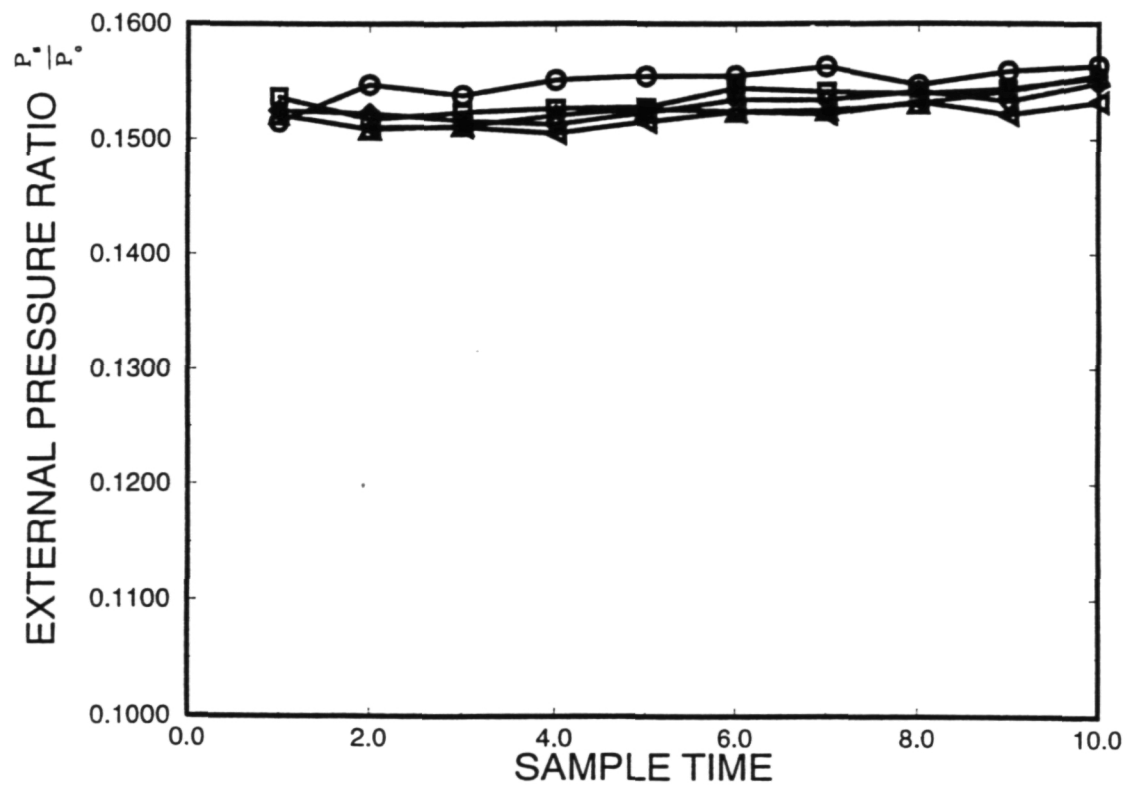


Figure 5-2. Typical non-dimensional external pressure measurements during the tunnel operation.

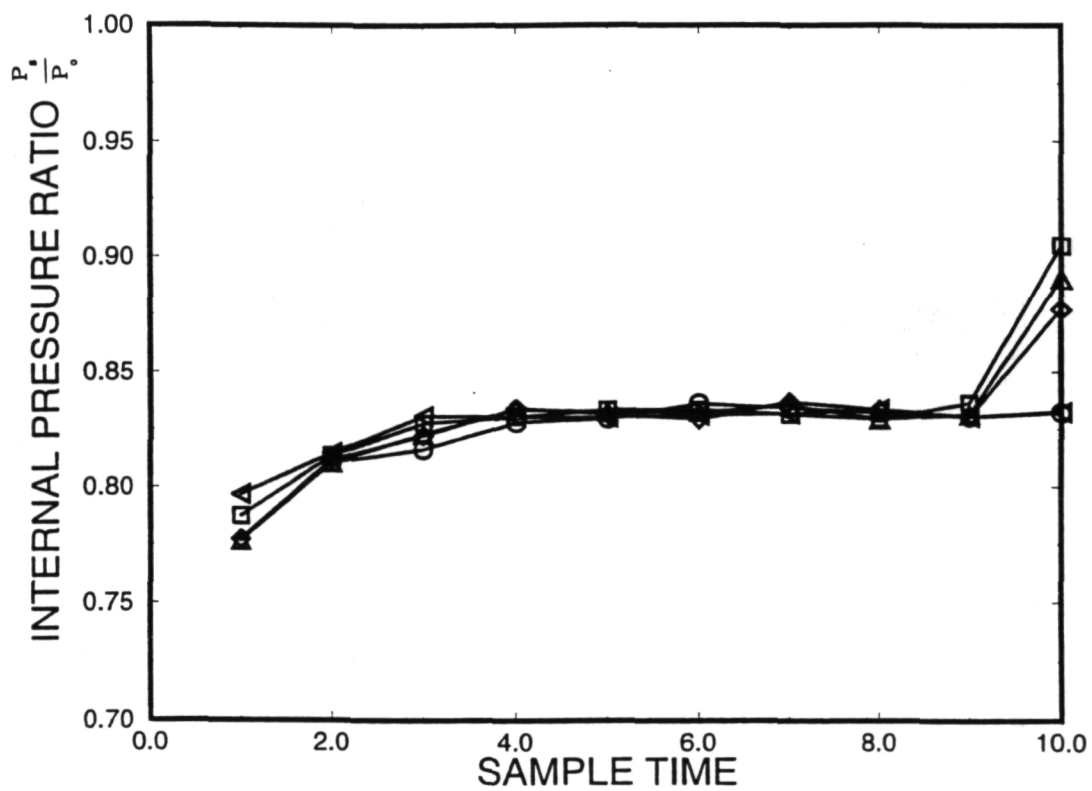


Figure 5-3. Typical non-dimensional internal pressure measurements during the tunnel operation.

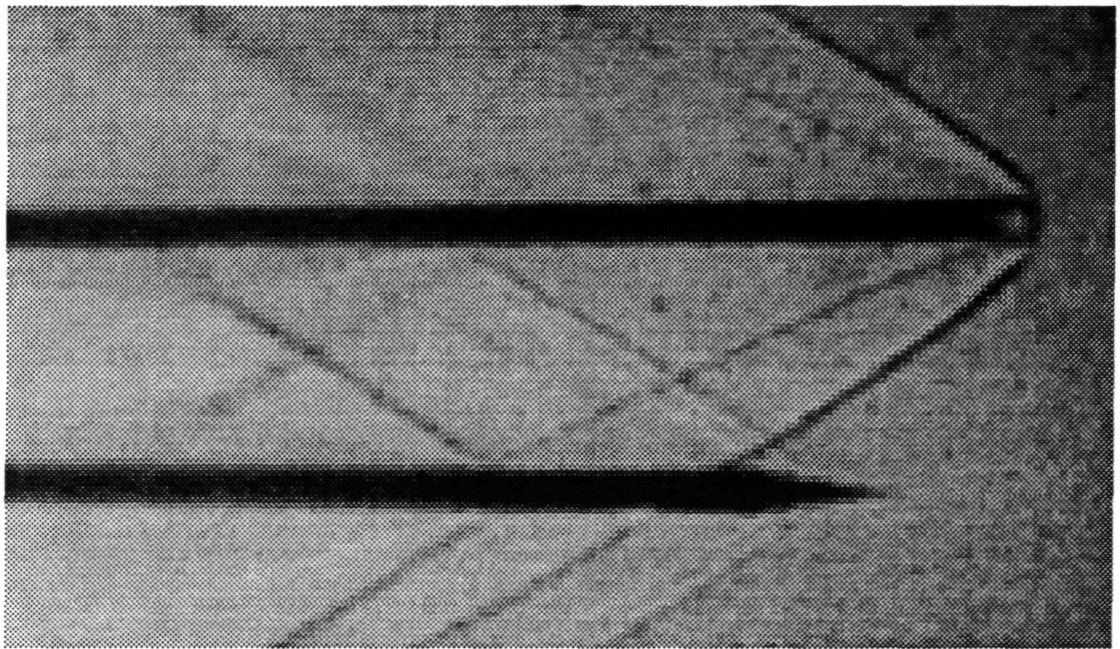


Figure 5-4. Shadowgraph photo of two external probes in supersonic flow.

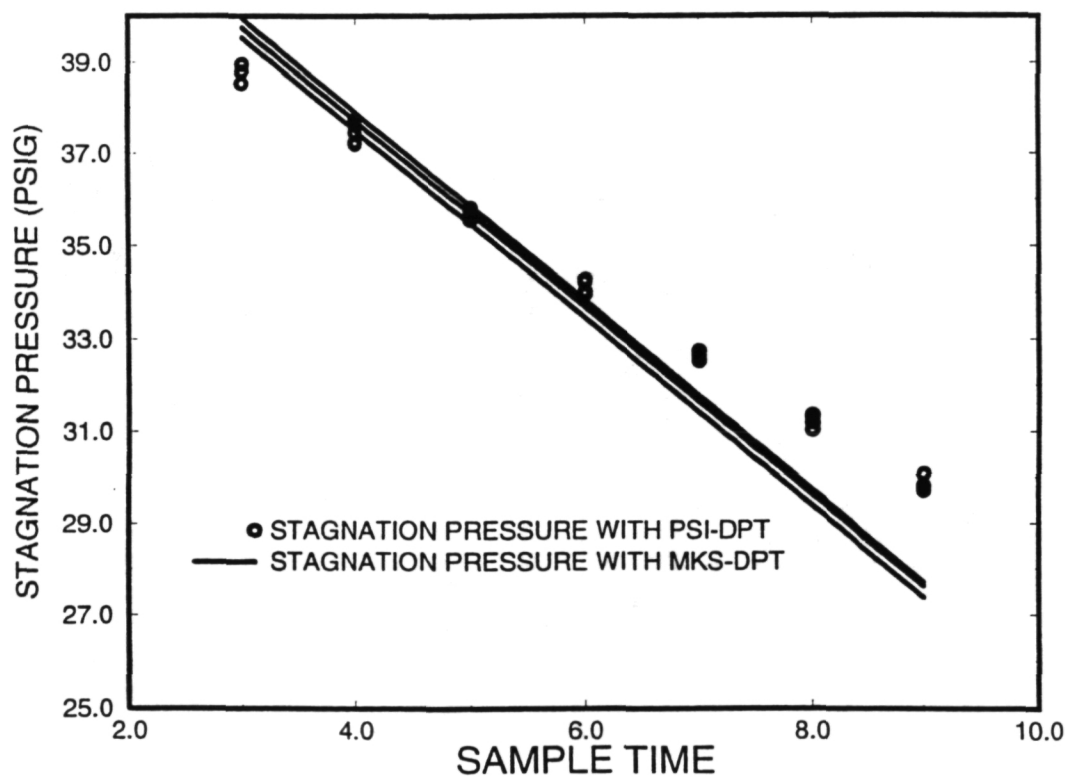
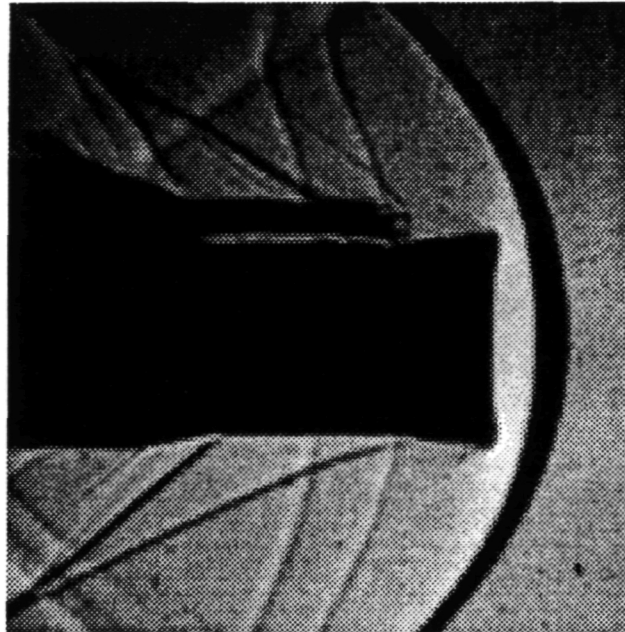
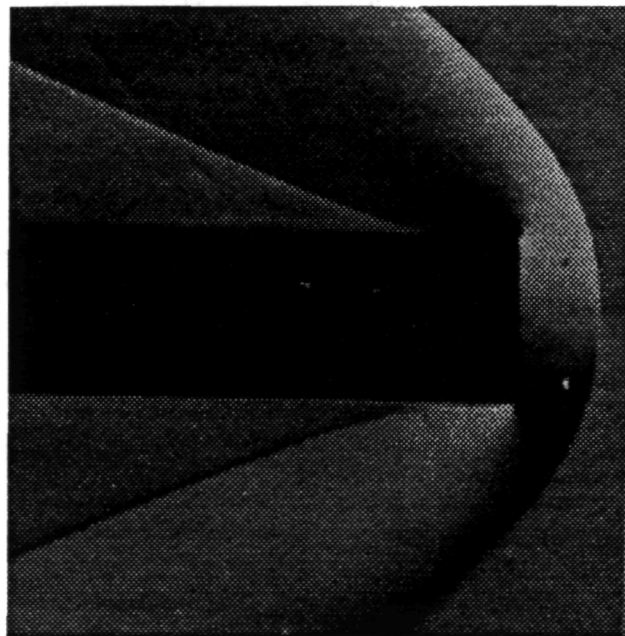


Figure 5-5. Stagnation pressure measurements with PSI-DPT and MKS-DPT.



A) Experimental result at Mach 1.9 (Shadowgraph).



B) Pre-existing result at Mach 2.0 (Schlieren) [17].

Figure 5-6. Photographic results for flat circular cylinder

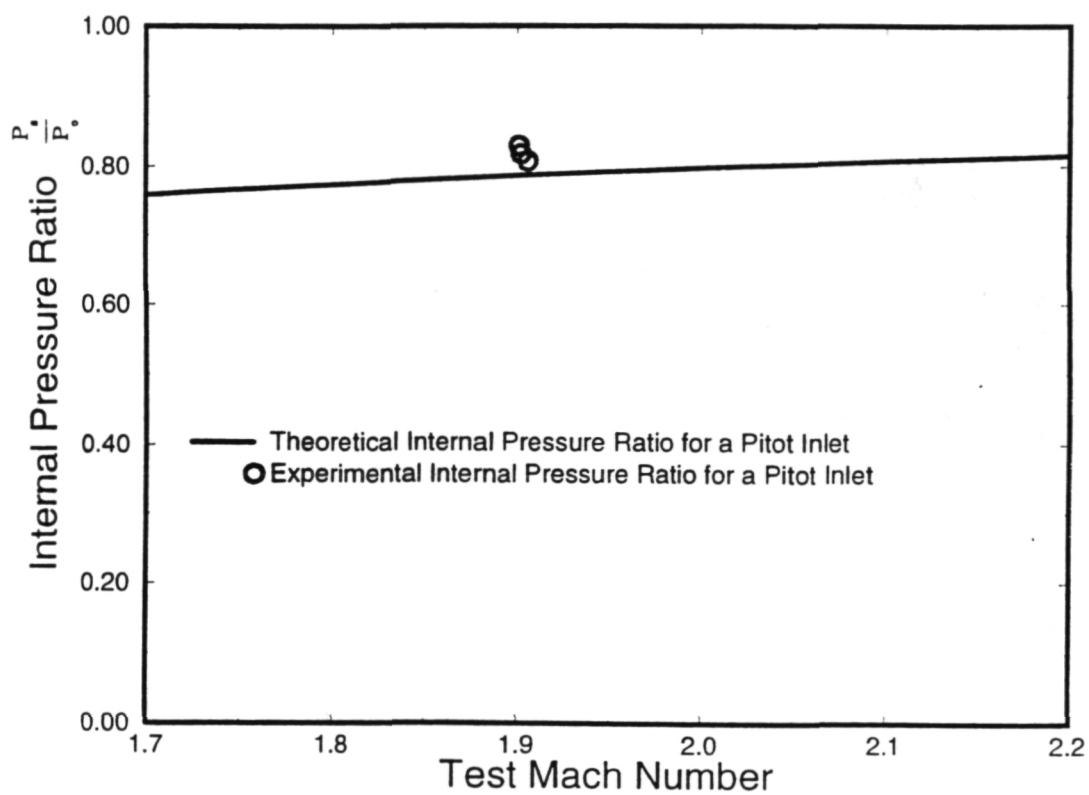


Figure 5-7. Theoretical and experimental comparison of internal pressure ratio for pitot type inlet.

Table 5-1. Experimental results for test configuration #1-1: Atmospheric pressure=14.914 Psia

ANGLE OF ROTATION (DEGREE)	TEST MACH NUMBER	PROBE 1 STATIC PRESSURE (PSIG)	PROBE 2 STAGNATION PRESSURE (PSIG)	EXTERNAL STAGNATION PRESSURE (PSIG)	EXTERNAL STATIC PRESSURE (PSIG)	INTERNAL STAGNATION PRESSURE (PSIG)	INTERNAL STATIC PRESSURE (PSIG)
0	1.886	-3.527	15.978	35.391	-7.246	23.469	17.188
0	1.887	-4.243	15.029	33.903	-7.484	22.347	16.171
0	1.883	-4.805	14.027	32.415	-7.662	21.276	15.202
45	1.886	-4.856	15.872	34.222	-7.424	22.602	16.364
45	1.886	-5.06	15.029	32.628	-7.662	21.48	15.348
45	1.884	-5.418	14.08	31.3	-7.84	20.459	14.428
90	1.882	-4.243	16.716	34.275	-7.365	22.857	16.413
90	1.882	-4.498	15.82	32.734	-7.603	21.48	15.541
90	1.879	-4.754	14.976	31.353	-7.781	20.408	14.525
135	1.885	-3.169	17.349	35.657	-7.187	23.878	17.381
135	1.878	-3.578	16.347	33.957	-7.365	22.653	16.364
135	1.879	-3.987	15.609	32.522	-7.603	21.429	15.445
180	1.873	-2.914	16.822	34.01	-7.306	22.653	16.316
180	1.87	-3.322	15.767	32.628	-7.484	21.582	15.445
180	1.877	-3.629	14.923	31.193	-7.781	20.408	14.525

Table 5-2. Experimental results for test configuration #1-2: Atmospheric pressure=14.663 Psia

ANGLE OF ROTATION (DEGREE)	TEST MACH NUMBER	PROBE 1 STATIC PRESSURE (PSIG)	PROBE 2 STAGNATION PRESSURE (PSIG)	EXTERNAL STAGNATION PRESSURE (PSIG)	EXTERNAL STATIC PRESSURE (PSIG)	INTERNAL STAGNATION PRESSURE (PSIG)	INTERNAL STATIC PRESSURE (PSIG)
0	1.893	-4.191	21.093	35.71	-7.068	24.082	16.945
0	1.886	-4.549	20.091	34.01	-7.246	22.908	15.929
0	1.884	-4.754	19.089	32.628	-7.424	21.48	14.96
45	1.896	-5.878	17.454	35.923	-7.068	24.235	17.139
45	1.889	-6.03	16.4	34.222	-7.246	22.653	16.074
45	1.889	-6.27	15.503	32.628	-7.484	21.633	15.106
90	1.894	-4.958	18.351	35.763	-7.068	24.031	17.042
90	1.889	-5.214	17.191	34.169	-7.246	22.449	16.074
90	1.888	-5.469	16.136	32.522	-7.484	21.531	15.106
135	1.889	-3.783	18.087	35.338	-7.068	23.571	16.897
135	1.888	-4.089	16.98	33.744	-7.306	22.5	15.88
135	1.885	-4.396	15.925	32.362	-7.484	21.582	15.009
180	1.889	-3.527	17.824	35.338	-7.068	23.725	16.849
180	1.887	-3.834	16.874	33.691	-7.306	22.449	15.88
180	1.888	-4.191	15.872	32.203	-7.543	21.378	14.815

Table 5-3. Experimental results for test configuration #1-3: Atmospheric Pressure=14.779 Psia

ANGLE OF ROTATION (DEGREE)	TEST MACH NUMBER	PROBE 1 STATIC PRESSURE (PSIG)	PROBE 2 STAGNATION PRESSURE (PSIG)	EXTERNAL STAGNATION PRESSURE (PSIG)	EXTERNAL STATIC PRESSURE (PSIG)	INTERNAL STAGNATION PRESSURE (PSIG)	INTERNAL STATIC PRESSURE (PSIG)
0	1.886	-5.469	19.986	36.135	-7.009	23.265	16.219
0	1.888	-4.754	22.78	37.889	-6.771	24.031	18.156
0	1.887	-4.958	21.515	33.531	-7.424	20.561	16.316
45	1.904	-6.389	19.511	36.932	-7.127	23.163	17.381
45	1.9	-6.645	18.456	35.391	-7.306	22.449	16.413
45	1.896	-6.849	17.138	30.343	-8.018	17.959	14.331
90	1.9	-5.725	19.458	37.836	-6.949	23.622	17.962
90	1.902	-5.827	18.298	36.348	-7.187	22.653	16.945
90	1.896	-6.389	17.296	31.937	-7.781	19.082	15.251
135	1.899	-4.549	18.351	36.135	-7.187	22.704	16.849
135	1.898	-4.907	17.191	34.488	-7.424	21.735	15.832
135	1.899	-5.163	16.136	32.575	-7.721	19.898	14.912
180	1.884	-4.447	17.824	34.86	-7.187	22.296	16.364
180	1.88	-4.856	16.716	33.425	-7.365	21.378	15.348
180	1.881	-5.316	15.978	31.884	-7.603	19.694	14.428

Table 5-4. Experimental results for test configuration #2-1: Atmospheric Pressure=14.856 Psia

ANGLE OF ROTATION (DEGREE)	TEST MACH NUMBER	PROBE 1 STATIC PRESSURE (PSIG)	PROBE 2 STAGNATION PRESSURE (PSIG)	EXTERNAL STAGNATION PRESSURE (PSIG)	EXTERNAL STATIC PRESSURE (PSIG)	INTERNAL STAGNATION PRESSURE (PSIG)	INTERNAL STATIC PRESSURE (PSIG)
0	1.889	-3.936	23.993	36.826	-7.009	23.776	17.188
0	1.889	-3.936	23.993	36.826	-7.009	23.776	17.188
0	1.888	-4.345	22.78	35.179	-7.246	22.755	16.122
45	1.885	-4.958	23.624	35.338	-7.187	22.449	16.316
45	1.887	-5.367	22.2	33.957	-7.424	21.276	15.348
45	1.887	-5.367	22.2	33.957	-7.424	21.276	15.348
90	1.89	-5.827	20.407	32.628	-7.662	19.847	14.718
90	1.886	-6.134	19.353	31.14	-7.84	19.949	13.798
90	1.883	-6.287	18.14	29.758	-8.018	18.827	12.975
135	1.885	-5.316	20.777	33.053	-7.543	21.071	14.767
135	1.886	-5.623	19.617	31.512	-7.781	19.898	13.895
135	1.882	-5.878	18.615	30.077	-7.959	18.622	13.072
180	1.89	-4.14	22.675	35.763	-7.187	23.061	16.607
180	1.886	-4.498	21.462	33.903	-7.424	22.092	15.541
180	1.889	-4.805	20.355	32.522	-7.662	21.122	14.67

Table 5-5. Experimental results for test configuration #2-2: Atmospheric Pressure=14.914 Psia

ANGLE OF ROTATION (DEGREE)	TEST MACH NUMBER	PROBE 1 STATIC PRESSURE (PSIG)	PROBE 2 STAGNATION PRESSURE (PSIG)	EXTERNAL STAGNATION PRESSURE (PSIG)	EXTERNAL STATIC PRESSURE (PSIG)	INTERNAL STAGNATION PRESSURE (PSIG)	INTERNAL STATIC PRESSURE (PSIG)
0	1.883	-2.3	26.419	39.377	-6.593	26.684	19.027
0	1.883	-2.3	26.419	39.377	-6.593	26.684	19.027
0	1.875	-2.709	25.206	37.57	-6.771	25.153	17.962
45	1.879	-4.038	24.837	37.145	-6.89	24.796	17.575
45	1.877	-4.243	23.361	35.444	-7.127	22.245	16.461
45	1.871	-4.447	22.306	33.797	-7.306	21.939	15.445
90	1.883	-4.498	24.679	39.005	-6.652	25.51	18.834
90	1.882	-4.958	23.677	37.358	-6.89	24.898	17.817
90	1.872	-5.316	22.622	35.444	-7.068	23.01	16.703
135	1.878	-4.396	24.626	37.836	-6.771	24.597	18.107
135	1.875	-4.805	23.202	36.082	-7.009	23.418	17.042
135	1.87	-5.06	22.042	34.541	-7.187	21.939	15.977
180	1.877	-4.396	21.937	35.072	-7.187	23.061	16.461
180	1.876	-4.754	20.566	33.478	-7.424	21.837	15.348
180	1.87	-5.06	19.353	31.884	-7.603	20.765	14.476

Table 5-6. Experimental results for test configuration #2-3: Atmospheric Pressure=14.798 Psia

ANGLE OF ROTATION (DEGREE)	TEST MACH NUMBER	PROBE 1 STATIC PRESSURE (PSIG)	PROBE 2 STAGNATION PRESSURE (PSIG)	EXTERNAL STAGNATION PRESSURE (PSIG)	EXTERNAL STATIC PRESSURE (PSIG)	INTERNAL STAGNATION PRESSURE (PSIG)	INTERNAL STATIC PRESSURE (PSIG)
0	1.898	-2.096	22.991	35.657	-7.246	23.725	17.042
0	1.9	-3.067	21.989	34.222	-7.484	23.98	15.977
0	1.895	-3.476	20.566	32.628	-7.662	21.122	15.057
45	1.9	-3.966	21.093	36.986	-7.068	25.051	17.817
45	1.901	-4.269	20.091	35.444	-7.306	23.418	16.849
45	1.899	-4.579	19.089	33.744	-7.543	22.143	15.88
90	1.899	-3.016	21.937	35.338	-7.306	23.622	16.752
90	1.895	-3.476	20.618	33.85	-7.484	22.449	15.783
90	1.896	-5.06	19.669	32.309	-7.721	21.888	14.767
135	1.896	-4.345	22.359	35.072	-7.306	23.214	16.655
135	1.894	-4.703	21.198	33.372	-7.543	22.245	15.59
135	1.89	-5.112	20.091	31.884	-7.721	21.122	14.718
180	1.888	-4.805	22.253	34.86	-7.246	23.827	16.364
180	1.887	-5.009	21.251	33.213	-7.484	22.398	15.445
180	1.886	-5.316	20.091	31.618	-7.721	20.969	14.573

Table 5-7. Non-dimensional results for test configuration #1-1.

ANGLE OF ROTATION (DEGREE)	TEST MACH NUMBER	PROBE PRESSURE RATIO	EXTERNAL PRESSURE RATIO	INTERNAL PRESSURE RATIO
0	1.886	0.369	0.152	0.836
0	1.887	0.356	0.152	0.834
0	1.883	0.349	0.153	0.832
45	1.886	0.327	0.152	0.834
45	1.886	0.329	0.153	0.832
45	1.884	0.328	0.153	0.83
90	1.882	0.337	0.153	0.829
90	1.882	0.339	0.153	0.837
90	1.879	0.34	0.154	0.833
135	1.885	0.364	0.153	0.833
135	1.878	0.363	0.154	0.833
135	1.879	0.358	0.154	0.835
180	1.873	0.378	0.156	0.831
180	1.87	0.378	0.156	0.832
180	1.877	0.378	0.155	0.833

Table 5-8. Non-dimensional results for test configuration #1-2.

ANGLE OF ROTATION (DEGREE)	TEST MACH NUMBER	PROBE PRESSURE RATIO	EXTERNAL PRESSURE RATIO	INTERNAL PRESSURE RATIO
0	1.893	0.293	0.151	0.816
0	1.886	0.291	0.152	0.814
0	1.884	0.294	0.153	0.82
45	1.896	0.274	0.15	0.818
45	1.889	0.278	0.152	0.824
45	1.889	0.278	0.152	0.82
90	1.894	0.294	0.151	0.819
90	1.889	0.297	0.152	0.828
90	1.888	0.299	0.152	0.822
135	1.889	0.332	0.152	0.825
135	1.888	0.334	0.152	0.822
135	1.885	0.336	0.153	0.819
180	1.889	0.343	0.152	0.821
180	1.887	0.343	0.152	0.823
180	1.888	0.343	0.152	0.818

Table 5-9. Non-dimensional results for test configuration #1-3.

ANGLE OF ROTATION (DEGREE)	TEST MACH NUMBER	PROBE PRESSURE RATIO	EXTERNAL PRESSURE RATIO	INTERNAL PRESSURE RATIO
0	1.886	0.268	0.153	0.815
0	1.888	0.267	0.152	0.849
0	1.887	0.271	0.152	0.88
45	1.904	0.245	0.148	0.848
45	1.9	0.245	0.149	0.838
45	1.896	0.248	0.15	0.889
90	1.9	0.264	0.149	0.853
90	1.902	0.271	0.148	0.848
90	1.896	0.262	0.15	0.887
135	1.899	0.309	0.149	0.844
135	1.898	0.309	0.149	0.838
135	1.899	0.311	0.149	0.856
180	1.884	0.317	0.153	0.84
180	1.88	0.315	0.154	0.833
180	1.881	0.308	0.154	0.847

Table 5-10. Non-dimensional results for test configuration #2-1.

ANGLE OF ROTATION (DEGREE)	TEST MACH NUMBER	PROBE PRESSURE RATIO	EXTERNAL PRESSURE RATIO	INTERNAL PRESSURE RATIO
0	1.889	0.281	0.152	0.829
0	1.889	0.281	0.152	0.829
0	1.888	0.279	0.152	0.824
45	1.885	0.257	0.153	0.836
45	1.887	0.256	0.152	0.836
45	1.887	0.256	0.152	0.836
90	1.89	0.256	0.152	0.852
90	1.886	0.255	0.153	0.823
90	1.883	0.26	0.153	0.826
135	1.885	0.268	0.153	0.825
135	1.886	0.268	0.153	0.827
135	1.882	0.268	0.153	0.834
180	1.89	0.286	0.152	0.83
180	1.886	0.285	0.152	0.823
180	1.889	0.285	0.152	0.821

Table 5-11. Non-dimensional results for test configuration #2-2.

ANGLE OF ROTATION (DEGREE)	TEST MACH NUMBER	PROBE PRESSURE RATIO	EXTERNAL PRESSURE RATIO	INTERNAL PRESSURE RATIO
0	1.883	0.305	0.153	0.816
0	1.883	0.305	0.153	0.816
0	1.875	0.304	0.155	0.821
45	1.879	0.274	0.154	0.818
45	1.877	0.279	0.155	0.844
45	1.871	0.281	0.156	0.824
90	1.883	0.263	0.153	0.835
90	1.882	0.258	0.154	0.822
90	1.872	0.256	0.156	0.834
135	1.878	0.266	0.154	0.836
135	1.875	0.265	0.155	0.834
135	1.87	0.267	0.156	0.838
180	1.877	0.285	0.155	0.826
180	1.876	0.286	0.155	0.823
180	1.87	0.288	0.156	0.824

Table 5-12. Non-dimensional results for test configuration #2-3.

ANGLE OF ROTATION (DEGREE)	TEST MACH NUMBER	PROBE PRESSURE RATIO	EXTERNAL PRESSURE RATIO	INTERNAL PRESSURE RATIO
0	1.898	0.336	0.15	0.827
0	1.9	0.319	0.149	0.794
0	1.895	0.32	0.15	0.831
45	1.9	0.302	0.149	0.818
45	1.901	0.302	0.149	0.828
45	1.899	0.302	0.149	0.88
90	1.899	0.321	0.149	0.821
90	1.895	0.32	0.15	0.821
90	1.896	0.283	0.15	0.806
135	1.896	0.281	0.15	0.827
135	1.894	0.28	0.151	0.82
135	1.89	0.278	0.152	0.822
180	1.888	0.27	0.152	0.807
180	1.887	0.272	0.152	0.813
180	1.886	0.272	0.152	0.821

Table 5-13. Corrected non-dimensional results
for test configuration #1-1.

ANGLE OF ROTATION (DEGREE)	TEST MACH NUMBER	MACH NUMBER AFTER BOW SHOCK	PROBE PRESSURE RATIO	EXTERNAL PRESSURE RATIO	INTERNAL PRESSURE RATIO
0	1.886	1.3	0.361	0.152	0.84
0	1.887	1.328	0.347	0.152	0.83
0	1.883	1.346	0.339	0.153	0.83
45	1.886	1.403	0.313	0.152	0.83
45	1.886	1.397	0.316	0.153	0.83
45	1.884	1.401	0.314	0.153	0.83
90	1.882	1.375	0.325	0.153	0.83
90	1.882	1.371	0.327	0.153	0.84
90	1.879	1.369	0.328	0.154	0.83
135	1.885	1.31	0.356	0.153	0.83
135	1.878	1.314	0.354	0.154	0.83
135	1.879	1.325	0.349	0.154	0.84
180	1.873	1.278	0.372	0.156	0.83
180	1.87	1.279	0.371	0.156	0.83
180	1.877	1.278	0.372	0.155	0.83

Table 5-14. Corrected non-dimensional results
for test configuration #1-2.

ANGLE OF ROTATION (DEGREE)	TEST MACH NUMBER	MACH NUMBER AFTER BOW SHOCK	PROBE PRESSURE RATIO	EXTERNAL PRESSURE RATIO	INTERNAL PRESSURE RATIO
0	1.893	1.5	0.272	0.151	0.82
0	1.886	1.506	0.27	0.152	0.81
0	1.884	1.498	0.273	0.153	0.82
45	1.896	1.563	0.249	0.15	0.82
45	1.889	1.548	0.254	0.152	0.82
45	1.889	1.547	0.254	0.152	0.82
90	1.894	1.497	0.274	0.151	0.82
90	1.889	1.489	0.277	0.152	0.83
90	1.888	1.483	0.279	0.152	0.82
135	1.889	1.389	0.319	0.152	0.83
135	1.888	1.384	0.322	0.152	0.82
135	1.885	1.38	0.323	0.153	0.82
180	1.889	1.362	0.332	0.152	0.82
180	1.887	1.36	0.332	0.152	0.82
180	1.888	1.361	0.332	0.152	0.82

Table 5-15. Corrected non-dimensional results
for test configuration #1-3.

ANGLE OF ROTATION (DEGREE)	TEST MACH NUMBER	MACH NUMBER AFTER BOW SHOCK	PROBE PRESSURE RATIO	EXTERNAL PRESSURE RATIO	INTERNAL PRESSURE RATIO
0	1.886	1.582	0.241	0.153	0.81
0	1.888	1.586	0.24	0.152	0.85
0	1.887	1.573	0.245	0.152	0.88
45	1.904	1.668	0.213	0.148	0.85
45	1.9	1.668	0.213	0.149	0.84
45	1.896	1.653	0.217	0.15	0.89
90	1.9	1.594	0.237	0.149	0.85
90	1.902	1.573	0.245	0.148	0.85
90	1.896	1.604	0.234	0.15	0.89
135	1.899	1.453	0.291	0.149	0.84
135	1.898	1.453	0.292	0.149	0.84
135	1.899	1.446	0.294	0.149	0.86
180	1.884	1.43	0.301	0.153	0.84
180	1.88	1.435	0.299	0.154	0.83
180	1.881	1.456	0.29	0.154	0.85

Table 5-16. Corrected non-dimensional results
for test configuration #2-1.

ANGLE OF ROTATION (DEGREE)	TEST MACH NUMBER	MACH NUMBER AFTER BOW SHOCK	PROBE PRESSURE RATIO	EXTERNAL PRESSURE RATIO	INTERNAL PRESSURE RATIO
0	1.889	1.538	0.258	0.152	0.83
0	1.889	1.538	0.258	0.152	0.83
0	1.888	1.544	0.256	0.152	0.82
45	1.885	1.62	0.228	0.153	0.84
45	1.887	1.625	0.227	0.152	0.84
45	1.887	1.625	0.227	0.152	0.84
90	1.89	1.625	0.227	0.152	0.85
90	1.886	1.629	0.225	0.153	0.82
90	1.883	1.611	0.231	0.153	0.83
135	1.885	1.583	0.241	0.153	0.82
135	1.886	1.582	0.242	0.153	0.83
135	1.882	1.581	0.242	0.154	0.83
180	1.89	1.523	0.263	0.152	0.83
180	1.886	1.524	0.263	0.152	0.82
180	1.889	1.524	0.263	0.152	0.82

Table 5-17. Corrected non-dimensional results
for test configuration #2-2.

ANGLE OF ROTATION (DEGREE)	TEST MACH NUMBER	MACH NUMBER AFTER BOW SHOCK	PROBE PRESSURE RATIO	EXTERNAL PRESSURE RATIO	INTERNAL PRESSURE RATIO
0	1.883	1.463	0.287	0.153	0.82
0	1.883	1.463	0.287	0.153	0.82
0	1.875	1.466	0.286	0.155	0.82
45	1.879	1.562	0.249	0.154	0.82
45	1.877	1.545	0.255	0.155	0.84
45	1.871	1.537	0.258	0.156	0.82
90	1.883	1.599	0.236	0.153	0.83
90	1.882	1.617	0.229	0.154	0.82
90	1.872	1.626	0.226	0.156	0.83
135	1.878	1.589	0.239	0.154	0.84
135	1.875	1.591	0.238	0.155	0.83
135	1.87	1.586	0.24	0.156	0.84
180	1.877	1.524	0.263	0.155	0.83
180	1.876	1.521	0.264	0.155	0.82
180	1.87	1.517	0.266	0.156	0.82

Table 5-18. Corrected non-dimensional results
for test configuration #2-3.

ANGLE OF ROTATION (DEGREE)	TEST MACH NUMBER	MACH NUMBER AFTER BOW SHOCK	PROBE PRESSURE RATIO	EXTERNAL PRESSURE RATIO	INTERNAL PRESSURE RATIO
0	1.898	1.379	0.324	0.15	0.83
0	1.9	1.424	0.304	0.149	0.79
0	1.895	1.421	0.305	0.15	0.83
45	1.9	1.473	0.283	0.149	0.82
45	1.901	1.473	0.283	0.149	0.83
45	1.899	1.474	0.283	0.149	0.83
90	1.899	1.419	0.306	0.149	0.82
90	1.895	1.422	0.305	0.15	0.82
90	1.896	1.533	0.26	0.15	0.81
135	1.896	1.537	0.258	0.15	0.83
135	1.894	1.54	0.257	0.151	0.82
135	1.89	1.549	0.254	0.152	0.82
180	1.888	1.576	0.244	0.152	0.81
180	1.887	1.569	0.246	0.152	0.81
180	1.886	1.569	0.246	0.152	0.82

Table 5-19. Corrected average non-dimensional results for test configuration #1-1.

LE OF ROTATION (DEGREE)	AVERAGE TEST MACH NUMBER	STANDARD DEVIATION	AVERAGE MACH NUMBER AFTER BOW SHOCK	STANDARD DEVIATION	AVERAGE PROBE PRESSURE RATIO	STANDARD DEVIATION	AVERAGE EXTERNAL PRESSURE RATIO	STANDARD DEVIATION	AVERAGE INTERNAL PRESSURE RATIO	STANDARD DEVIATION
0	1.885	0.0016	1.324	0.0837	0.3494	0.0221	0.1526	0.0398	0.8343	0.0412
45	1.885	0.0009	1.401	0.0577	0.314	0.0129	0.1527	0.0411	0.8316	0.0416
90	1.881	0.0013	1.372	0.0486	0.3268	0.0116	0.1537	0.0406	0.8332	0.0445
135	1.881	0.0029	1.316	0.0572	0.3531	0.0154	0.1538	0.0413	0.8335	0.0427
180	1.873	0.0024	1.278	0.0547	0.3716	0.0159	0.1555	0.0431	0.8322	0.0407

Table 5-20. Corrected average non-dimensional results for test configuration #1-2

ANGLE OF ROTATION (DEGREE)	AVERAGE TEST MACH NUMBER	STANDARD DEVIATION	AVERAGE MACH NUMBER AFTER BOW SHOCK	STANDARD DEVIATION	AVERAGE PROBE PRESSURE RATIO	STANDARD DEVIATION	AVERAGE EXTERNAL PRESSURE RATIO	STANDARD DEVIATION	AVERAGE INTERNAL PRESSURE RATIO	STANDARD DEVIATION
0	1.888	0.0036	1.502	0.0591	0.2718	0.0107	0.1521	0.0378	0.8165	0.0457
45	1.891	0.0031	1.553	0.0587	0.2522	0.0095	0.1512	0.0423	0.8204	0.0472
90	1.89	0.0024	1.49	0.0619	0.2765	0.0115	0.1515	0.0419	0.8233	0.0453
135	1.887	0.0016	1.384	0.0585	0.3213	0.0136	0.1522	0.0407	0.8221	0.0394
180	1.888	0.0007	1.361	0.0569	0.3318	0.0139	0.152	0.0435	0.8206	0.0442

Table 5-21. Corrected average non-dimensional results for test configuration #1-3.

ANGLE OF ROTATION (DEGREE)	AVERAGE TEST MACH NUMBER	STANDARD DEVIATION	AVERAGE MACH NUMBER AFTER BOW SHOCK	STANDARD DEVIATION	AVERAGE PROBE PRESSURE RATIO	STANDARD DEVIATION	AVERAGE EXTERNAL PRESSURE RATIO	STANDARD DEVIATION	AVERAGE INTERNAL PRESSURE RATIO	STANDARD DEVIATION
0	1.887	0.0007	1.58	0.0862	0.2422	0.0132	0.1523	0.0613	0.847	0.0632
45	1.9	0.0027	1.663	0.0736	0.2141	0.0095	0.1489	0.1016	0.8569	0.0969
90	1.899	0.0022	1.59	0.0847	0.2387	0.0127	0.149	0.0881	0.8614	0.0804
135	1.899	0.0004	1.451	0.0656	0.2924	0.0132	0.1492	0.0499	0.8459	0.0499
180	1.882	0.0016	1.44	0.0728	0.2969	0.015	0.1535	0.0405	0.84	0.0483

Table 5-22. Corrected average non-dimensional results for test configuration #2-1.

ANGLE OF ROTATION (DEGREE)	AVERAGE TEST MACH NUMBER	STANDARD DEVIATION	AVERAGE MACH NUMBER AFTER BOW SHOCK	STANDARD DEVIATION	AVERAGE PROBE PRESSURE RATIO	STANDARD DEVIATION	AVERAGE EXTERNAL PRESSURE RATIO	STANDARD DEVIATION	AVERAGE INTERNAL PRESSURE RATIO	STANDARD DEVIATION
0	1.889	0.0004	1.54	0.0475	0.2572	0.0079	0.1519	0.0279	0.8276	0.0268
45	1.886	0.0009	1.623	0.058	0.2274	0.0081	0.1524	0.0265	0.8358	0.0284
90	1.886	0.0024	1.622	0.0682	0.2279	0.0096	0.1524	0.038	0.834	0.0345
135	1.884	0.0016	1.582	0.0669	0.2416	0.0102	0.1529	0.0421	0.8286	0.0437
180	1.888	0.0016	1.524	0.0663	0.2632	0.0115	0.1519	0.0445	0.8245	0.0394

Table 5-23. Corrected average non-dimensional results for test configuration #2-2.

ANGLE OF ROTATION (DEGREE)	AVERAGE TEST MACH NUMBER	STANDARD DEVIATION	AVERAGE MACH NUMBER AFTER BOW SHOCK	STANDARD DEVIATION	AVERAGE PROBE PRESSURE RATIO	STANDARD DEVIATION	AVERAGE EXTERNAL PRESSURE RATIO	STANDARD DEVIATION	AVERAGE INTERNAL PRESSURE RATIO	STANDARD DEVIATION
0	1.88	0.0036	1.464	0.0406	0.2868	0.008	0.1539	0.0245	0.8174	0.0307
45	1.876	0.0031	1.549	0.0557	0.2538	0.0091	0.155	0.0409	0.8285	0.0547
90	1.879	0.0047	1.614	0.0748	0.2305	0.0107	0.1542	0.0414	0.8302	0.0468
135	1.874	0.0029	1.589	0.0743	0.2392	0.0112	0.1552	0.0403	0.8358	0.0463
180	1.874	0.0029	1.521	0.0715	0.2644	0.0124	0.1552	0.0413	0.8245	0.0439

Table 5-24. Corrected average non-dimensional results for test configuration #2-3.

ANGLE OF ROTATION (DEGREE)	AVERAGE TEST MACH NUMBER	STANDARD DEVIATION	AVERAGE MACH NUMBER AFTER BOW SHOCK	STANDARD DEVIATION	AVERAGE PROBE PRESSURE RATIO	STANDARD DEVIATION	AVERAGE EXTERNAL PRESSURE RATIO	STANDARD DEVIATION	AVERAGE INTERNAL PRESSURE RATIO	STANDARD DEVIATION
0	1.898	0.0018	1.407	0.0945	0.311	0.0209	0.1498	0.0408	0.8167	0.0541
45	1.9	0.0007	1.474	0.0569	0.283	0.0109	0.1493	0.043	0.8255	0.0467
90	1.897	0.0016	1.455	0.1398	0.2906	0.0279	0.15	0.0408	0.8161	0.0391
135	1.893	0.0022	1.542	0.0726	0.2563	0.0121	0.1508	0.0424	0.8232	0.0412
180	1.887	0.0007	1.571	0.0615	0.2454	0.0096	0.1523	0.0443	0.8135	0.0455

Table 5-25. Redefined total pressure recovery ratio and coefficient of spillage drag for test configuration #1-1.

External Mach Number	Internal Mach Number	Redefined Total Pressure Recovery Ratio	Standard Deviation	Coefficient of Spillage Drag: A	Coefficient of Spillage Drag: B	Fractional Standard Deviation
1.885	0.5154	0.1829	0.05674	0.6698	0.4020	0.310
1.885	0.5201	0.1836	0.05861	0.6597	0.4020	0.319
1.881	0.5173	0.1845	0.05858	0.6668	0.4038	0.317
1.881	0.5168	0.1845	0.05900	0.6674	0.4038	0.319
1.873	0.5191	0.1868	0.06093	0.6670	0.4072	0.326

Table 5-26. Redefined total pressure recovery ratio and coefficient of spillage drag for test configuration #1-2.

External Mach Number	Internal Mach Number	Redefined Total Pressure Recovery Ratio	Standard Deviation	Coefficient of Spillage Drag: A	Coefficient of Spillage Drag: B	Fractional Standard Deviation
1.888	0.5460	0.1862	0.05672	0.6072	0.4008	0.304
1.891	0.5394	0.1843	0.06216	0.6193	0.3995	0.337
1.890	0.5344	0.1840	0.06102	0.6291	0.3999	0.331
1.887	0.5365	0.1851	0.05838	0.6264	0.4012	0.315
1.888	0.5390	0.1852	0.06299	0.6209	0.4008	0.340

* Note:

$$C_{\text{spillage drag}} = A \frac{P_{o2}}{P_{o1}} - B$$

Table 5-27. Redefined total pressure recovery ratio and coefficient of spillage drag for test configuration #1-3.

External Mach Number	Internal Mach Number	Redefined Total Pressure Recovery Ratio	Standard Deviation	Coefficient of Spillage Drag: A	Coefficient of Spillage Drag: B	Fractional Standard Deviation
1.887	0.4929	0.1798	0.08579	0.7164	0.4012	0.477
1.900	0.4749	0.1738	0.13822	0.7552	0.3957	0.795
1.899	0.4666	0.1730	0.11842	0.7761	0.3961	0.685
1.899	0.4949	0.1764	0.06940	0.7092	0.3961	0.393
1.882	0.5054	0.1827	0.05872	0.6911	0.4033	0.321

Table 5-28. Redefined total pressure recovery ratio and coefficient of spillage drag for test configuration #2-1.

External Mach Number	Internal Mach Number	Redefined Total Pressure Recovery Ratio	Standard Deviation	Coefficient of Spillage Drag: A	Coefficient of Spillage Drag: B	Fractional Standard Deviation
1.889	0.5270	0.1835	0.03966	0.6434	0.4003	0.339
1.886	0.5127	0.1823	0.03790	0.6747	0.4016	0.344
1.886	0.5159	0.1827	0.05312	0.6681	0.4016	0.320
1.884	0.5253	0.1845	0.06054	0.6497	0.4025	0.331
1.888	0.5323	0.1842	0.06278	0.6342	0.4008	0.347

* Note:

$$C_{\text{spillage drag}} = A \frac{P_{o2}}{P_{o1}} - B$$

Table 5-29. Redefined total pressure recovery ratio and coefficient of spillage drag for test configuration #2-2.

External Mach Number	Internal Mach Number	Redefined Total Pressure Recovery Ratio	Standard Deviation	Coefficient of Spillage Drag: A	Coefficient of Spillage Drag: B	Fractional Standard Deviation
1.880	0.5445	0.1883	0.03704	0.6141	0.4042	0.197
1.876	0.5255	0.1871	0.06172	0.6520	0.4059	0.330
1.879	0.5225	0.1857	0.06034	0.6569	0.4046	0.325
1.874	0.5127	0.1857	0.05850	0.6797	0.4068	0.315
1.874	0.5324	0.1882	0.06011	0.6405	0.4068	0.319

Table 5-30. Redefined total pressure recovery ratio and coefficient of spillage drag for test configuration #2-3.

External Mach Number	Internal Mach Number	Redefined Total Pressure Recovery Ratio	Standard Deviation	Coefficient of Spillage Drag: A	Coefficient of Spillage Drag: B	Fractional Standard Deviation
1.898	0.5457	0.1834	0.06211	0.6031	0.3966	0.339
1.900	0.5307	0.1809	0.06232	0.6317	0.3957	0.345
1.897	0.5467	0.1838	0.05880	0.6018	0.3970	0.320
1.893	0.5346	0.1832	0.06067	0.6274	0.3987	0.331
1.887	0.5511	0.1872	0.06493	0.5984	0.4012	0.347

* Note:

$$C_{\text{spillage drag}} = A \frac{P_{o2}}{P_{o1}} - B$$

Chapter 6

DISCUSSION OF RESULTS

The details of the experimental results are presented in this chapter. First, the effects of the deflector length variation on the flow field are discussed. Then, the effects of the deflector base width variation are examined.

6-1. The Effect of Deflector Length

As illustrated in Fig 6-1, the external probe pressure measurements at different angles of rotation reveal a considerable pressure ratio variation around the inlet deflector. It is noted that the pressure ratio decreases as the angle of rotation increases. Further decrease in the external pressure ratio is observed until the 45° rotation of the test configuration. At the 45° rotation, the deflector and the cowl lip of an inlet merge together. The lowest pressure ratio at the junction is mainly due to a weak oblique shock generated in the vicinity of the deflector and the spillage of air which is blocked by the deflector through the junction. The formation of the oblique shock at the entrance of the inlet reduces the incoming flow velocity gradually. As the angle of rotation

progressively increases, the probe pressure ratio increases modestly. By comparing the measurements at 0° and 180° rotations, a lower pressure ratio is observed at 0° rotation. This is because, although there is an oblique shock generated in the vicinity of the deflector, the supersonic flow condition in the outer region of the deflector is maintained along the deflector length. The higher pressure ratio at 180° rotation is due to the presence of a subsonic region at the entrance of the inlet.

Also, Fig. 6-1. demonstrates that the overall external probe pressure ratio decreases further as the length of the deflector is increased. This trend is contributed to by two factors. First, as the length of the deflector increases, a smaller deflector's side angle is formed which consequently results in a smaller oblique shock angle formation. In addition, as the length of the deflector increases, a greater portion of the incoming flow is gradually slowed down by an oblique shock generated further away from the inlet entrance. This indicates that a significant portion of the flow retains its relatively low pressure ratio. Although these two factors contribute much to lower the external probe pressure measurements, as the length of the deflector is increased further, the magnitude of these effects declines. Consequently, the rate of decrease in the external probe measurement declines.

The results of the internal pressure ratio measurements at different deflector lengths are illustrated in Fig. 6-2. The results indicate that as the length of the deflector increases, a decrease in the internal pressure ratio is

obtained. This is because a significant amount of the incoming flow is gradually slowed down by the oblique shock wave. There is a decrease in the internal pressure ratio. However, the overall quantitative improvements on the internal pressure ratio is found to be small. Also, as shadowgraph photos display, although there is an impinging oblique shock onto the normal shock, the results indicate that the overall quality of the internal flow is maintained. The results show the steadiness in the pressure ratio measurements for each rotation. The steadiness in the internal pressure ratio implies that the magnitude of the impinging oblique shock is weak to disturb the internal flow.

The results of the Redefined Total Pressure Recovery Ratio (RTPRR) measurements at different deflector lengths are presented in Fig 6-3. As mentioned in Chap. 5, the variables are redefined due to the non-dimensionalization of the pressure terms. The experimental RTPRR of the test configurations and the theoretical RTPRR of a simple pitot tube are plotted against the Mach number. The experimental results indicate that RTPRR improves as the length of the deflector increases. This coincides with the overall improvements of the internal pressure ratio. However, the results for Test Configuration #1-3 display the deterioration in RTPRR. Since the experimental results (Test Configuration #1-3) reveal much scatter in data, this peculiar behavior is assumed due to errors in the tunnel operation.

The results indicate that the experimental RTPRR are measured lower than the theoretical RTPRR for a simple pitot tube. This is because the

theoretical data is calculated based on the assumption of an inviscid and isentropic flow; whereas the experimental results are obtained for the actual flow where much of the internal pressure is lost due to the friction. Although RTPRR improves as the length of the deflector increases, the results fail to quantify the improvement on each test configuration due to its high uncertainty in measurements.

Figure 6-4 shows the coefficient of spillage drag at various deflector lengths. The experimental data is plotted against the total pressure recovery ratio. The results indicate that the coefficient of drag decreases as the length of the deflector increases. This is because as the length of the deflector increases, a significant portion of the incoming flow velocity is reduced by the oblique shock generated in the vicinity of the deflector. Like RTPRR, the quantitative improvements in the coefficient of spillage drag for different different lengths are not calculated due to its high uncertainty in measurements.

For the shock angle and the shock standoff distance measurements, the shadowgraph photos are presented in Appendix A for the visual comparisons. The photographs, A-1, A-2, and A-3, represent the shock waves formation at each angle of rotation for each test configuration. The results show that as the length of the deflector increases, a smaller spillage shock angle is observed. This result is clearly seen at 180° rotation. The smaller shock angle results because a larger portion of the incoming flow is slowed down by an oblique

shock where the flow retains its relatively low pressure ratio. These conclusions are further reinforced by the results obtained from the external probe pressure measurements. As previously stated, the external probe measurements indicate that as the length of the deflector is increased, a decrease in the pressure ratio is observed. Since the shadowgraph photos display a decrease in the shock angle, which represents a decrease in the magnitude of the shock disturbances, a lower external pressure ratio behind the shock is expected. The photographs show that there is a small decrease in the shock standoff distance as the deflector length increases. This is expected since there is a decrease in the coefficient of spillage drag. However, due to negligible variations in the shock standoff distance, and poor photograph resolution, the quantitative measurements of each test configuration are not included.

6-2. The Effects of Deflector Base Width

The experimental results indicate that at different angles of rotation, the external probe pressure measurements around the inlet, at various deflector base widths, reveal variations in the pressure ratio (Fig. 6-5). Like the results presented in Section 6-1, Fig. 6-5 shows the lowest pressure ratio at the junction where the deflector and the inlet cowl lip merge together. In addition, the results show that as the deflector base width increases, the position of the lowest probe pressure ratio shifts closer to the junction. Also, it is noted that

as the angle of rotation increases further from the junction, the pressure ratio increases modestly. Conclusively, the basic pattern in the pressure distribution around the inlet at different base widths is similar to the results at different deflector lengths.

As illustrated in Fig. 6-5, when the base width of the deflector increases, further increase in the external probe pressure ratio measurements at 0° rotation is found. This is because as the base width of the deflector increases, a stronger oblique shock is formed due to increase in the deflector's side angle. Consequently, the shock formation contributes in a higher external probe pressure ratio at 0° rotation. However, the external pressure measurements at 180° rotation reveal the opposite trend compared to the results at 0° rotation. The external probe pressure measurements at 180° rotation continuously decrease as the deflector base width increases. This is because as the base width of the deflector increases, a significant amount of air spills through the reduced area which results further decrease in the probe pressure ratio measurements. As the base width of the deflector increases, the area for air spillage decreases. Consequently, as the base width of the deflector increases further, the probe measurements display lower pressure ratios at 180° rotation.

The results of the internal pressure ratio measurements at different base widths are presented in Fig 6-6. The results show that as the base width increases, a modest decrease in the internal pressure measurements is

observed. This is because as the base width increases, a broader area of the inlet is covered by the oblique shock. Also, the results display a modest fluctuation in data at different angles of rotation: however, in general, the quality of data displays the uniformity in the internal flow.

Figure 6-7 show the Redefined Total Pressure Recovery Ratio (RTPRR) at different deflector base widths. The experimental RTPRR of the Test Configurations and the theoretical RTPRR of a simple pitot tube are plotted as function of the test Mach number. The results indicate that RTPRR improves as the base width of the deflector increases. The improvement in RTPRR results because the broader area of the inlet is within the range of an oblique shock generated in the vicinity of the deflector. In addition, it is noted that the experimental RTPRR are lower than the theoretical RTPRR. This is because, as mentioned previously, much of the internal pressure is lost due to friction. Due to high uncertainty in measurements and a small increase in ratio, the results fail to quantify the improvement on each test configuration.

The coefficient of spillage drag at various deflector widths is shown in Fig 6-8. The drag coefficients are plotted against the total pressure recovery ratio. Although much of the data are scattered, the results clearly indicate that the coefficient of the drag decreases as the base width of the deflector increases. However, similar to RTPRR, the quantitative improvements in the coefficient of spillage drag at each base width are not calculated due to its high uncertainty in measurements and its minimal changes.

The shadowgraph photos presented in Appendices A-4, A-5, and A-6, indicate that as the base width of the deflector increases, the shock angle at 0° rotation increases where the external probes measured an increase in the external pressure ratio. Accordingly, as the base width of the deflector increases, the shock angle at 180° rotation decreases where the external probes measured a decrease in the external pressure ratio. Since, in theory, the shock angle variation is expected to directly relate with the external pressure variation, the trend in the shock angle measurements is identical with the trend in the external probe pressure measurements. Also, the photographs demonstrate that the shock standoff distance increases as the base width increases. This is because when the base width increases, the exit area for the air spillage is reduced. Hence, to compensate the loss in exit area, the normal shock moves forward, therefore a small increase in the shock standoff distance is observed. In the experiments, the quantitative measurements of the shock standoff distance are not achieved due to high uncertainties in its measurements.

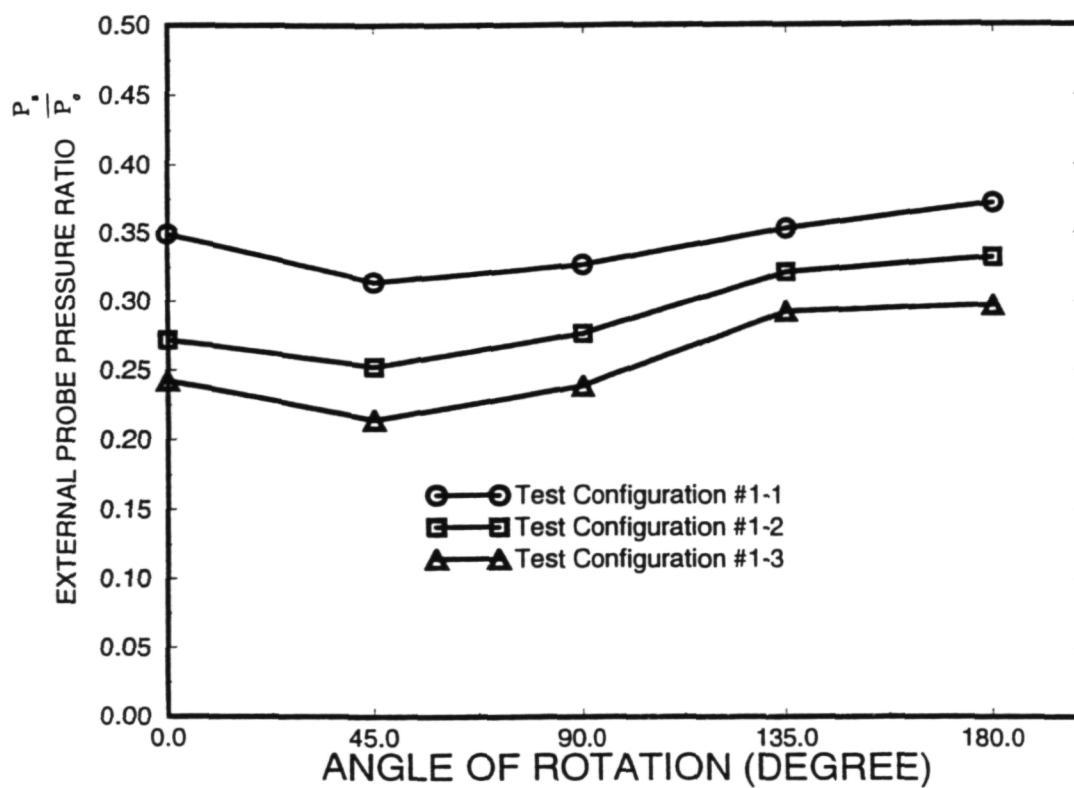


Figure 6-1. External probe pressure ratio measurements for different deflector lengths.

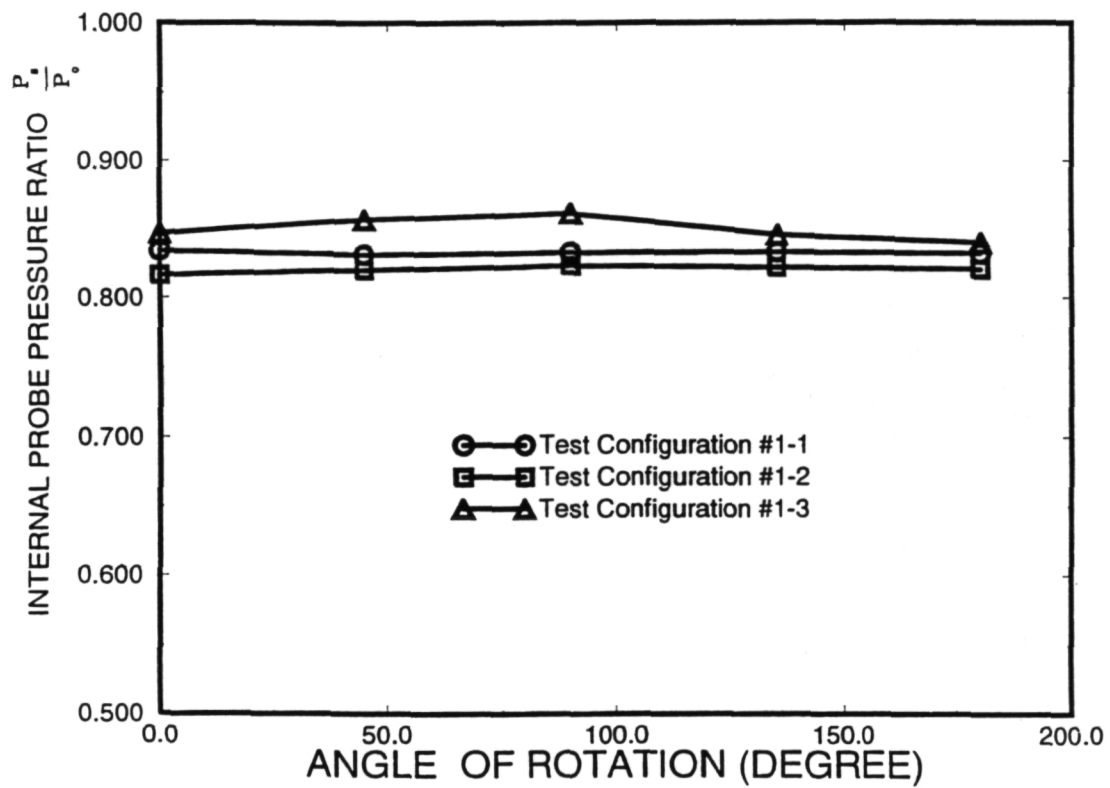


Figure 6-2. Internal probe pressure ratio measurements for different deflector lengths.

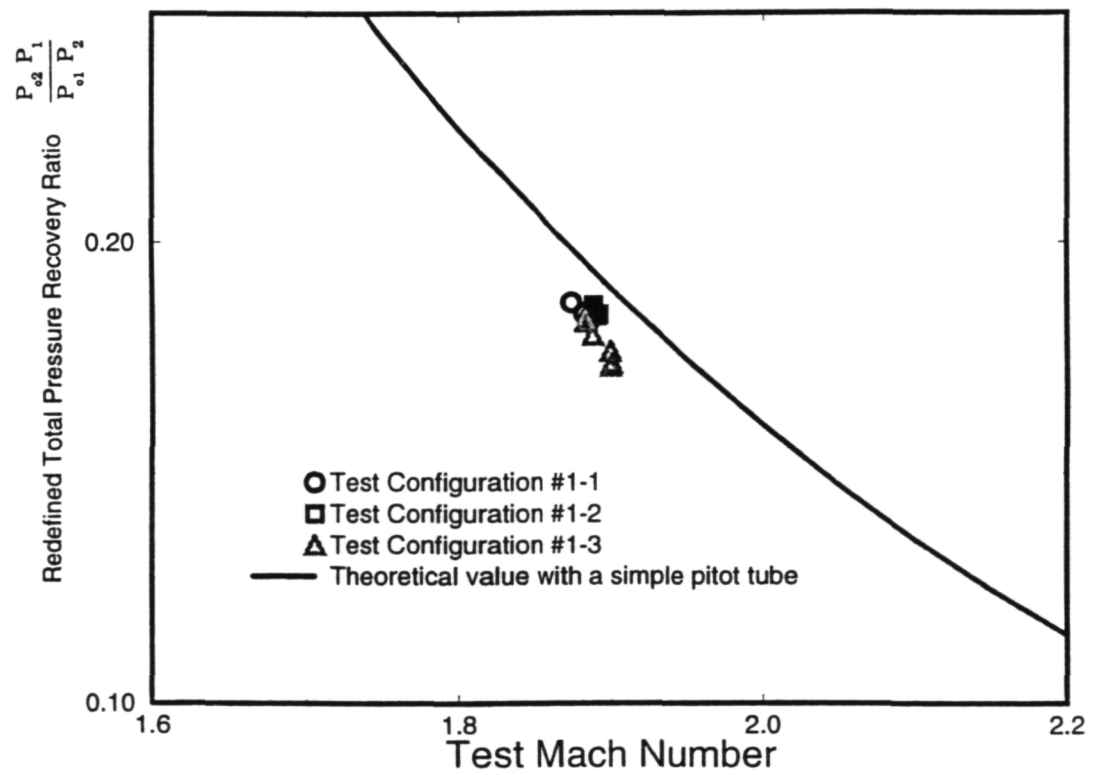


Figure 6-3. Redefined Total Pressure Recovery Ratio (RTPRR) for different deflector lengths and a theoretical simple pitot tube.

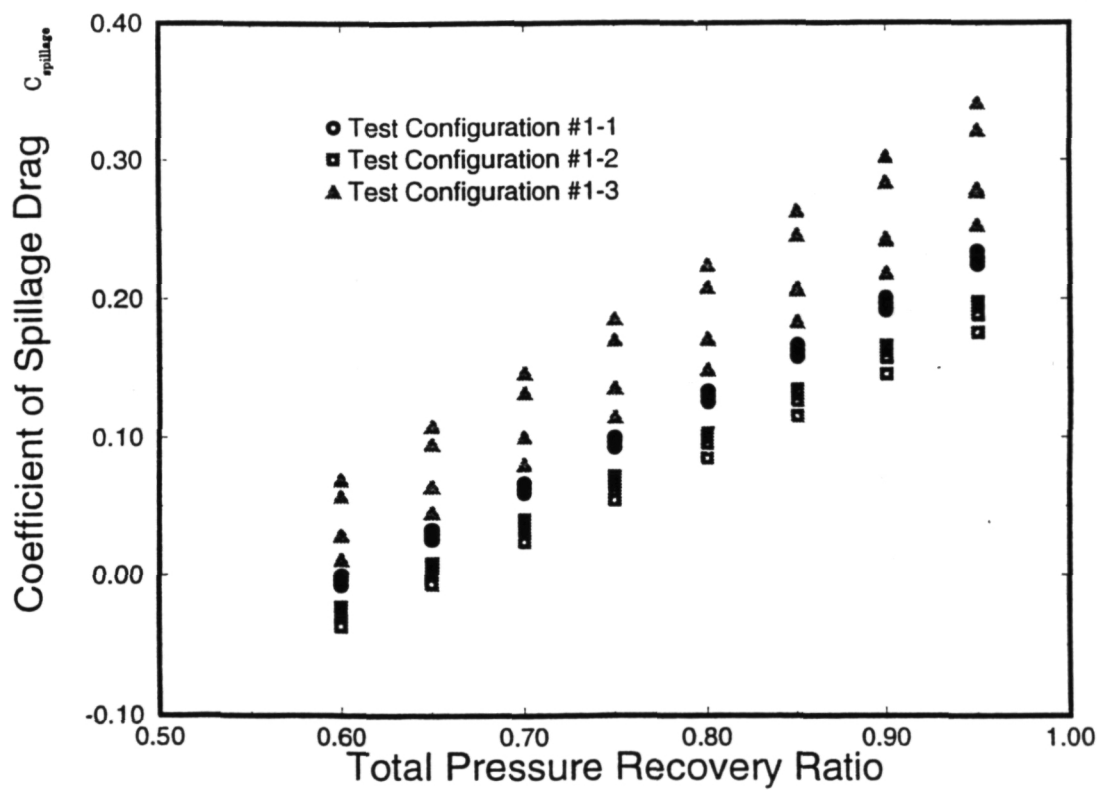


Figure 6-4. Coefficient of spillage drag vs. total pressure recovery ratio for different deflector lengths.

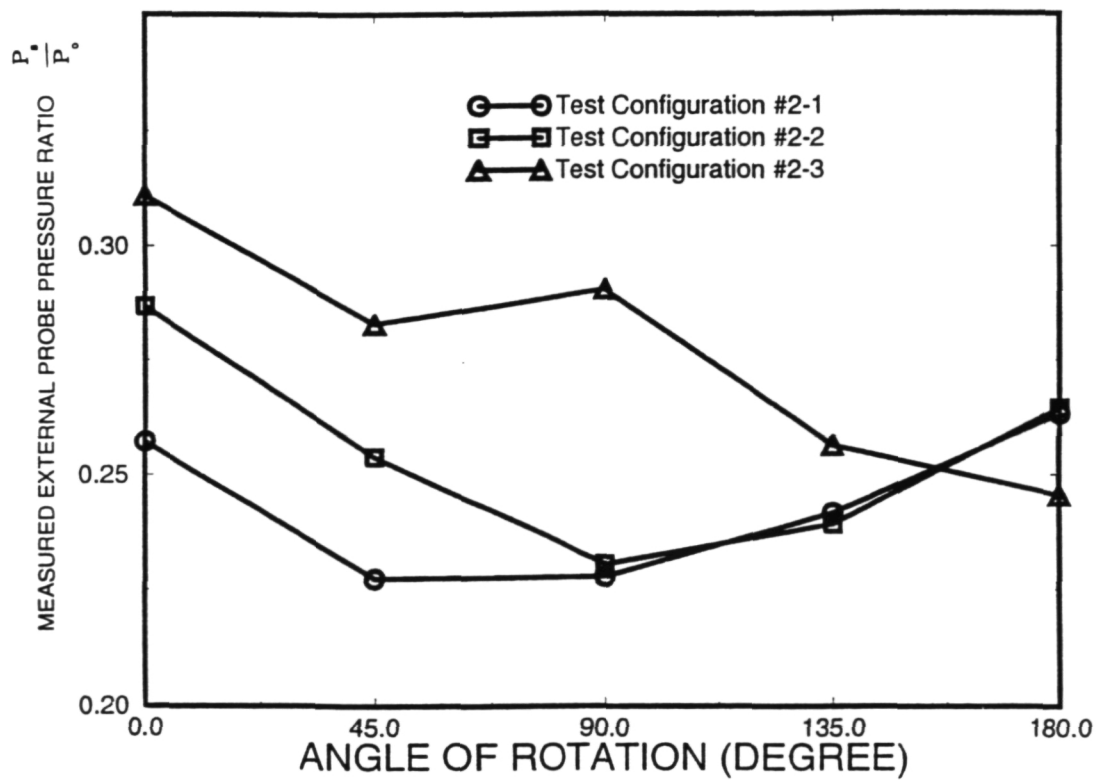


Figure 6-5. External probe pressure ratio measurements for different base widths.

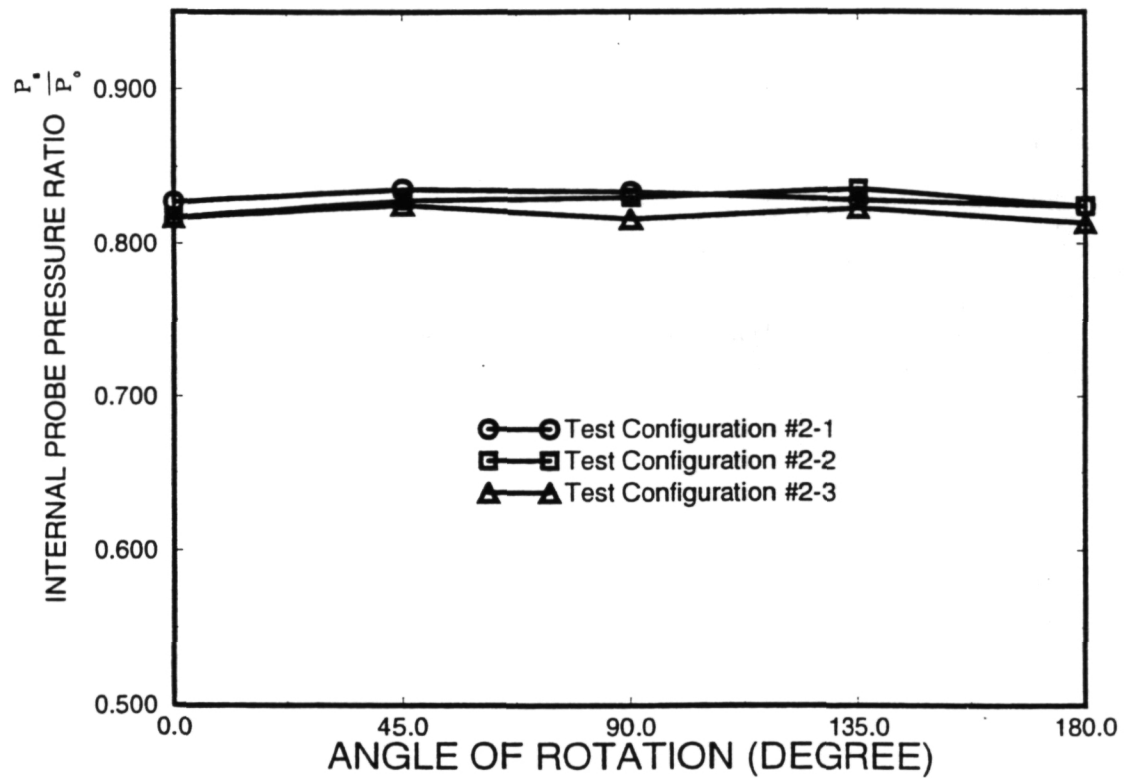


Figure 6-6. Internal probe pressure ratio measurements for different base widths.

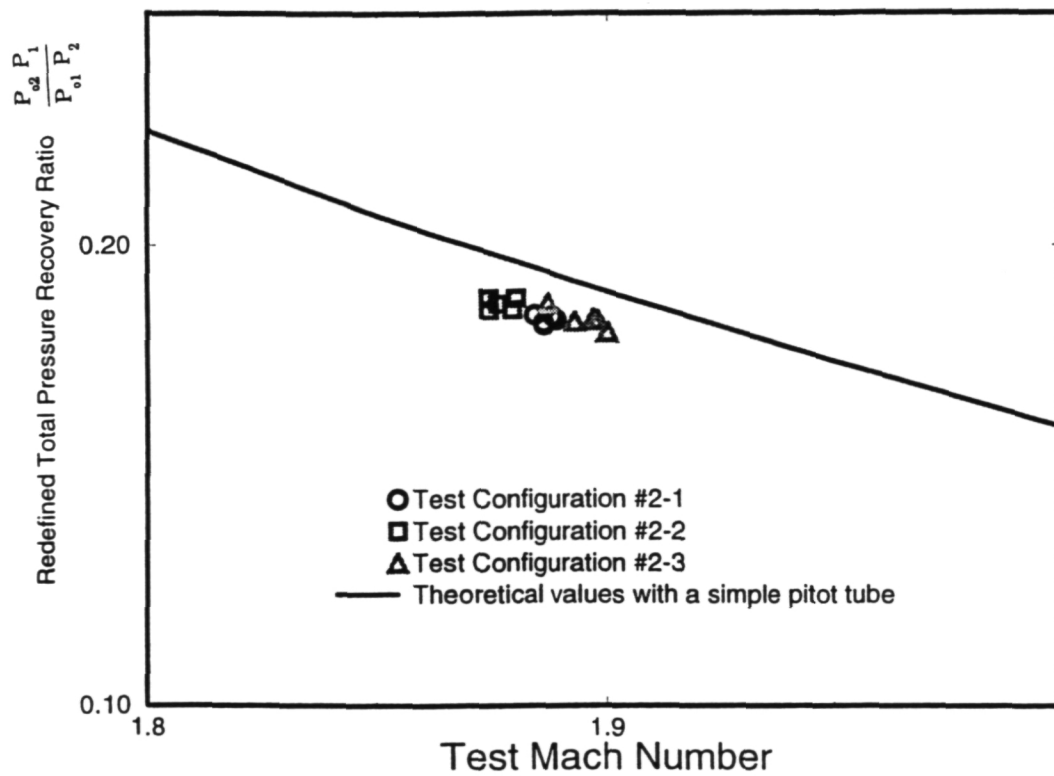


Figure 6-7. Redefined Total Pressure Recovery Ratio (RTPRR) for different base width lengths and a theoretical simple pitot tube.

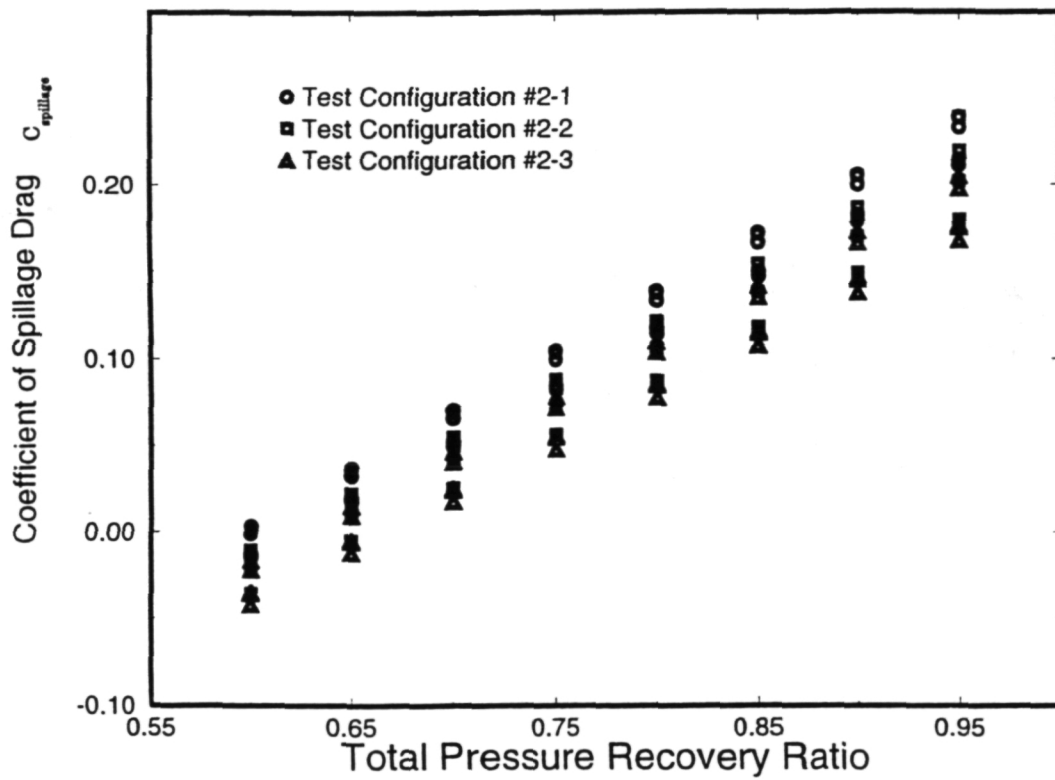


Figure 6-8. Coefficient of spillage drag vs. total pressure recovery ratio for different base widths.

Chapter 7

CONCLUSIONS

In this study, the effects of the variation in deflector configuration on the flow field are investigated. The study is initiated to investigate the possibility/feasibility of modifying the F-16 inlet to minimize shock disturbances on the wing where the data acquisition is conducted. For this study, the F-16 inlet is simulated by a simple circular tube with various triangular deflector configurations. The experiments are conducted at Mach 1.9. The internal Reynolds number is between 1.12×10^3 and 1.35×10^3 and the internal mass flow rate is 83 percent of the incoming mass flow.

In the study of the effects of deflector length on the flow field, the lowest external pressure ratio is observed at the junction of deflector lip and the inlet cowl lip. By comparing the probe pressure measurements at 0° and 180° rotation, lower pressure ratio is observed at 0° . In these experiments, it is inferred that an increase in the deflector length leads to a decrease in the external probe pressure ratio and the bow shock angle formation around the inlet-deflector. In addition, the internal pressure ratio, the coefficient of spillage drag, and the shock standoff distance decrease with an increase in the

deflector length. Consequently, RTPRR increases with an increase in the length of the deflector.

In the study of the effects of the deflector base width on the flow field, the lowest external probe pressure ratio is observed at the junction of the inlet cowl lip and the deflector lip. The results show that as the base width of the deflector increases, the position of the lowest probe pressure ratio shifts closer to the junction. By comparing the external probe pressure ratio at 0° and 180° rotations, the probe pressure ratio measurements at 0° rotation increase with an increase in the deflector base width. However, the external probe pressure ratio at 180° rotation decreases as the deflector base width increases. These results are further strengthened by the results obtained from the shadowgraph photos. The photographs display a decrease in the shock angle at 0° of rotation and an increase in the shock angle at 180° as the deflector base width increases. Also, it is noted that with an increase in the base width, the internal pressure ratio and the coefficient of spillage drag decreases further. In consequence, RTPRR and the shock standoff distance increase.

In conclusion, the experimental results indicate that there is significant pressure variation around the inlet deflector for various deflector configurations. As deflector dimensions vary, distinctive patterns in the pressure variations around the inlet-deflector are observed. With an increase in the deflector length and base width, the magnitude of shock-disturbances are weaker due to decrease in the external pressure ratio. Also, the

shadowgraph photos infer that as the deflector length and the base width increase, a smaller bow shock angle is formed. These indicate that the inlet shock wave formation around the inlet-deflector can be significantly altered by modifying the deflector. Consequently, shock-disturbances on the wing could be avoided through appropriately designing the deflector.

REFERENCES

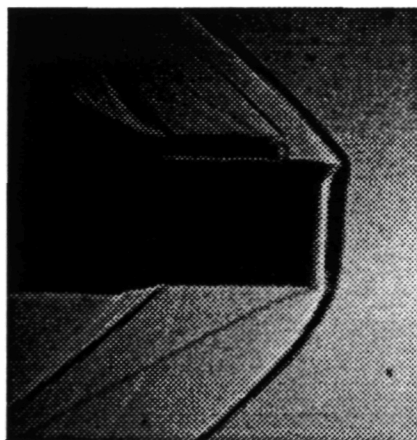
1. Fischer, M. C., "Application of Laminar Flow Control to the High Speed Civil Transport-the NASA Supersonic Laminar Flow Control Program", SAE Paper No. 912115, September 1991.
2. Fischer, M. C., and Miley S., "Shock-Disturbances and the F-16XL Inlet", Private Communication, 1994.
3. Seddon, J., Goldsmith, E. L., and Carbonaro, M., "Intake Aerodynamics", Lecture Series 1988-04, Vol. 1, Von Karman Institute for Fluid Dynamics, Chausse De Waterloo, 72, B-1640, Rhode Saint Gnese, Belgium, February 1988.
4. Ferri, A., and Nucci, L. M., "Theoretical and Experimental Analysis of Low Drag Supersonic Inlets having a Circular Cross Section and a Central Body at Mach Numbers of 3.30, 2.75, 2.45", NACA Report No. 1189, May 1948.
5. Flores, J., Chaderjian, N., and Sorenson, R., "Simulation of Transonic Viscous Flow over a Fighter-Like Configuration Including Inlet", Journal of Aircraft, Vol. 26, No. 4, 1989, pp. 295-301.
6. Huband, G., Rizzetta, D., and Shang, J., "Numerical Simulation of the Navier-Stokes Equations for an F-16A Configuration", Journal of Aircraft, Vol. 26, No. 7, 1989, pp. 634-640.
7. Fraenkel, L. E., "The External Drag of Some Pitot-Type Intakes at Supersonic Speeds: Part I", Royal Aircraft Establishment Report No. Aero. 2380, Farnborough Great Britain, June 1950.
8. Hagseth, P. E., "F-16 Modular Common Inlet Design Concept", AIAA Paper No. 87-1748, June 1989.
9. John, J. E., Gas Dynamics, 2nd Ed., Prentice-Hall, New York, 1984.
10. Taylor J. R., An Introduction to Error Analysis, Oxford University Press, U.S.A., 1982.

11. Eckert, E. R.; Goldstein, R. J., "Measurements in Heat Transfer", 2nd Ed., McGraw-Hill, New York, 1976.
12. Malan, P. and Brown, E. F. "Prediction of Inlet Drag for Aircraft Conceptual Design", AIAA Proceedings, Vol. 1, A91-24358, 1990.
13. Leynaert, J., "Wind Tunnel Air Intake Test Technique", Office National d'Etudes et de Recherches Aerospatiales, 29 Avenue de la Division Leclerc, 92320 Chatillon, France, 1989.
14. Reed, T. D., Pope, T. C., and Cooksey, J. M. "Calibration of Transonic and Supersonic Wind Tunnels", NASA Contractor Report No. 2920, November 1977.
15. Anonymous, "Operating Instructions for Aerolab Supersonic Wind Tunnel", Aerolab Supply Co., Laurel, MD, 1986.
16. Anonymous, "Model DPT-6400, Digital Pressure Transmitter Users Manual", Pressure Systems Inc., Hampton, VA, 1984.
17. Van Dyke, M., An Album of Fluid Motion, The Parabolic Press, Stanford, CA, 1984.
18. Juvinall, R. C. and Marshek, K. M., Fundamentals of Machine Component Design, John Wiley & Sons, New York, 1991.

APPENDIX A.

SHADOWGRAPH PHOTOS

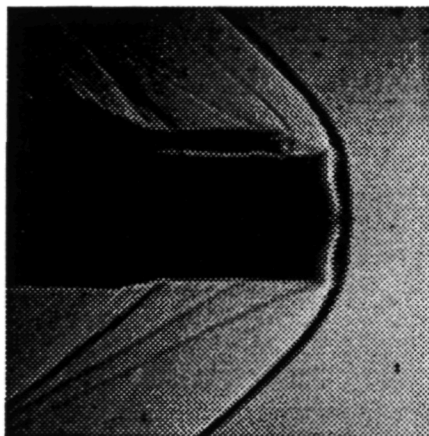
	<u>PAGE</u>
SHADOWGRAPH PHOTOS FOR TEST CONFIGURATION #1-1 .	100
SHADOWGRAPH PHOTOS FOR TEST CONFIGURATION #1-2 .	101
SHADOWGRAPH PHOTOS FOR TEST CONFIGURATION #1-3 .	102
SHADOWGRAPH PHOTOS FOR TEST CONFIGURATION #2-1 .	103
SHADOWGRAPH PHOTOS FOR TEST CONFIGURATION #2-2 .	104
SHADOWGRAPH PHOTOS FOR TEST CONFIGURATION #2-3 .	105



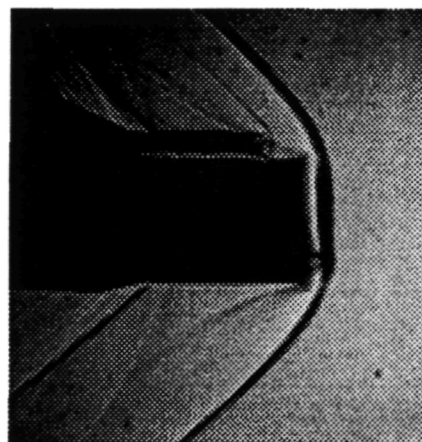
0 DEGREE ROTATION



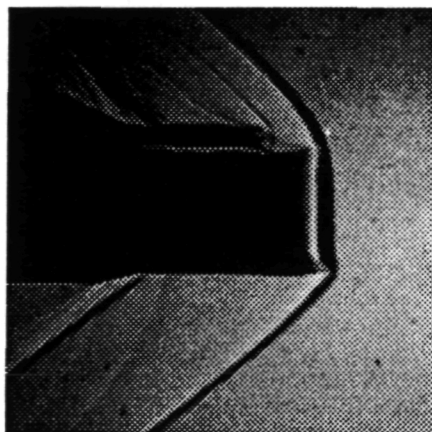
45 DEGREE ROTATION



90 DEGREE ROTATION

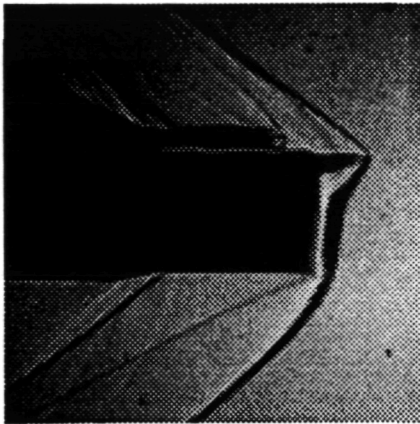


135 DEGREE ROTATION



180 DEGREE ROTATION

Figure A-1. Shadowgraph photos for test configuration #1-1.



0 DEGREE ROTATION



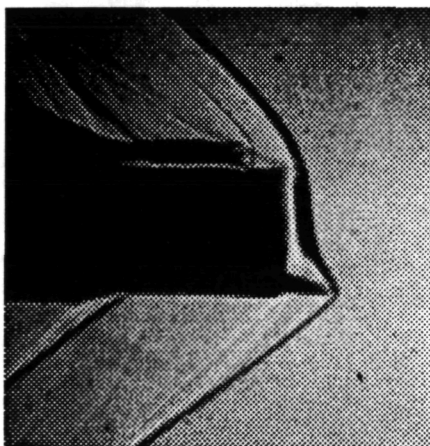
45 DEGREE ROTATION



90 DEGREE ROTATION

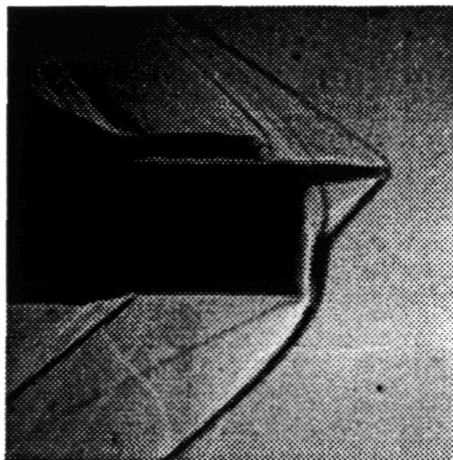


135 DEGREE ROTATION

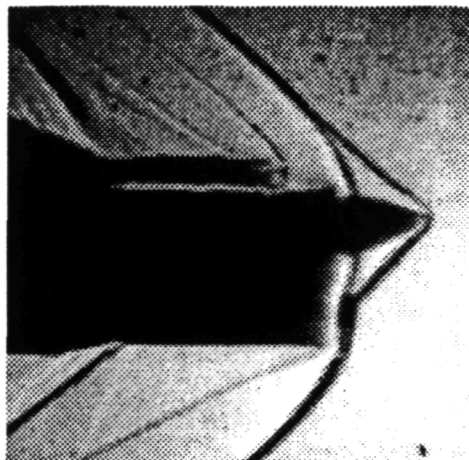


180 DEGREE ROTATION

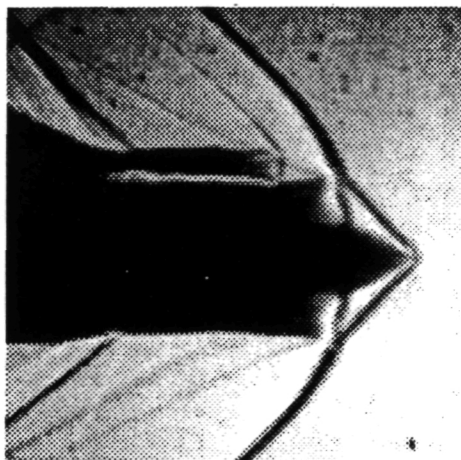
Figure A-2. Shadowgraph photos for test configuration #1-2.



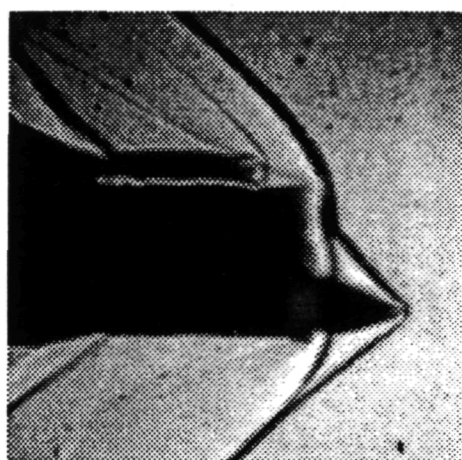
0 DEGREE ROTATION



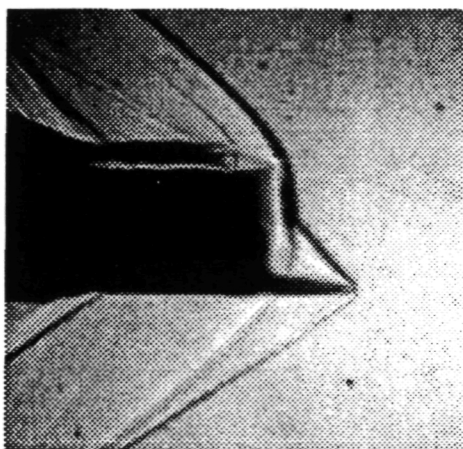
45 DEGREE ROTATION



90 DEGREE ROTATION

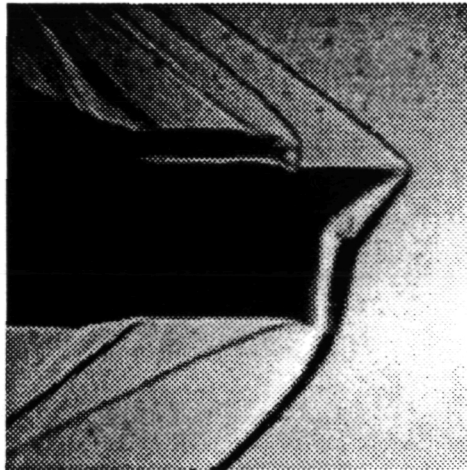


135 DEGREE ROTATION

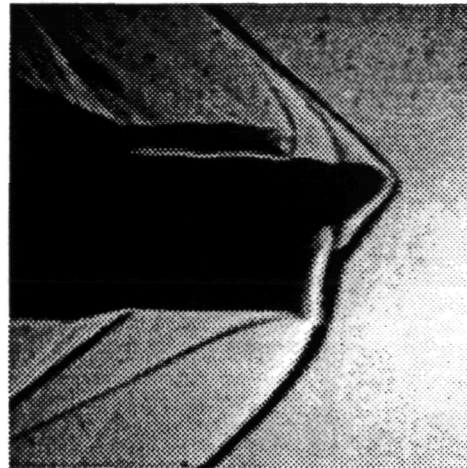


180 DEGREE ROTATION

Figure A-3. Shadowgraph photos for test configuration #1-3.



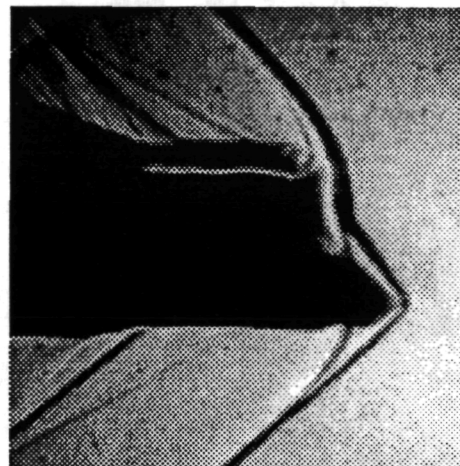
0 DEGREE ROTATION



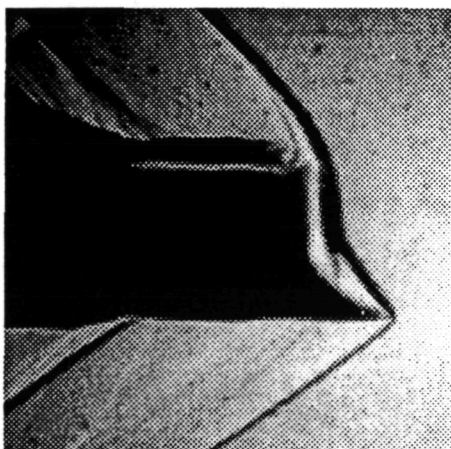
45 DEGREE ROTATION



90 DEGREE ROTATION

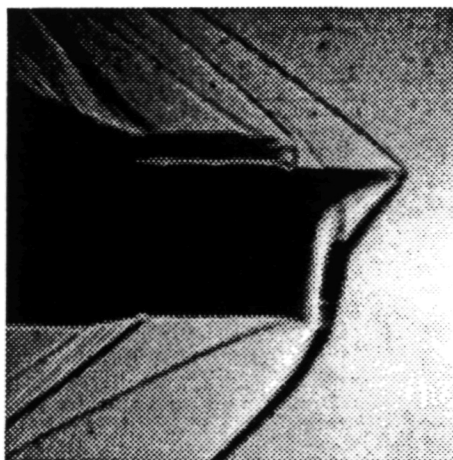


135 DEGREE ROTATION

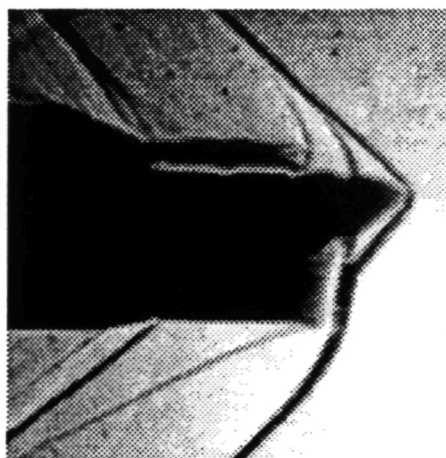


180 DEGREE ROTATION

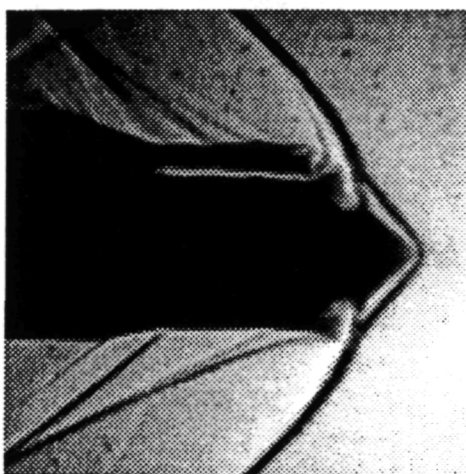
Figure A-4. Shadowgraph photos for test configuration #2-1.



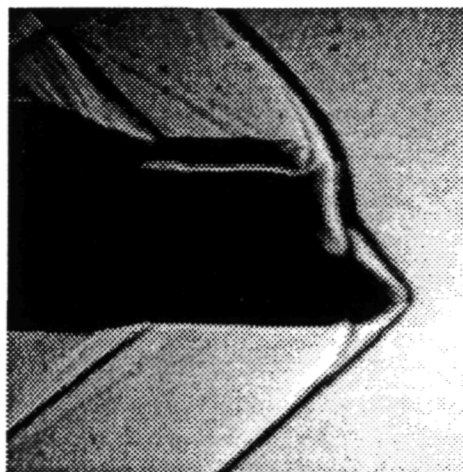
0 DEGREE ROTATION



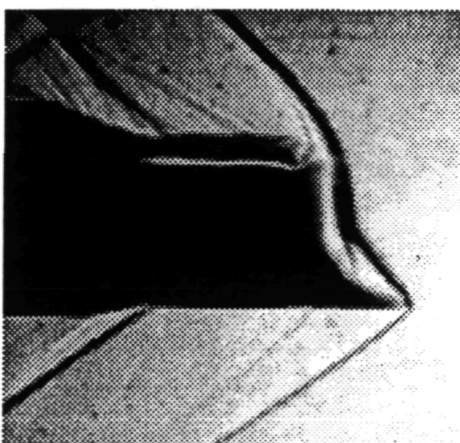
45 DEGREE ROTATION



90 DEGREE ROTATION

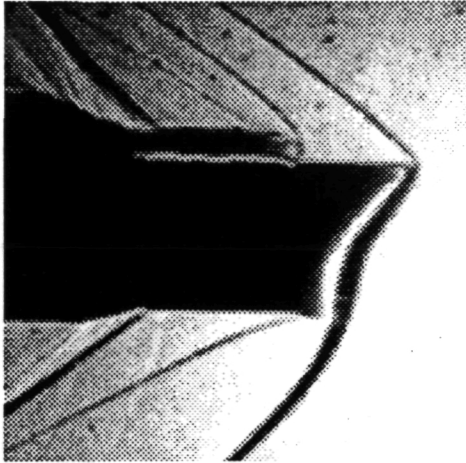


135 DEGREE ROTATION



180 DEGREE ROTATION

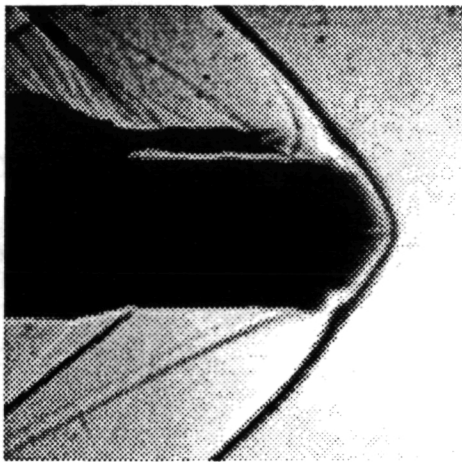
Figure A-5. Shadowgraph photos for test configuration #2-2.



0 DEGREE ROTATION



45 DEGREE ROTATION



90 DEGREE ROTATION



135 DEGREE ROTATION



180 DEGREE ROTATION

Figure A-6. Shadowgraph photos for test configuration #2-3.

APPENDIX B.

NUMERICAL ANALYSIS

	<u>PAGE</u>
B-1. GOVERNING EQUATIONS 107
B-2. PHYSICAL DOMAIN AND GRID TRANSFORMATION	. 110
B-3. NUMERICAL METHOD 111
B-4. REMARKS 114

NUMERICAL ANALYSIS

In this study, to validate the experimental results, an axisymmetrical SPARK code is utilized. The validation of the data is required to further strengthen the results. In numerical analysis, to minimize the computational time and to maximize the effectiveness in validating the experimental results, a simple circular pitot inlet without a deflector is selected as a numerical model for the comparison. Accordingly, in this chapter, the detailed descriptions of mathematical equations, numerical procedures, and boundary conditions for the analysis are discussed.

B-1. Governing Equations

For numerical analysis, the governing equations of Continuity, Momentum, and Energy are utilized. These equations are expressed in vector form as follows:

$$\frac{\partial U}{\partial t} + \frac{\partial F}{\partial x} + \frac{\partial G}{\partial y} = H \quad (B-1)$$

where vectors U, F, G, and H are expressed as

$$U = \begin{bmatrix} \rho \\ \rho u \\ \rho v \\ \rho E \end{bmatrix}$$

$$F = \begin{bmatrix} \rho u \\ \rho u^2 - \sigma_x \\ \rho uv - \tau_{xy} \\ (\rho E - \sigma_x)u - \tau_{xy}v + q_x \end{bmatrix}$$

$$G = \begin{bmatrix} \rho v \\ \rho uv - \tau_{xy} \\ \rho v^2 - \sigma_y \\ (\rho E - \sigma_y)v - \tau_{xy}u + q_y \end{bmatrix}$$

$$H = \frac{1}{y} \begin{bmatrix} \rho v \\ \rho uv + \tau_{xy} \\ \rho v^2 + \tau_{yy} - \tau\theta\theta \\ (\rho E + P + \tau_{yy})v - \tau_{xy}u + q_y \end{bmatrix}$$

Also, the related constitutive equations for the analysis are as follow:

$$\sigma_x = -P + 2\mu \frac{\partial u}{\partial x} + \lambda \nabla \cdot \mathbf{u} \quad (\text{B-2})$$

$$\sigma_y = -P + 2\mu \frac{\partial v}{\partial y} + \lambda \nabla \cdot \mathbf{u} \quad (\text{B-3})$$

$$\tau_{xy} = \mu \left(\frac{\partial u}{\partial y} + \frac{\partial v}{\partial x} \right) \quad (\text{B-4})$$

$$\tau_{yy} = -\frac{2}{3}\mu \left(2\frac{\partial v}{\partial y} - \frac{v}{y} - \frac{\partial v}{\partial x} \right) \quad (\text{B-5})$$

$$\tau_{\theta\theta} = -\frac{2}{3}\mu \left(2\frac{v}{y} - \frac{\partial v}{\partial y} - \frac{\partial u}{\partial x} \right) \quad (\text{B-6})$$

$$q_x = -k \frac{\partial T}{\partial x} \quad (\text{B-7})$$

$$q_y = -k \frac{\partial T}{\partial y} \quad (\text{B-8})$$

$$P = \rho RT \quad (\text{B-9})$$

$$E = -\frac{P}{\rho} + \frac{u^2 + v^2}{2} \quad (\text{B-10})$$

$$\frac{\mu}{\mu_0} = \left(\frac{T}{T_0} \right)^{\frac{3}{2}} \frac{T_0 + S}{T + S} \quad (\text{B-11})$$

$$\frac{k}{k_0} = \left(\frac{T}{T_0} \right)^{\frac{3}{2}} \frac{T_0' + S}{T + S} \quad (\text{B-12})$$

where the subscripted variables are derived from the referenced conditions.

B-2. Physical Domain and Grid Transformation

To solve the governing equations, the equations in the physical domain (x, y) is transformed into the computational domain (ζ, η) . The transformation is desired since it would result in a much simpler and uniform grid for analysis. Hence, the fluxes $F = F(x, y)$ and $G = G(x, y)$ are transformed as follow:

$$F_{\zeta} = F_x x_{\zeta} + F_y y_{\zeta} \quad (B-13)$$

$$F_{\eta} = F_x x_{\eta} + F_y y_{\eta} \quad (B-14)$$

$$G_{\zeta} = G_x x_{\zeta} + G_y y_{\zeta} \quad (B-15)$$

$$G_{\eta} = G_x x_{\eta} + G_y y_{\eta} \quad (B-16)$$

Then,

$$F_x = \frac{F_{\zeta} y_{\eta} - F_{\eta} y_{\zeta}}{J} \quad (B-17)$$

$$G_y = \frac{G_{\eta} x_{\zeta} - G_{\zeta} x_{\eta}}{J} \quad (B-18)$$

where the jacobian of the transformation is defined as

$$J = x_{\zeta} y_{\eta} - y_{\zeta} x_{\eta} \quad (B-19)$$

Once the variables are transformed, Eq. (B-1) is transformed into

$$\frac{\partial \hat{U}}{\partial t} + \frac{\partial \hat{F}}{\partial \zeta} + \frac{\partial \hat{G}}{\partial \eta} = \hat{H} \quad (\text{B-20})$$

where

$$\hat{U} = JU, \quad \hat{H} = JH$$

$$\hat{F} = y_{\eta} F - x_{\eta} G, \quad \hat{G} = x_{\zeta} G - y_{\zeta} F$$

B-3. Numerical Method

In the numerical analysis, the MacCormack's finite-difference method with the Lax-Wendroff's predictor-corrector scheme is employed. The scheme is second order accurate in time and space, and operates with a simultaneous spatial and temporal discrete system of equations at each grid points. The discrete form of Eq. (B-20) is as follow:

$$\frac{\hat{U}_{ij}^{n+1} - \hat{U}_{ij}^n}{\Delta t} = - \left[\left(\frac{\partial \hat{F}}{\partial \zeta} \right)_{ij}^n + \left(\frac{\partial \hat{G}}{\partial \eta} \right)_{ij}^n \right] + \hat{H}_{ij}^{n+1} \quad (\text{B-21})$$

or

$$\hat{U}_{ij}^{n+1} = \hat{U}_{ij}^n - \Delta t \left[\left(\frac{\partial \hat{F}}{\partial \zeta} \right)_{ij}^n + \left(\frac{\partial \hat{G}}{\partial \eta} \right)_{ij}^n - \hat{H}_{ij}^{n+1} \right] \quad (\text{B-22})$$

Since the equation displays non linear characteristics, the method of Taylor series expansion is utilized for the linearization. H is linearized as

$$\hat{H}_{ij}^{n+1} = \hat{H}_{ij}^n + \left(\frac{\partial \hat{H}}{\partial t} \right)^n \Delta t + o(\Delta t)^2 \quad (B-23)$$

where dH/dt is defined as

$$\frac{\partial \hat{H}}{\partial t} = \frac{\partial \hat{H}}{\partial \hat{U}} \frac{\partial \hat{U}}{\partial t} + \frac{\partial \hat{H}}{\partial \zeta_t} \frac{\partial \zeta_t}{\partial t} + \frac{\partial \hat{H}}{\partial \zeta_x} \frac{\partial \zeta_x}{\partial t} + \frac{\partial \hat{H}}{\partial \zeta_y} \frac{\partial \zeta_y}{\partial t} \quad (B-24)$$

Since the grid generated is time independent, the above expression is further simplified as

$$\frac{\partial \hat{H}}{\partial t} = \frac{\partial \hat{H}}{\partial \hat{U}} \frac{\partial \hat{U}}{\partial t} \quad (B-25)$$

The partial derivative dU/dt is obtained from the first order forward difference expression,

$$\frac{\partial \hat{U}}{\partial t} = \frac{\hat{U}^{n+1} - \hat{U}^n}{\Delta t} + o(\Delta t) = \frac{\Delta \hat{U}^{n+1}}{\Delta t} + o(\Delta t) \quad (B-26)$$

Substituting Eqs. (B-25) and (B-26) into Eq. (B-23), one obtains

$$\hat{H}_{ij}^{n+1} = \hat{H}_{ij}^n + \left(\frac{\partial \hat{H}}{\partial \hat{U}} \right)^n \Delta \hat{U}^{n+1} + o(\Delta t)^2 \quad (B-27)$$

Therefore, the linearized equation becomes

$$\hat{U}_{ij}^{n+1} = \hat{U}_{ij}^n - \Delta t \left[\left(\frac{\partial \hat{F}}{\partial \zeta} \right)_{ij}^n + \left(\frac{\partial \hat{G}}{\partial \eta} \right)_{ij}^n - \hat{H}_{ij}^n - \left(\frac{\partial \hat{H}}{\partial \hat{U}} \right)^n \Delta \hat{U}^{n+1} \right] \quad (B-28)$$

or

$$\frac{\Delta \hat{U}^{n+1}}{\Delta t} + \left(\frac{\partial \hat{F}}{\partial \zeta} \right)_{ij}^n + \left(\frac{\partial \hat{G}}{\partial \eta} \right)_{ij}^n = \hat{H}_{ij}^n + \left(\frac{\partial \hat{H}}{\partial \hat{U}} \right)^n \Delta \hat{U}^{n+1} \quad (B-29)$$

If the variables are redefined as

$$K^n = \left(\frac{\partial \hat{H}}{\partial \hat{U}} \right)^n$$

$$\hat{R}_{ij}^n = \left(\frac{\partial \hat{F}}{\partial \zeta} \right)_{ij}^n + \left(\frac{\partial \hat{G}}{\partial \eta} \right)_{ij}^n - \hat{H}_{ij}^n$$

then Eq (B-29) becomes

$$\frac{\Delta \hat{U}^{n+1}}{\Delta t} + \hat{R}^n - K^n \Delta \hat{U}^{n+1} = 0 \quad (B-30)$$

or

$$\Delta \hat{U}^{n+1} [I - K^n] = -\Delta t \hat{R}^n \quad (B-31)$$

where I is an identity matrix. At this point, the symbol "^" on both sides is dropped for convenience.

For the predictor step,

$$[I - \Delta t K_{ij}^n] \Delta U_{ij}^{n+1} = -\Delta t R_{ij}^n \quad (B-32)$$

In the predictor step, the variable R represents a forward spatial difference.
For the corrector step,

$$[I - \Delta t K_{ij}^{\overline{n+1}}] \Delta U_{ij}^{n+1} = -\Delta t R_{ij}^{\overline{n+1}} \quad (B-33)$$

In the corrector step, the variable R represents a backward spatial difference.
Therefore, Eq. (B-33) is rewritten as

$$U_{ij}^{n+1} = U_{ij}^n + \frac{1}{2} [\Delta U_{ij}^{\overline{n+1}} + \Delta U_{ij}^{n+1}] \quad (B-34)$$

With these steps, the solution advances from time n to n+1 until the solution converges. In instability analysis, since an implicit MacCormack method is utilized, the scheme is stable throughout the calculations. In the Lax-Wendroff scheme, an artificial viscosity is introduced to increase the convergence rate and to decrease the damping ratio. For numerical analysis, the viscosity is calculated based on the temperature and pressure. In the analysis, the initial conditions are given at the inflow boundary. As the solution marches, the supersonic outflow boundary conditions are extrapolated from the interior grid points, whereas the boundary conditions for subsonic regions are extrapolated from the neighboring supersonic grid points.

B-4. Remarks

Although the scheme is well explored, successful numerical analysis is not achieved. In the analysis, the orthogonality of the grid lines in both physical and computational domains are not successfully achieved. Hence, the

solution did not converge within the limit of tolerance. In future studies, a successful generation of grid for this model should be explored.

APPENDIX C.

UNCERTAINTY CALCULATIONS

	<u>PAGE</u>
C-1. UNCERTAINTY IN DIRECT MEASUREMENT 117
C-2. PROPAGATION OF UNCERTAINTY. 117

UNCERTAINTY CALCULATIONS

C-1. Uncertainty in direct measurement

If the stagnation pressures are measured as $a=45$ Psia, $b=47$ Psia, and $c=45$ Psia, then, the equations for mean stagnation pressure and its standard deviation are

$$A = \frac{a + b + c}{3.0} \quad (C-1)$$

$$SD_A = \frac{Abs(A-a) + Abs(A-b) + Abs(A-c)}{3.0} \quad (C-2)$$

$$SD_{fraction} = \frac{SD_A}{A} \quad (C-3)$$

With Eqs. (C-1) and (C-2), the mean stagnation pressure is $A=46$ Psia, and the standard deviation of 1.0 Psia. Or with Eq. (C-3), the fractional standard deviation is 0.022.

C-2. Propagation of uncertainty

Let's suppose that a variable has the mean stagnation pressure and its standard deviation of $A=46$ Psia and $SD=1.0$ Psia. Also, let's suppose that the other has the mean stagnation pressure and its standard deviation of $B=20$

Psia and SD=0.50. If the new variable C is defined as follows:

$$C = \left[\frac{B}{A} \right]^n \quad (C-4)$$

the equations for the propagation of uncertainty are as follows:

$$PU_{\text{fraction}} = n \left[\frac{SD_A}{A} + \frac{SD_B}{B} \right] \quad (C-5)$$

$$PU = PU_{\text{fraction}} C \quad (C-6)$$

If n is equal to 2, the fractional propagation of uncertainty (Eq. (C-5)) for C is 0.0023. Or with Eq. (C-6), the propagation of uncertainty for C is 0.0010.

APPENDIX D.

COMPUTER PROGRAMS

	<u>PAGE</u>
COMPUTER PROGRAM FOR DATA ACQUISITION. .	120
COMPUTER PROGRAM FOR DATA PRINTING . .	124
COMPUTER PROGRAM FOR CORRECTING DATA. .	126

***** Program for data acquisition *****

```

10 REM *****
20 REM **
30 REM **          OLD DOMINION UNIVERSITY          **
40 REM **
50 REM **          SUPERSONIC WIND TUNNEL            **
60 REM **
70 REM **          DATA ACQUISITION PROGRAM         **
80 REM **
90 REM **          USING PRESSURE SYSTEMS DPT-6400     **
100 REM **
110 REM **          DIGITAL PRESSURE TRANSMITTER      **
120 REM **
130 REM **          AND                               **
140 REM **
150 REM **          THE DASCON1 ANALOG/DIGITAL        **
160 REM **
170 REM **          INPUT/OUTPUT EXPANSION BOARD      **
180 REM **
190 REM **          by:                               **
195 REM **
200 REM **          KYU C. HWANG                      **
210 REM **          (GRADUATE STUDENT)                **
220 REM **
230 REM **          AND                               **
240 REM **
250 REM **
260 REM **          DR. COLIN P. BRITCHER             **
270 REM **          (FACILITY ADVISOR)                **
280 REM **
290 REM **          SPRING 1995                       **
300 REM **
310 REM *****
320 CLEAR,32768!
340 DEF SEG=0
350 SG=256*PEEK(&H511)+PEEK(&H510)
360 DASCON1=0
370 SG=(32768!/16)+SG
380 DEF SEG=SG
390 BLOAD "DASCON1.BIN",0
400 OPEN "I",#1,"DASCON1.ADR":INPUT#1,BASADR%:CLOSE #1
405 CH%=3          'CHANNEL NUMBER FOR THE DASCON1 ROUTINE
410 MD%=1          'MODE FOR THE DASCON1 ROUTINE
420 DIM P(100,30),MACH(100),T$(100),DIO%(8),TEMPF(150)
430 CLS:LOCATE 5,1:INPUT "ENTER ATMOSPHERIC PRESSURE (mm Hg)
";PMM
431 LOCATE 6,1:INPUT "EXPERIMENT SET NUMBER";Q1
432 LOCATE 7,1:INPUT "EXPERIMENT PART NUMBER";Q2
433 LOCATE 8,1:INPUT "PART POSITION ANGLE (DEG)";Q3
434 LOCATE 9,1:INPUT "PRESSURE PROBE 1 (POSITION)";Q4
435 LOCATE 10,1:INPUT "PRESSURE PROBE 2 (POSITION)";Q5
436 CLS
440 PATM=((PMM/1000)*9.810001*13560*(1/47.88))/144
450 GOSUB 770
460 ON TIMER (2) GOSUB 955
461 LOCATE 2,30 :PRINT Q1

```

```

462 LOCATE 3,30 :PRINT Q2
463 LOCATE 4,30 :PRINT Q3
464 LOCATE 5,30 :PRINT Q4
465 LOCATE 6,30 :PRINT Q5
470 GOSUB 550
480 GOSUB 1160
490 CLOSE
500 LOCATE 15,1:INPUT "DO YOU WANT TO MAKE ANOTHER RUN (Y/N) ";R$
510 IF R$="Y" THEN 430
520 IF R$="Y" THEN 430
530 KEY ON
540 END
550 REM
560 REM          ***** SCREEN UPDATES *****
570 REM
580 TIMER ON
590 MP=((2*(((P(I,22)+PATM)/(P(I,24)+PATM))^(.4/1.4))-1))/ .4)
600 IF MP<0 THEN 630
610 MACH(I)=MP^.5
620 GOTO 650
630 LOCATE 7,30:COLOR 4:PRINT"          ":COLOR 8:MACH(I)=0
640 GOTO 660
650 LOCATE 7,30:PRINT USING"###.##";MACH(I)
660 LOCATE 2,70:PRINT TIMES$
670 LOCATE 11,66:PRINT USING"###.##";TEMPF(I)
680 LOCATE 11,26:PRINT USING"###.###";P(I,17)
690 LOCATE 13,26:PRINT USING"###.###";P(I,18)
700 LOCATE 13,66:PRINT USING"###.###";P(I,21)
710 LOCATE 15,26:PRINT USING"###.###";P(I,23)
720 LOCATE 15,66:PRINT USING"###.###";P(I,22)
730 LOCATE 17,26:PRINT USING"###.###";P(I,20)
740 LOCATE 17,66:PRINT USING"###.###";P(I,24)
760 GOTO 590
770 REM
780 REM          ***** SCREEN SETUP *****
790 REM
800 KEY OFF:I=1:JJ=1
810 COLOR 8,14
820 CLS:LOCATE 1,1:PRINT"    ODU SUPERSONIC WIND TUNNEL"
823 LOCATE 2,1:PRINT"EXPERIMENT SET NUMBER"
824 LOCATE 3,1:PRINT"EXPERIMENT PART NUMBER"
825 LOCATE 4,1:PRINT"PART POSITION ANGLE (DEG)"
826 LOCATE 5,1:PRINT"PRESSURE PROBE 1 (POSITION)"
827 LOCATE 6,1:PRINT"PRESSURE PROBE 2 (POSITION)"
830 LOCATE 7,1:PRINT" MACH NUMBER"
840 LOCATE 11,1:PRINT"EXT. PRESSURE PROBE 1"
850 LOCATE 11,40:PRINT"EXT. STAG. TEMPERATURE (F)"
860 LOCATE 13,1:PRINT"EXT. PRESSURE PROBE 2"
870 LOCATE 13,40:PRINT"STORAGE PRESSURE"
880 LOCATE 15,1:PRINT"INTERNAL STAG. PRESSURE"
890 LOCATE 15,40:PRINT"EXTERNAL STAG. PRESSURE"
900 LOCATE 17,1:PRINT"INTERNAL STATIC PRESSURE"
910 LOCATE 17,40:PRINT"EXTERNAL STATIC PRESSURE"
930 LOCATE 23,70:PRINT"<CTRL-E>"
940 OPEN "COM1:1200,N,8,1,BIN" AS #2
950 RETURN

```

```

953 REM
955 REM ***** START DASCON1 CALL ROUTINE
960 JJ=JJ+1
970 CALL DASCON1(MD%,CH%,DIO%(0),DIO%(1),BASADR%)
980 TEMPC=DIO%(CH%)/5
985 REM***** CALCULATE STAGNATION TEMPERATURE IN DEGREES
FAHRENHEIT
990 TEMPF(JJ)=(9*TEMPC/5)+32
1000 REM
1010 REM          ***** COMMUNICATION WITH DPT-6400 *****
1020 REM
1030 Z$=INKEY$:IF Z$="" THEN 1050
1040 IF ASC(Z$)=5 THEN 480
1050 I=I+1:IF I=30 THEN 480
1060 T$(I)=RIGHT$(TIME$,5)
1070 PRINT#2, "SC0 17-24 "+CHR$(13);
1080 E$=INPUT$(1,#2)
1090 IF ASC(E$)=13 THEN 1080
1100 D$=E$+INPUT$(12,#2)
1110 CHAN=VAL(RIGHT$(LEFT$(D$,4),2))
1120 P(I,CHAN)=VAL(RIGHT$(D$,9))
1130 IF EOF(2) THEN 1150
1140 GOTO 1080
1150 RETURN
1160 REM
1170 REM          ***** SAVE DATA TO DISK *****
1180 REM
1190 CLOSE #2
1200 COLOR 7,0:CLS
1210 LOCATE 5,1:INPUT "DO YOU WANT TO SAVE TO DISK (Y/N) ";X$
1220 IF X$= "N" THEN 1460
1230 IF X$= "n" THEN 1460
1240 LOCATE 8,15:PRINT "***** THE DATA WILL BE STORED IN
C:\SST\QDAT *****"
1250 LOCATE 11,1:INPUT "FILE NAME ";DFIL$
1255 DFIL$=DFIL$+".BAS"
1260 OPEN "R",#3,"C:\SST\QDAT\"+DFIL$,42
1270 FIELD #3,4 AS M$,4 AS P1$,4 AS P2$,4 AS P4$,4 AS P6$,4 AS
P7$,4 AS P8$,4 AS P9$, 5 AS ST$
1280 FOR J=2 TO I+1
1290 LSET M$=MK$$(MACH(J))
1300 LSET P1$=MK$$(P(J,17))
1310 LSET P2$=MK$$(P(J,18))
1330 LSET P4$=MK$$(P(J,22))
1350 LSET P6$=MK$$(P(J,24))
1360 LSET P7$=MK$$(P(J,23))
1370 LSET P8$=MK$$(P(J,20))
1380 LSET P9$=MK$$(P(J,21))
1390 LSET ST$=MK$$(TEMPF(J))
1400 PUT #3,J
1410 NEXT J
1415 K=I+1
1420 FIELD #3,4 AS K$
1430 LSET K$=MK$$(K)
1440 PUT #3,1
1441 FIELD #3,4 AS Q11$

```

1442 LSET Q11\$=MK\$\$(Q1)
1443 PUT #3,K+1
1444 FIELD #3,4 AS Q12\$
1445 LSET Q12\$=MK\$\$(Q2)
1446 PUT #3,K+2
1447 FIELD #3,4 AS Q13\$
1448 LSET Q13\$=MK\$\$(Q3)
1449 PUT #3,K+3
1450 FIELD #3,4 AS Q14\$
1451 LSET Q14\$=MK\$\$(Q4)
1452 PUT #3,K+4
1453 FIELD #3,4 AS Q15\$
1454 LSET Q15\$=MK\$\$(Q5)
1455 PUT #3,K+5
1456 FIELD #3,4 AS PA\$
1457 LSET PA\$=MK\$\$(PATM)
1458 PUT #3,K+6
1459 LOCATE 13,1:PRINT "DISK LOAD COMPLETE"
1460 RETURN

***** DATA PRINTING *****

```

10 CLS
15 CLEAR
20 LPRINT:LPRINT:LPRINT:LPRINT:LPRINT:LPRINT:LPRINT
30 LPRINT:LPRINT
40 LPRINT:LPRINT
70 DIM MACH(100),P(100,25),T$(100)
80 CLS:LOCATE 5,1:LINE INPUT "WHAT FILE DO YOU WANT ? ";DFIL$
81 DFIL$=DFIL$+".BAS"
85 PRINT "FILE NAME: ";DFIL$
90 LPRINT "FILE NAME: ";DFIL$
100 OPEN "R",#3,"C:\SST\QDAT\"+DFIL$,42
105 FIELD #3,4 AS K$
110 GET #3,1
111 K=CVS(K$)
112 FIELD #3,4 AS Q11$
113 GET #3,K+1
115 LPRINT "EXPERIMENT SET NUMBER: ";CVS(Q11$)
116 PRINT "EXPERIMENT SET NUMBER: ";CVS(Q11$)
117 FIELD #3,4 AS Q12$
118 GET #3,K+2
119 LPRINT "EXPERIMENT PART NUMBER: ";CVS(Q12$)
120 PRINT "EXPERIMENT PART NUMBER: ";CVS(Q12$)
121 FIELD #3,4 AS Q13$
122 GET #3,K+3
123 LPRINT "PART POSITION ANGLE (DEGREE): ";CVS(Q13$)
124 PRINT "PART POSITION ANGLE (DEGREE): ";CVS(Q13$)
125 FIELD #3,4 AS Q14$
126 GET #3,K+4
127 LPRINT "PRESSURE PROBE 1 (POSITION): ";CVS(Q14$)
128 PRINT "PRESSURE PROBE 1 (POSITION): ";CVS(Q14$)
129 FIELD #3,4 AS Q15$
130 GET #3,K+5
131 LPRINT "PRESSURE PROBE 2 (POSITION): ";CVS(Q14$)
132 PRINT "PRESSURE PROBE 2 (POSITION): ";CVS(Q15$)
133 FIELD #3,4 AS PA$
134 GET #3,K+6
135 PRINT:PRINT "ATMOSPHERIC PRESSURE (PSI) : ";CVS(PA$)
136 PRINT:PRINT
140 LPRINT:LPRINT "ATMOSPHERIC PRESSURE (PSI) : ";CVS(PA$)
150 LPRINT:LPRINT
158 PRINT "      MACH      PROB 1  PROB 2  EX STAG EX STAT IN STAG IN
STAT STOR      TEMP"
159 PRINT "      NUMBER      (PSI)      (PSI)      (PSI)      (PSI)      (PSI)
(PSI)      (PSI)      (F) "
160 LPRINT "      MACH      PROB 1  PROB 2  EX STAG EX STAT IN STAG IN
STAT STOR      TEMP"
161 LPRINT "      NUMBER      (PSI)      (PSI)      (PSI)      (PSI)      (PSI)
(PSI)      (PSI)      (F) "
170 LPRINT:LPRINT
171 PRINT:PRINT
180 FIELD #3,4 AS M$,4 AS P1$,4 AS P2$,4 AS P4$,4 AS P6$,4 AS
P7$,4 AS P8$,4 AS P9$,5 AS ST$
185 FOR I=2 TO K
190 GET #3,I
220 PRINT USING

```

```
"####.###";CVS(M$);CVS(P1$);CVS(P2$);CVS(P4$);CVS(P6$);CVS(P7$);C
VS(P8$);CVS(P9$);CVS(ST$)
230 LPRINT USING
"####.###";CVS(M$);CVS(P1$);CVS(P2$);CVS(P4$);CVS(P6$);CVS(P7$);C
VS(P8$);CVS(P9$);CVS(ST$)
240 NEXT I
250 CLOSE
252
LPRINT:LPRINT:LPRINT:LPRINT:LPRINT:LPRINT:LPRINT:LPRINT:LPRINT:LP
RINT
253 LPRINT:CLS
255 LOCATE 5,1:INPUT "do you want to print again?"; RS$
256 IF RS$="Y" THEN 10
257 IF RS$="Y" THEN 10
260 END
```

***** Program for Experimental Data Correction *****

*23456789

```

    program crunch_data
    character*21 zname,name
    dimension zmachld(100),prold(100),pro2d(100),exstagd(100)
    dimension exstatd(100),zinstatd(100),zinstagd(100)
    dimension zqpro2d(100),zqprold(100),zqexstagd(100),zqexstatd(100)
    dimension zqzinstatd(100),zqzinstagd(100),zqzmachld(100)
    dimension zqerr1(100),zqerr2(100),zqerr3(100),zqerr4(100)
    dimension zqerr6(100),zqerr7(100),zqerr5(100),zzposit(100)
    real zmach1,pro1,pro2,exstag,exstat,zinstat,zinstag,atmos
    real zposit,zz,zzz,ratio,zerror,zcor,zprolper2
    real zerror1, zerror2, zerror3
    integer j,n,k,i
4  write(*,*) 'enter the file name for input'
    read(*,*)name
    open (1,file=name)
    write(*,*) 'enter the file name for output'
    read(*,*)zname
    open (2,file=zname)
    read(1,*)atmos
    j=15
    gamma=1.4
    do 200 n=1,j,1
        read(1,*)zposit,zmach1,pro1,pro2,exstag,exstat,zinstag,zinstat
        prold(n)=pro1+atmos
        pro2d(n)=pro2+atmos
        exstagd(n)=exstag+atmos
        exstatd(n)=exstat+atmos
        zinstatd(n)=zinstat+atmos
        zinstagd(n)=zinstag+atmos
        zmachld(n)=zmach1
        zzposit(n)=zposit
    200 continue
    ***** zz represented the corrected mach number after bow shock*****
    ***** zprolper2 represented the corrected probe pressure ratio *****
    do 100 i=1,j,1
        ratio=pro2d(i)/prold(i)
        zzz=0.001
        zz=1.
19  zcor=(zz**2.+2./(gamma-1.))/(2.*gamma/(gamma-1.)*zz**2.-1.)
        zerror=ratio-(1.+zcor*(gamma-1.)/2.)*(gamma/(gamma-1.))*
        *(2.*gamma*zz**2./(gamma+1.)-(gamma-1.)/(gamma+1.))
        if (abs(zerror) .le. 0.0001) goto 20
        zz=zz+zzz
        if (zz .ge. 2.) then
            zzz=zzz/10.
            zz=1.0
        endif
        goto 19
20  zprolper2=1./(1.+(gamma-1.)/2*zz**2)**(gamma/(gamma-1.))
        write(2,10)zzposit(i),zmachld(i),zz,
        %zprolper2,
        %exstatd(i)/exstagd(i),
        %zinstatd(i)/zinstagd(i)
10  format(2x,f7.2,2x,f5.3,2x,f5.3,2x,f8.5,2x,
        %f8.5,2x,f8.5)
100 continue
    write(*,*) 'would you like to run again? yes=1 no=2'
    read(*,*)k
    if (k .le. 1.1) goto 4

```

stop

***** Program for Average Experimental Data Correction *****

*23456789

```
program crunch_data
character*21 zname,name
dimension zmachld(100),prold(100),pro2d(100),exstagd(100)
dimension exstatd(100),zinstatd(100),zinstagd(100)
dimension zqpro2d(100),zqprold(100),zqexstagd(100),zqexstatd(100)
dimension zqzinstatd(100),zqzinstagd(100),zqzmachld(100)
dimension zqerr1(100),zqerr2(100),zqerr3(100),zqerr4(100)
dimension zqerr6(100),zqerr7(100),zqerr5(100),zzposit(100)
real zmachl,prol,pro2,exstag,exstat,zinstat,zinstag,atmos
real zposit,zz,zzz,ratio,zerror,zcor,zprolper2
real zerror1,zerror2,zerror3
integer j,n,k,i
4 write(*,*)'enter the file name for input'
read(*,*)name
open (1,file=name)
write(*,*)'enter the file name for output'
read(*,*)zname
open (2,file=zname)
read(1,*)atmos
gamma=1.4
do 200 n=1,15,1
read(1,*)zposit,zmachl,prol,pro2,exstag,exstat,zinstag,zinstat
prold(n)=prol+atmos
pro2d(n)=pro2+atmos
exstagd(n)=exstag+atmos
exstatd(n)=exstat+atmos
zinstatd(n)=zinstat+atmos
zinstagd(n)=zinstag+atmos
zmachld(n)=zmachl
zzposit(n)=zposit
200 continue
do 50 j=1,5,1

zqprold(j)=(prold(1+(j-1)*3)+prold(2+(j-1)*3)+prold(3+(j-1)*3))/3.

zqerr1(j)=(abs(zqprold(j)-prold(1+(j-1)*3))+abs(zqprold(j)-
%prold(2+(j-1)*3))+abs(zqprold(j)-prold(3+(j-1)*3)))/3.

zqpro2d(j)=(pro2d(1+(j-1)*3)+pro2d(2+(j-1)*3)+pro2d(3+(j-1)*3))/3.
zqerr2(j)=(abs(zqpro2d(j)-pro2d(1+(j-1)*3))+abs(zqpro2d(j)-
%pro2d(2+(j-1)*3))+abs(zqpro2d(j)-pro2d(3+(j-1)*3)))/3.

zqexstagd(j)=(exstagd(1+(j-1)*3)+exstagd(2+(j-1)*3)+
%exstagd(3+(j-1)*3))/3.
zqerr3(j)=(abs(zqexstagd(j)-exstagd(1+(j-1)*3))+abs(zqexstagd(j)-
%exstagd(2+(j-1)*3))+abs(zqexstagd(j)-exstagd(3+(j-1)*3)))/3.

zqexstatd(j)=(exstatd(1+(j-1)*3)+exstatd(2+(j-1)*3)+
%exstatd(3+(j-1)*3))/3.
zqerr4(j)=(abs(zqexstatd(j)-exstatd(1+(j-1)*3))+abs(zqexstatd(j)-
%exstatd(2+(j-1)*3))+abs(zqexstatd(j)-exstatd(3+(j-1)*3)))/3.

zqzinstatd(j)=(zinstatd(1+(j-1)*3)+zinstatd(2+(j-1)*3)+
%zinstatd(3+(j-1)*3))/3.
zqerr5(j)=(abs(zqzinstatd(j)-zinstatd(1+(j-1)*3))+
%abs(zqzinstatd(j)-
%zinstatd(2+(j-1)*3))+abs(zqzinstatd(j)-zinstatd(3+(j-1)*3)))/3.
```



```

      zqzinstagd(j)=(zinstagd(1+(j-1)*3)+zinstagd(2+(j-1)*3)+
%zinstagd(3+(j-1)*3))/3.
      zqerr6(j)=(abs(zqzinstagd(j)-zinstagd(1+(j-1)*3))+
%abs(zqzinstagd(j)-
%zinstagd(2+(j-1)*3))+abs(zqzinstagd(j)-zinstagd(3+(j-1)*3)))/3.

      zqzmachld(j)=(zmachld(1+(j-1)*3)+zmachld(2+(j-1)*3)+
%zmachld(3+(j-1)*3))/3.
      zqerr7(j)=(abs(zqzmachld(j)-zmachld(1+(j-1)*3))+abs(zqzmachld(j)
%-zmachld(2+(j-1)*3))+abs(zqzmachld(j)-zmachld(3+(j-1)*3)))/3.

50  continue
***** zz represented the corrected mach number after bow shock ****
***** zprolper2 represented the corrected probe pressure ratio ****
      do 100 i=1,5,1
        ratio=zqpro2d(i)/zqprold(i)
        zzz=0.001
        zz=1.
19   zcor=(zz**2.+2./(gamma-1.))/(2.*gamma/(gamma-1.)*zz**2.-1.)
        zerror=ratio-(1.+zcor*(gamma-1.)/2.)*(gamma/(gamma-1.))*
% (2.*gamma*zz**2./(gamma+1.)-(gamma-1.)/(gamma+1.))
        if (abs(zerror) .le. 0.00001) goto 20
        zz=zz+zzz
        if (zz .ge. 2.) then
          zzz=zzz/10.
          zz=1.0
        endif
        goto 19
20   zprolper2=1./(1.+(gamma-1.)/2*zz**2)*(gamma/(gamma-1.))
        zerror1=(zqerr2(i)/zqpro2d(i)+zqerr1(i)/zqprold(i))
        zerror2=zqerr3(i)/zqexstacd(i)+zqerr4(i)/zqexstatd(i)
        zerror3=zqerr5(i)/zqzinstatd(i)+zqerr6(i)/zqzinstagd(i)
        write(2,10) 45*(i-1),zqzmachld(i),zqerr7(i),zz,zz*zerror1,
%zprolper2,zprolper2*zerror1,
%zqexstatd(i)/zqexstacd(i),zerror2,
%zqzinstatd(i)/zqzinstagd(i),zerror3
10  format(1x,i4,,2x,f5.3,2x,f5.4,2x,f5.3,2x,f5.4,2x,f8.5,2x,
%f6.5,2x,f8.5,2x,f6.5,2x,f8.5,2x,f6.5)
100  continue
      write(*,*)'would you like to run again? yes=1 no=2'
      read(*,*)k
      if (k .le. 1.1) goto 4
      stop
      end

```